Lensless Digital Holographic Microscopy for differentiation and counting of blood cells in a microfluidic device using Computer Vision

Owen Knightley Long

Masters Of Science By Research

University Of York

Physics, Engineering and Technology

January 2024

Abstract

This research paper presents lensless digital holographic microscopy (LDHM) combined with computer vision techniques for differentiating and counting blood cells in microfluidic flow.

A lensless holographic imaging setup captures holographic interference patterns of blood cells in a microfluidic channel using a digital sensor. LDHM eliminates the need for lenses, allowing for low cost, simplistic and robust designs, increasing suitability for decentralised testing and personalised healthcare. LDHM offers advantages of non-invasiveness, label-free and potential for real-time results; by utilising computer vision, it enables rapid and automated detection of particle populations, potentially aiding early disease detection and assessing treatment success via ongoing monitoring.

Computer vision algorithms allow for reconstruction of holograms, in order for further analysis such as to extract features, and classify cells based on morphology. This allows for a sample to be monitored over time, allowing for an accurate count of particles over time and averaging to generate an accurately calculated particle concentration.

This paper aims to display the potential for LDHM for blood cell differentiation and count as a form of blood analysis, and how this technology can be designed in an effective yet affordable manner, with its simplistic design having further potential for point-of-care translation.

Contents

List Of Figures

List Of Tables:

Acknowledgements

I would like to use this section to highlight some of the amazing people that, during my time in York, offered endless amounts of support, advice and encouragement.

First and foremost I would like to thank my supervisors Prof. Steven Johnson and Prof. Thomas Krauss for guiding me through what proved to be a fascinating yet challenging project, offering advice, support and constructive feedback with genuine enthusiasm.

Nyasha Suliali, who always found time to offer help, whether it was the smallest, silliest question to complex issues and practical advice. This support was invaluable and helped pull me through some dead ends and confusion, and I am forever grateful for it.

Sebastien Guilbaud, who aided me in drilling through glass slides (which proved to be no easy task and resulted in a lot of broken glass) in order for me to construct my microfluidics, which was crucial to my project and many milestones that I achieved.

Ellie Bennett, who kindly supervised and aided me in my blood sample testing. Not being from a biology-related field, I really appreciated the learning opportunity of using biological samples and applying them to my prototype. The results gained from the experiments were invaluable.

I would also like to thank the entire BIT-lab office, who were extremely welcoming and created an extremely supportive environment to work and learn, to the point I cannot possibly name every single person and every act of kindness offered.

Lastly, I would like to thank my other-half, Becks, who was by my side through every stressed and happy moment, every up and down. It's been a rollercoaster of a year, and while it's sad my time at York is over, I am extremely excited to see where we go next.

Author Declaration

I, Owen Knightley Long, declare that this thesis is a presentation of original work and I am the sole author.

This work has not previously been presented for a degree or other qualification at this University or elsewhere. All sources are acknowledged as references, and where third party content, such as other published work, has been used, is highlighted in the main body of text as well as the source referenced.

1: Introduction:

In England, the workload attributed to pathology services within the National Health Service, NHS, is seeing an annual 8 to 10 percent increase, with pathology investigations costing £2.5 billion in funding annually [1]. Of the clinical pathways within the NHS, approximately 95% relies on pathology services, making it vital to the healthcare service [2]. Pathology services are broad in scope, with "pathology" meaning the "study of disease" [3], with the goal of providing clinical diagnostics and treatments. One of these services, haematology , the medical branch responsible for the study of blood, blood disorders and treatment, in particular accounts for an approximate 130 million tests per annum [4].

Haematological testing, a range of biomedical tests that utilise biomarkers present in an individual's blood, is a critical tool in haematology for diagnosis , treatment and management of a wide range of medical conditions. Blood cell counting is a component of clinical blood analysis and considered the foundation of clinical haematology [5] . It allows data to be collected on the number of cells, of different cell groups (Red Blood Cells, White blood cells, platelets), in a whole / diluted blood sample, allowing concentrations to be calculated for each, as well as calculations such as haemoglobin (Hb) concentration [6].

Blood cell concentrations are a good indicator of overall health and potential health issues. Abnormal cell counts for white and red blood cells (RBCs) indicate separate issues, Low white blood cells (WBCs), as a crucial component of the immune system, can indicate a weakened immune system, such as acquired immunodeficiency syndrome (AIDs) [7], with increased white blood cell count potentially indicating an immune response triggered by an infection, bodily trauma & inflammation or certain health conditions[8]. Whereas low RBC count could indicate issues such as anaemia [9], while a high blood cell count indicates dehydration[10].This measurement does not just have importance in initial diagnosis; it can be used to monitor long term conditions or assess treatment plans.

Home solutions in terms of medical technologies allow patients to access the benefits of an intervention from the comfort of their own home, often without a trained medical professional present. This, for the patients, avoids appointment waiting times, potentially difficult commutes and gives them the freedom to personalise their approach to healthcare. For hospitals, particularly as seen with the NHS during the COVID-19 pandemic, at-home diagnostic solutions can also ease the pressure felt by the NHS, reducing the requirement for in-hospital testing and reducing the lead time to gain results for patients [11]. This highlights the need for the distributed healthcare approach, especially with a growing and ageing population.

This project will focus on blood cell counting at point of care using a Lensless Digital Holographic Microscopy (LDHM) approach. LDHM offers the visualisation benefits, such as potential for morphological analysis, of hemocytometers, as well as the potential for high throughput, automated testing similar to technology such as coulter counters. With haemocytometers and Coulter counters representing manual and automated industry standard methods respectively; the LDHM approach aims to combine the benefits of both into a system that is uniquely suitable for point of care diagnostics, given the low cost, robustness & simplicity of the LDHM system design.

1.1: Project Objectives:

This project aims to investigate the use of a Lensless Digital Holographic Microscopy (LDHM) approach for blood cell counting, within the context of at-home diagnostic technologies. A LDHM system has multiple components, from the physical components, to the supporting software; this has led to multiple objectives being identified.

1. **Optimise system design through investigation of LDHM components and geometry**
    a. Investigate the effects of size variation in the subsection lengths and their effects on quality of digital holography.
    b. Investigate the effects of pinhole / aperture size variation on the quality of digital holography.
    c. Investigate the effects of polariser variation on the quality of digital holography.
    d. Investigate the effects of light source wavelength variation on the quality of digital holography.

2. **Design a supporting software**
    a. Explore algorithms for digital reconstruction of holographic images.
    b. Investigate computer vision approach to automate particle identification, differentiation and count.
    c. Experiment with Computer Vision; with the aim of successful particle detection, sizing and categorisation, using manufactured (artificial) particle samples and biological samples (e.g. blood).

3. **Design a simple system compatible with at-home use.**
    a. Develop a device that is small, lightweight and portable.
    b. Develop a device that is low cost & low complexity.

4. **Experiment with designed LDMH system & software**
    a. Experiment with artificial & clinical samples, with the aim of correctly detecting, sizing and categorising the particles.
    b. Analyse potential for clinical use.
    c. Identify potential improvements / further development.

Understanding the physical geometry, the hardware, assembly and software requirements for a LDHM system is paramount for the development and optimisation of a device. The design and optimisation of this system requires a fine balance of hardware, software, and device geometry considerations.

As briefly mentioned, there is a desire within healthcare to automate processes to reduce the time taken for diagnostic tasks. Moreover, automation is critical to support the move towards distributed and decentralised diagnostics. Some technologies, such as Coulter Counting, are able to produce results without human intervention; therefore for LDHM technology to be a competitive option, there must be automation potential. This, in conjunction with the device's simplicity and compact size, potentially eliminates the need for data collection / processing by trained individuals, allowing for the possibility of at-home use.The philosophy of at-home diagnostics and decentralised healthcare plays a key role in the influence of the design. Particular attention has been paid to the size, weight and complexity in terms of use and user interaction.

The system would also need to be tested, using all components (hardware and software), to demonstrate the potential benefits of an LDHM system for blood count analysis. This, for ethical reasons and ease of testing would need to utilise both artificial and clinical samples.

1.2: Thesis Structure:

Chapter 1: Introduction

This chapter provides an overview of the area of research, highlighting the importance of blood work relative to centralised healthcare and how diagnostic technologies, especially point-of-care technology, may ease the strain on healthcare systems, such as the National Health Service (NHS). This chapter also introduces the concept of Lensless Digital Holographic Microscopy technology, and the goals of this project.

Chapter 2: Theory & Literature

This chapter will provide the theoretical background of LDHM, starting from basic wave theory and progressing to a full LDHM system. The theory behind bloodwork and its significance will also be discussed, to provide a rounded view of the project and the research direction. Competing technologies and methods will be discussed; analysing modern research to highlight advantages and disadvantages of these technologies in comparison to LDHM, in the context of blood analysis. This will form the basis of the theory behind the experimentation for system development and optimisation, providing context, and highlighting the significance of the parameters discussed in the following section as well as highlighting the decision to focus on a LDHM approach.

Chapter 3: Design Experiments

This chapter will reflect the system variables discussed in the "Background Theory" section, translating the variables into physical experiments to aid in designing and optimising a LDHM system. Other factors, such as electronic components (e.g. LED driver) and test sample options will also be discussed. This section will be summarised by a final design prototype.

Chapter 4: Microfluidics

This chapter will discuss the need for microfluidics as well as the sample delivery systems used throughout the course of the project, highlighting the development of a bespoke, transparent microfluidic channel compatible with microscopy.

Chapter 5: Software

This chapter will focus on the software element of the project. Justification will be given for the need for a software element, as well as the chosen language, however the main focus will be on the development and testing of the software. Only code snippets will be used in this section, though the entire script will be provided in the appendix - this is to provide function highlights within the thesis, without flooding the main text with code.

Chapter 6: Testing

This chapter will cover the testing element of the project, that is the combined testing of the physical prototype, the microfluidic delivery and the software processing. The testing will use both artificial and real blood samples.

Chapter 7: Discussion

This chapter will discuss the findings of the project, relative to current research and other competing technologies. The limitations of the project will be analysed and discussed, with solutions being proposed. Potential avenues for further development of the project will be discussed.

Chapter 8: Conclusion

This chapter will provide an overview of the project as a whole, providing a summary of the project achievements, limitations and future potential.

2: Theory & Literature:

2.1: Waves & Light

2.1.1: Properties:

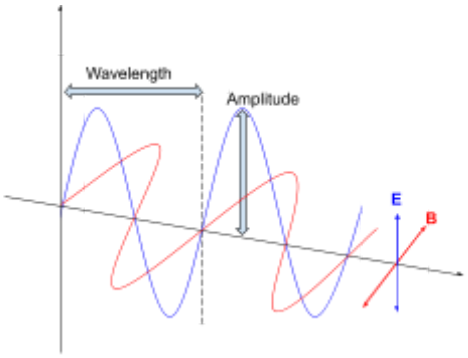

Figure 1: Light Wave Diagram

A wave in the simplest terms is an oscillation that transfers a quantity of energy through a medium or free space (vacuum). In terms of electromagnetic waves, the wave consists of an electric (E-field) and magnetic (B-field) component, oscillating perpendicular to each other. These two wave components additionally oscillate perpendicular to the direction of wave propagation, as shown by Figure 1.

Waves have three major components, wavelength, amplitude and frequency. The wavelength, λ, is the length of one oscillation cycle, commonly measured in nanometers (nm, $1x10^{-9}$m) for the visible spectrum. The frequency (f) the number of wavelengths passing through a point per second, measured in Hertz (Hz or s^{-1}). The relationship between wavelength and frequency for an electromagnetic wave travelling in free space is $\lambda = c / f$ where the constant 'c' refers to the the speed of light in a vacuum, measured in in metres per second (m s^{-1})
The amplitude of a wave is the magnitude of the peak, intensity of the wave being proportional to the square of the amplitude. This is highlighted by equation [12];

$I = ½ \varepsilon_0 c \varepsilon^2$

Where I is intensity (W m^{-2}), ε_0 is the permittivity of free space (8.854 x 10^{-12} F m^{-1}), c being the speed of light and E being the electric field amplitude (V m^{-1}). For applications where the wave is traversing a medium other than free space, the relative permeability of the medium, as well as the speed of light in that medium, would have to be accounted for. This forms the equation

$I = ½ \varepsilon c_n \varepsilon^2$

Where ε is the permittivity of the medium and c_n is the speed of light in the medium. c_n can be calculated by $c_n = c / n$, which is the speed of light in a vacuum over the refractive index of the medium.[12]

Visible light is a section of the electromagnetic spectrum that ranges from approximately 380 nm to 750 nm. The perceived colour of light is determined by the wavelength; with shorter wavelengths corresponding to violet / blue, and larger wavelengths corresponding to red. As the frequency of light is inversely proportional to the wavelength, meaning that higher frequency light has a shorter wavelength.

2.1.2: Phase Difference, Coherence

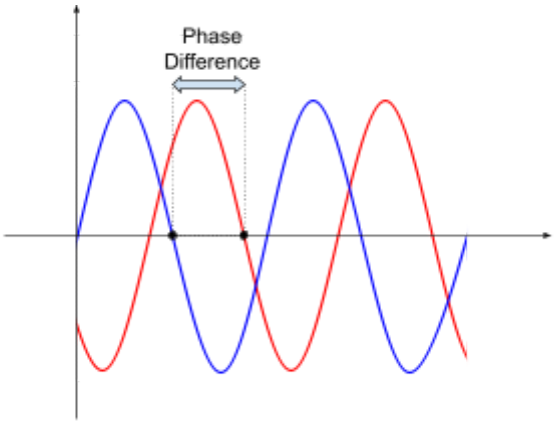

Figure 2: Phase difference between two waves

When two waves interact, phase difference is key to understanding how the two will interfere with each other. A wave forms a repeating, oscillating pattern, with "phase" being a point along this cycle at a given time. When two waves meet, one may be further along or behind the cycle than the other meaning there will be a phase difference between them, shown by Figure 2. This difference is measured in either radians or degrees, as waveforms are cyclical in nature, they are linked to trigonometric functions, with complex waveforms being simplified into a series of sin and cosine functions via fourier analysis. This means a full cycle for a wave can be thought of as one full rotation of a circle, being 2π radians or 360 degrees. [13]

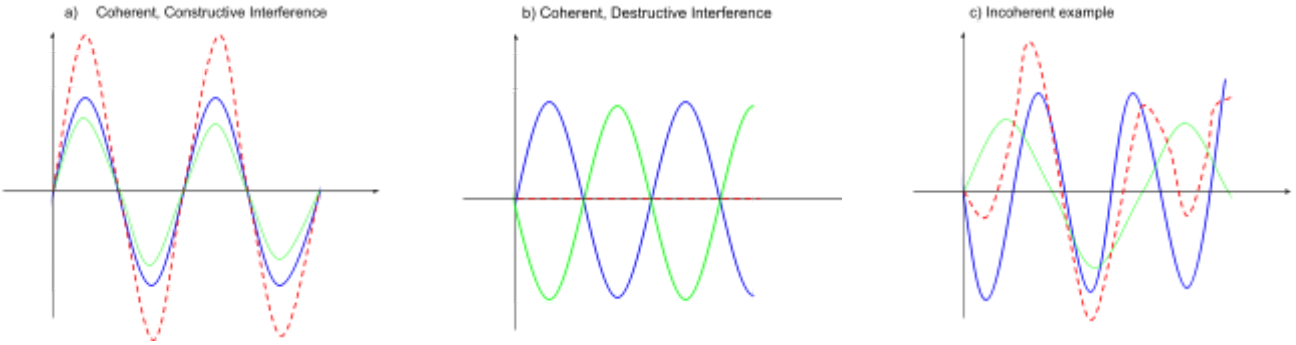

Figure 3: Interference between waves (Coherent [constructive,destructive] & incoherent)

Waves are said to be "coherent" if their phase difference is constant, while waves that have a non-constant phase difference are said to be "incoherent". As mentioned above, phase difference provides information about how two waves will interfere with each other; this interference takes two forms, constructive (additive) and destructive (subtractive). In terms of perfect constructive interference (Figure 3a), with peaks and troughs aligning, the phase difference would be 0 or a constant multiple of 2π radians (a full cycle), this would result in a combined waveform that would be equivalent to the amplitudes of the two waves. In terms of perfect destructive interference (Figure 3b), with peaks of one wave aligning with the troughs of another and the waves being of equal amplitude, the phase being odd multiples of π radians results in the combined waveform being nullified - perfectly cancelled out. Incoherent light is not perfectly aligned however, this results in a complex waveform, resulting from both constructive and destructive interference (Figure 3c).[13]

The wavefronts from an emitting source have a degree of phase uniformity across the space of which the wave has traversed at any given time, this is referred to as spatial coherence. High spatial coherence would refer to the

phase relationship between the wavefronts being consistent over the distance traversed, with low spatial coherence being a non-constant phase relationship.

Additionally, there is the phase-relationship between wavefronts over time; referred to as temporal coherence. Light sources of a single wavelength (high degree of spectral purity), have a higher temporal coherence; fluctuations in the wavelength of this emitting source would impact the temporal coherence of the light produced, meaning a stable light source is required for high temporal coherence applications, such as creating stable interference patterns over time, however low coherence is associated with reduced speckle patterns in imaging

Monochromatic (narrow spectral bandwidth) light sources (e.g. a laser) have an increased spatial coherence compared to broadband polychromatic light sources, such as a white light bulb. Polychromatic light consists of multiple wavelengths, which distorts the phase relationship.

2.1.3: Refraction, Diffraction & Double Slit Interference

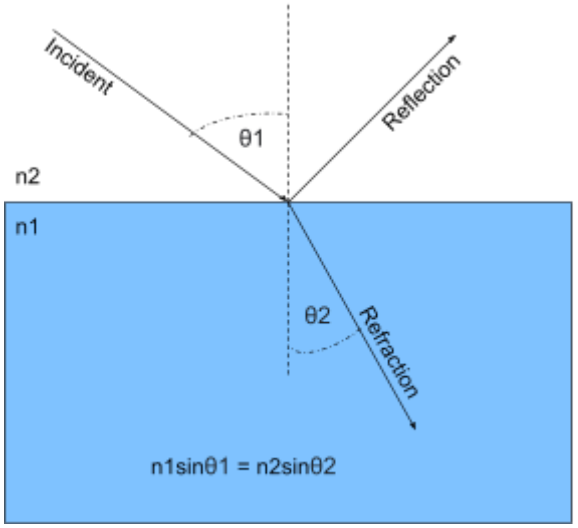

Figure 4: Refraction diagram

All mediums have an associated refractive index (RI) , defined as the ratio between the speed of light in a vacuum versus the speed of light in that medium. The speed at which light passes through a medium is inversely proportional to the RI of that medium. The magnitude of the RI also dictates to which extent the light passing through that medium bends, relative to the angle of incidence.[14]

Snell's equation describes the change in angle of the path of light as it passes across an interface between two materials of unmatched refractive index; $n_1 \sin\theta_1 = n_2 \sin\theta_2$, where n_1, n_2 are the RIs of the mediums either side of the boundary line. The angle of incidence is defined as θ_1, with angle of refraction being θ_2, both with respect to the normal line. This is described by Figure 4. RI is a dimensionless number (lacking units) as it is a ratio between the speed of light in a vacuum and the speed of light in a medium[14]. Spatial coherence of light is impacted by the effects of refraction, this can happen for a multitude of reasons, such as distortion from the surface of the boundary (i.e non-uniform surface), angle of incidence variation in non perpendicular boundaries, the change in light path and partial refraction where a portion incident light is refracted (i.e by a small object).[15]

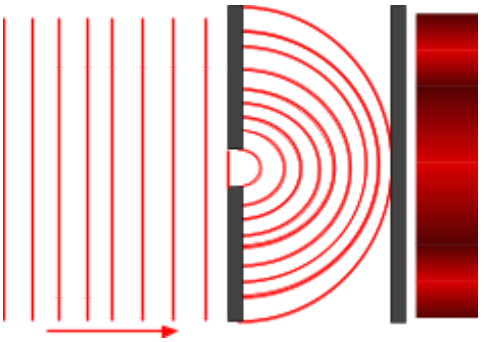

Figure 5: Diffraction diagram

Diffraction patterns form most prominently where a wave passes through a gap comparable to its wavelength; causing the light that passes through the slit to spread out. This forms a central, bright and wide band of light, with decreasing intensity at the edges of the central band, followed by a less intense band at the edges. The diffraction pattern is a result of constructive (bright bands) and destructive interference (dark bands). This phenomena is described by Figure 5.The central band (maxima) is inversely proportional to the width of the slit, as a result of increased light diffraction (spread) as the slit becomes comparable in size to the wavelength. [16]

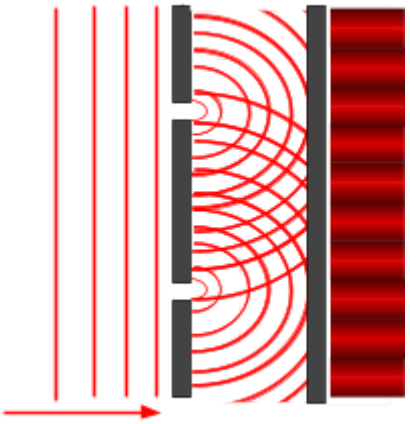

Figure 6: Double slit interference

Increasing the number of slits produces multiple, separate points where light can spread from. The light from these separate points can interfere with each other, both constructively and destructively, to form a repeating pattern of bright and dark bands - referred to as an interference pattern.This phenomena, often referred to as Young's double slit experiment [17], is described by Figure 6.

2.1.4: Scattering

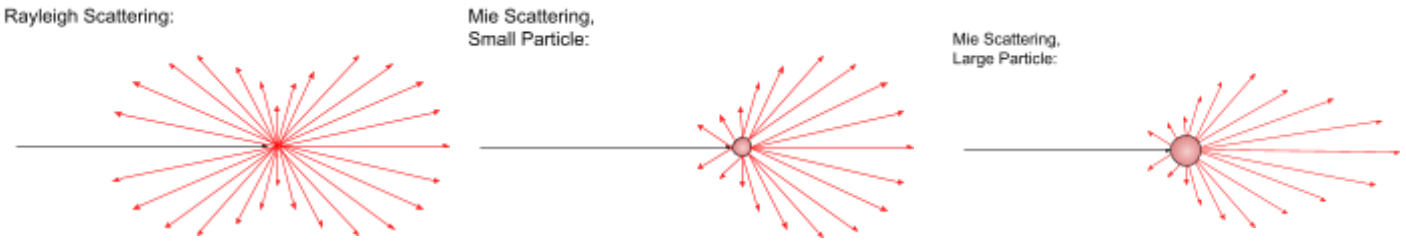

Figure 7: Scattering of Light diagrams

Waves traverse with a straight trajectory, only altering from this path when faced with non-uniformity in the medium, such as changes of refractive index or scattering from particle interaction. Different scattering patterns (Rayleigh, Mie) are described by Figure 7. [18]

Rayleigh scattering occurs when light interacts with particles which are far smaller than the wavelength. The intensity of scattering depends on wavelength, which is proportional to fourth power of wavelength ($I \propto \lambda^{-4}$); showing that blue light (smaller wavelength) scatters more efficiently than red light (larger wavelength) - this effect is the reason the sky appears blue, with polychromatic light from the sun scattering on small, atmospheric particles, as well as the transition gradient of reds towards dawn and dusk. Due to this scattering, and the E-field of the light oscillating perpendicular to the direction of light wave traversal, , the resultant light is mostly polarized. The Rayleigh scattering pattern is symmetrical, with stronger scattering in the direction of wave propagation as well as in the opposite direction, with weak scattering perpendicular to the direction of the wave at the point of scattering. [19]
Mie scattering occurs when the light interacts with particles of comparable size to the light wavelength. Mie scattering lacks the same "$I \propto \lambda^{-4}$ " relationship as Rayleigh scattering as a result of being less dependent on wavelength, scattering (white) light more uniformly. Mie scattering results in a pattern that is stronger in the forward direction, with the effect being more pronounced for larger scattering particles. 20]

2.1.5: Polarisation

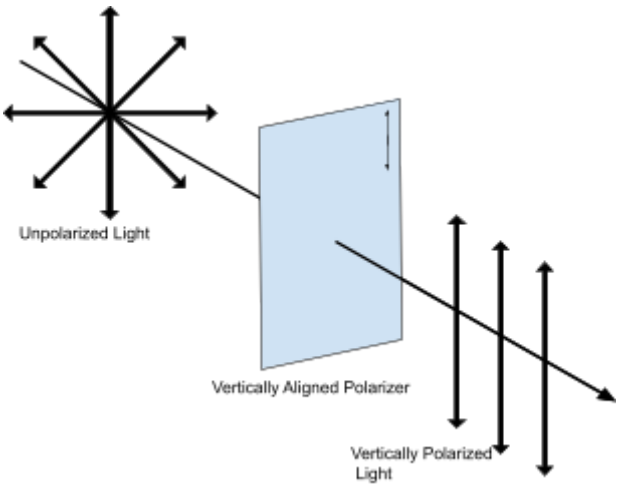

Figure 8: Polarizer Diagram

Waves can oscillate at any given orientation, even those produced by the same source may vary. However, these waves can become orientated - polarised - to oscillate in a single direction by use of polarising optical components (Figure 8) or naturally, such as rayleigh scattering via atmospheric particles. As sunlight is naturally polarised, polarising filters on glasses or in photography can reduce glare from reflective surfaces.

Polarisation can also be utilised in medical imaging, such as in optical microscopy, where a polarising filter is used to polarise the incident light, which becomes scattered (unpolarised) on interaction with a sample. A polariser set 90 degrees to the first allows for light scattered from the sample to be preserved while the incident light is reduced or extinct. This is particularly useful for viewing microscopic objects with birefringent properties (where the RI is dependent on polarisation and wave path through the medium), which in the context of biological samples include crystalline structures and organelles (cellular sub-structures).

2.2: Holography

Unlike photography, holography preserves the three-dimensional (3D) nature of the subject; allowing a recording of the subject to be viewed from multiple angles with a shifting perspective. These holograms are a product of coherent light interacting with a subject to produce a complex interference pattern, which is captured on photographic film.

2.2.1: History

Holography is a relatively young field of study; the origins of the field can be traced back to Dr Dennis Gabor, a Hungarian physicist. While working on improving the electron microscope technology of the time, Gabor's research led to the invention of holography with an outline of the system being reported in 1948; he was awarded the 1971 Nobel Prize in Physics for "invention and development of the holographic method" [20] .

2.2.2: System Design

In-Line Holography:

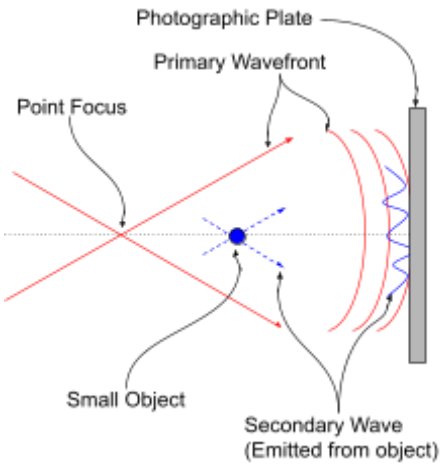

Figure 9: In-line holography Diagram

Figure 9 displays the experimental setup described by Gabor in his 1948 report "A New Microscopic Principle". This is an example of "in-line" holography [20]; where the reference light wave interacts with a small object, producing an object-scattered wave that travels along the same path as the reference. These two waves interfere with each other, producing an interference pattern that is recorded on a photographic plate or digital sensor in modern applications. With the intended purpose being associated with electron microscopy, the "Point Focus" represents a focused electron beam, with modern applications, the illumination tends to utilise laser technology; due to the coherent light produced.

In-line holography does not require complex alignment of mirrors or beam splitter components to generate separate reference and object beams. The lack of physical components means in-line systems can be more compact. Overall this results in a system that is conceptually simple, low cost, and robust to misalignment.

However, there are some disadvantages with this system design; such as being sensitive to motion and twin imaging. Twin imaging - where a real image and virtual image are superimposed - occurs due to the reference and object wave travelling along the same path, resulting in both waves being recorded at holographic film / sensor plane. Depth information is also reduced, as a result of the twinning issue. This overlap results in a reconstructed image that is unclear [21]. Motion artefacts occur as a result of distortion caused by the change in the light path, which for inline effects both reference and object beams as they do not follow separate paths.

Off-Axis Holography:

An alternative system is "Off-Axis" holography; where the reference beam and object beam are separate, but from the same origin, making use of components such as beam splitters and mirrors.

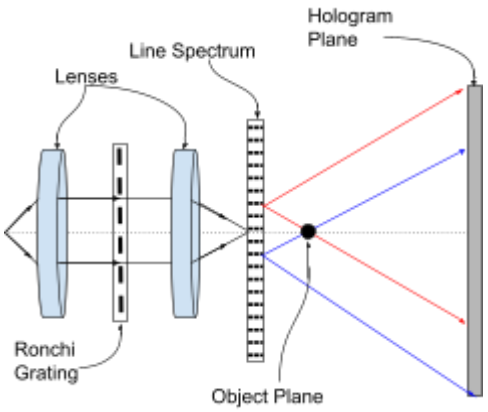

Figure 10: Off-axis Holography diagram

This system was originally described in "Reconstructed Wavefronts and Communication Theory"by Emett Leith and Juris Upatnieks [22]; Figure 10 shows their proposed system..

Off-axis was developed to address the issues with in-line systems. With this set-up, conjugate images that are superimposed with in-line designs are removed by spatially separating the two, this allows for a more coherent image reconstruction. The separation also increases the contrast of the interference pattern due to the lack of twinning as well as generating interference patterns with increased motion stability, with smaller motions having less overall effect on the interference pattern.

However, the drawbacks of this system is its complexity; with the addition of multiple alignment sensitive components, such as lenses, mirrors or beamsplitters, results in a physically larger system, which as mentioned, is sensitive to alignment issues. The addition of these components also results in a higher cost than a more simplistic system. Overall choosing between an off-axis system and an in-line system is the trade off between quality, cost and size of the system.

2.2.3: Transmission and Reflection Holograms

For either transmission or reflection holograms to be visible, the hologram needs to be illuminated by a light source, their difference however is how they are illuminated relative to the observer.

Transmission holograms require monochromatic light to pass through the hologram. This allows an observer with a backlit hologram to perceive the three dimensional information , allowing the observer to view the hologram at different angles to observe a shift in perspective of the holographic image. As transmission holograms use a monochromatic laser for recording, using polychromatic light will lead to a blurred reconstruction as white light will contain numerous wavelengths that do not match the coherence / wavelength that was used at the point of recording.[23]

Reflection holograms require front illumination to be visible; with the holographic image being seen by the observer when they are on the same side as the light source. Reflection holograms have the benefit of being able to utilise white / natural light, giving use in everyday life. Comparatively however, they are more sensitive to the angle of the observer than transmission holograms, with the three dimensional effect only being visible in a small spatial / angular window.[23]

2.2.4: Applications

Holography has a multitude of applications. The implementation of reflection holograms is becoming increasingly common as an anti-counterfeiting measure in banknote currency as well as official (government issued) identification such as driving licences and passports; while it is not impossible to generate holograms using commercially sourced equipment and materials, the replication of specific holograms would be a complex task and significantly reduces a forger’s ability to generate an authentic appearing counterfeit [25].

Transmission holograms are used in interferometry; where a coherent light source beam is split, each traversing a equal distance before being reflected back along their path by mirrors, recombined to generate an interference and then detected by a sensor. Distortions in the path of the light, caused by slight changes in the distance or changes of refractive index in an axis alters the interference pattern produced. This makes it useful for detecting slight alterations in object shape or position [26]. Transmission holograms also have use in the development of optical computing technology, which aims to utilise optoelectronics in data processing and computation, with the aim of offering increased speed and reduced power consumption compared to traditional electronics. Optical computing technology may also utilise holographic data storage, which has the potential to encode information in a three dimensional space, rather than two dimensional e.g. a disk in a traditional optical storage drive [27].

As for medical imaging, the field of holography allows for non-invasive, label free imaging of live cells, which can be visualised in two or three dimensional space depending on the system design and reconstruction method. This imaging allows for the shape, size, spatial position in volume, and internal organelles to be viewed [28].

2.3: Blood Analysis

2.3.1: Overview

Blood analysis encompasses a wide range of haematological diagnostic testing used within healthcare for diagnosis, condition monitoring and treatment monitoring of a patient. Patient health can be assessed by analysing the concentrations of the various blood components; such as indicating the level of function of organs, such as kidneys and liver, the presence of infection [30].

2.3.2: Cellular components of blood

Component	Purpose	Condition
Red Blood Cell (RBC)	Transportation of oxygen from inhalation in the lungs to tissues, transportation of carbon dioxide to lungs for exhalation	**High**: Suggest heart disease [31], polycythemia vera[32] **Low**: Potential anaemia, bleeding [9]
White Blood Cell (WBC)	Responsible for immune system response against foreign bodies / organisms	**High**: Typically infection, inflammation, potentially leukaemia[8] **Low**: autoimmune disorders, bone marrow disorders [7]
Platelets	Responsible for blood clotting	**High**: associated with cancers [33] or rheumatoid arthritis [34] **Low**: potential bleeding or bone marrow disorders [35]

Table 1: Cellular components of blood, their purpose & related conditions

2.3.3: Applications (diagnosis and monitoring)

Given the range of conditions that can be diagnosed with aid of blood analysis, it is often the basis for diagnosing medical issues. Blood analysis plays an important role in disease diagnosis; from a cellular point of view, the concentration of the different blood groups are indicative of potential health conditions, such as those listed in the “conditions” column in the previous section. Other blood components, such as glucose levels, can aid in diagnosis of diabetes or aid in the management of the condition [36].

Given blood analysis can aid in diagnosis of disease, it can additionally be used to monitor and track the patient’s response to treatment over time. This allows the effectiveness of treatment plans to be assessed for a particular patient. As mentioned, life long conditions, such as diabetes, can be monitored and assessed to maintain patient health. From a blood cell perspective, the impact of chemotherapy on patients' health can be assessed, as chemotherapy suppresses the production of WBCs, the WBC count can be used to assess the negative impacts of the treatment on the patient’s immune system [37].

The functionality of vital organs can be assessed via metabolic analysis. By analysing concentrations of glucose, cholesterol and electrolytes, organ functionality can be assessed. For example, high glucose levels may indicate the body's inability to regulate insulin, this would mean the organ (pancreas) is partially or completely non-functional [38].

Critically, blood analysis can be utilised for blood typing. Blood typing is essential in situations where the patient requires a blood transfusion or organ transplantation where donor compatibility needs to be assessed to avoid serious health complications [39].

To summarise, blood analysis is vital in modern day medicine and can be used for disease diagnosis, treatment assessment and in aid of medical procedures.

2.3.4: Centralised vs Decentralised Testing

Blood analysis is often handled by specially trained individuals, utilising high end laboratory equipment, at a centralised location, e.g. hospital laboratory. This allows for high accuracy results, as well as handling a broad range and large volume of tests. However, the turnaround time - the time from sample collection to result provided - can be lengthy for multiple reasons. Logistically, there is a handover period between sample collection and delivery to the laboratory, with particular care taken with the storage and transport of the sample to ensure it remains viable. There is also the time taken for processing and appropriate disposal of the sample. This may further inconvenience the patient by delaying diagnosis and treatment monitoring.

Decentralised testing, or point-of-care testing (POCT), aims to conduct diagnostic testing closer to the patient, either at home or a local clinic that lacks specialised staff or equipment. Decentralised testing results in faster result turnaround, improving convenience of healthcare for patients, as well as reducing the workload / volume of testing passed through specialised laboratories.

By engaging people with their health via convenient testing, fast or real-time feedback and user-friendly GUI, technology has the potential to empower people to manage their own healthcare[40], from a less clinical environment or even the comfort of their home. POCT devices offer a sense of control and freedom for those with long-term / chronic diseases which require regular and routine observation . Given the wide range of tests that encompass blood analysis, not all will be viable for POCT due to the test complexity.

POCT devices such as the ‘FreeStyle Libre’ allow users to monitor their blood glucose levels in realtime, track the trend of the levels over time (i.e rising or falling) as well as being alerted when glucose levels reach a high or low level. This allows diabetic users to manage their health in a way that provides them a larger degree of information, freedom and comfort [41].

2.3.5: Blood Analysis Using Haemocytometer:

Blood analysis using a haemocytometer is a widely employed technique in clinical laboratories and research settings for quantifying and analysing blood cells. This method involves utilising an integrated glass slide with a reference grid pattern to facilitate accurate cell counting [42]. The haemocytometer allows for the determination of cell concentration, evaluation of cell morphology, and identification of cell abnormalities. Morphology and abnormalities being indicative of cell health or linked to specific blood disorders, e.g. sickle cell anaemia [9].

A haemocytometer in design, is a microscope slide-like device that consists of a central chamber engraved with a grid pattern, which is further divided into smaller squares. The grid pattern allows for precise location and counting of cells. The chamber has a specific depth that ensures an even distribution of cells and a known sample volume for analysis such as concentration calculations.

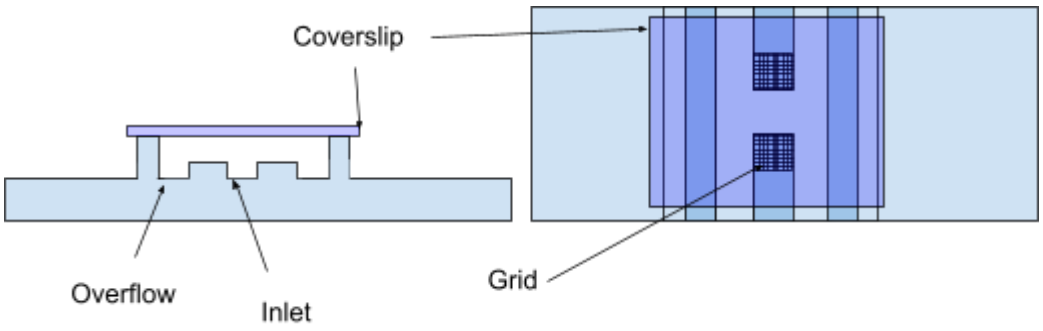

Figure 11: Haemocyctometer diagram

To perform blood analysis using a haemocytometer, described by Figure 11, a small volume of blood sample is diluted by a known factor to achieve an appropriate cell concentration solution . The mixture is then loaded into the chamber using a pipette. This solution is drawn into the sample chamber by capillary action, with the suspended cells settling on the reference grid. Using a microscope to image the gridded area, cells can be differentiated and counted, with information about concentrations of cell groups and cell health being recorded[42].

Haemocytometers offers standardised, and thus reproducible, procedure for blood cell analysis. The visual nature of the method allows for analysis on not just the relative concentrations of cell groups within the sample, but of their overall cell health, allowing blood disorders linked to cell abnormalities being identified. The method is low cost, requiring a minimal amount of specialised equipment to operate. Advancements of this method includes the introduction of computer vision to automate and increase the speed at which a haemocytometer can be processed[43]; however the static and limited sample capacity of these devices result in limited throughput .

This method is traditionally processed manually by a trained professional; this can be a lengthy and tedious process and subject to human error. A user must be trained in haemocytometer and sample preparation; as incorrect dilution or loading of the device can have an impact on the results of the concentration calculations or sample distribution. While lower concentrations would allow for increased usability, in terms lower number of particles to count, this potentially leads to the sample making it to the viewing sections not being representational of the undiluted sample, with errors / non uniform particle distribution having a larger impact.

2.3.6: Blood Analysis Using Coulter Counting:

Blood analysis using a Coulter counter is a widely used method for quantifying blood cells. This technique is based on electrical impedance to measure and count particles as they pass through a small aperture. The Coulter counter provides valuable information on cell size, count, and distribution, enabling the assessment of various particle types [44] (in the context of this project - blood cells).

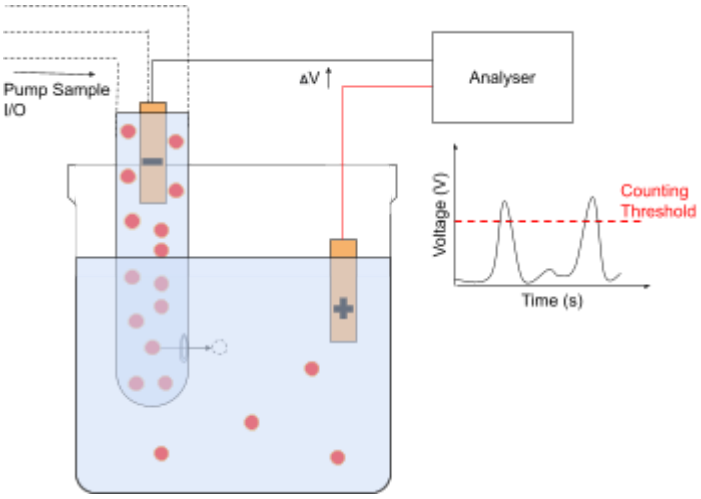

Figure 12: Coulter Counter diagram

A Coulter counter, described by Figure 12, consists of a sensing chamber and a small aperture situated between two electrodes. Cells are suspended in a low concentration solution, which flow through the aperture, where they cause changes in electrical impedance, which is detected and recorded by the device. The aperture size can be adjusted to accommodate different cell sizes, allowing for the analysis of various blood cell populations, also making it robust to obstruction. Plotting the electrical impedance over time will produce voltage peaks, each peak is the result of a particle crossing the aperture, with the peak magnitude corresponding to the size of the particle; allowing for both counting and size differentiation [45].

Coulter counters offer an automated, high-throughput alternative to the manual haemocytometer method, making it resistant to human error and decreasing the time taken to process a sample. The method allows for cell types to be differentiated, each cell type providing a different impedance change / voltage spike signature and is sensitive enough to provide size distribution information for the same cell group [45].

While Coulter Counters have use in bulk sample analysis, due to their sensing method being purely quantitative rather than visual, there is an inability to extract detailed morphological information from the data, as internal structures. This makes Coulter counting ideal for particle size differentiation and counting, though no functional characteristics of cells would be captured, which tends to then require a microscopy or flow cytometry for further analysis.With differentiation being purely based on particle size, coulter counting is susceptible to errors when the sample contains particles of a similar size or when multiple particles to be detected at once, such as the RBC density in blood [45] [46]. With variance in cell sizes within the same group, there is the potential for overlapping ranges between different cell groups, which increases the potential for error when applied to cells, especially in cases where the sample contains cell populations that exhibit a high level of heterogeneity or overlapping ranges in size.

Due to the reliance on changes in concentration / movement of particles through an aperture as the sensing mechanism, Coulter counting is extremely sensitive to sample dilution errors or the effects of improper sample handling, affecting the overall accuracy and precision counting data.The electrolytic solution used in Coulter Counting must be carefully sourced / prepared inorder to have a well defined conductivity and free from impurities, which will contribute to additional background count (error), which affects cell counting, for example bacterial studies [47].

To summarise, the Coulter counter approach to blood analysis allows for the automated and accurate measurement of particle size, though lacks the morphological benefits of visualisation based method that would aid in distinguishing groups of overlapping size ranges. The high throughput analysis is a benefit to analysing samples in bulk, however the sample preparation is critical for accuracy and precision in terms of correct

dilution and handling. Overall, Coulter counters are an essential tool in clinical blood analysis where manual, low throughput methods are not appropriate.

2.4: Lensless Digital Holographic Microscopy (LDHM)

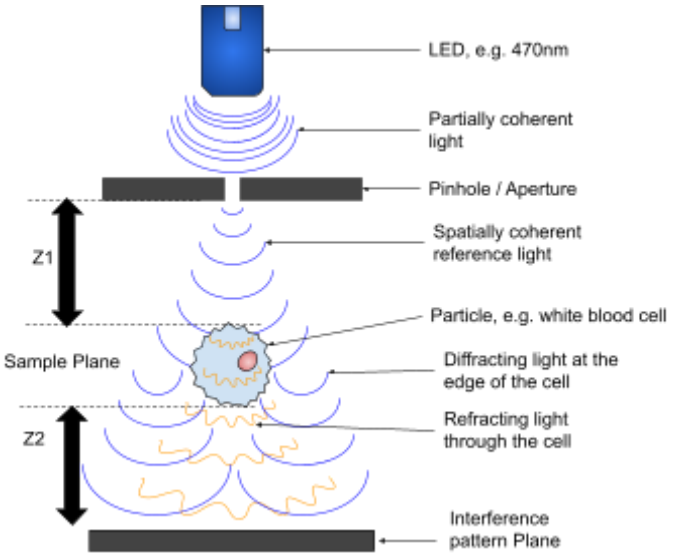

Figure 14: LDHM Diagram

Lensless Digital Holographic Microscopy (LDHM) utilises an In-line style system design. This design style, while having reduced reconstruction quality compared to off-axis design, opts to use less components (e.g. Lenses, beam splitters, mirrors) to allow for a compact , low cost and simplistic design.

2.4.1: System Design & Operation

Light Source

The light source chosen in an LDHM system is crucial to the quality of the imaging. Ideally, the chosen source should be spatially and temporally coherent. Spatially coherent light results in a stable phase relationship between wavefronts over distance, which is paramount for ensuring stability in the final interference pattern. A temporally coherent light has a constant wavelength overtime which is important for maintaining the constant phase relationship of the light, generating a stable interference pattern.. The wavelength of the light source has an impact on the resultant imaging quality. Use of shorter wavelengths, such as blue light, increases the resolution of the imagery, due to the smaller diffraction limit of the light, however, blue light is less effective at viewing thicker samples, as the light has a short penetration depth. For viewing thicker samples, red light becomes a competitive choice, offering deeper penetration into the sample though the resolution of the imagery is compromised by the increased diffraction limit. Therefore the sample is a key factor in choosing a system wavelength [28].

Laser sources are prime candidates due to the coherent, monochromatic (narrow band) nature of their light. However, Light Emitting Diodes (LEDs) are an alternative to laser components, offering benefits such as significant reduction in cost, being readily available and having less operational safety concerns. While LEDs do not provide the same degree of coherence, the system can be designed around this. There are relatively narrow band LED components available, with the emitting light being able to be passed through a pinhole/aperture to increase its spatial coherence [48]. Being lower power components, LEDs also allow for a system that only requires a lower power input, such as a 5v USB connection. The low power nature of LEDs also reduces the heat dissipation of the light source, which reduces the damaging effects of static, live biological samples when

imaged over longer periods of time. With standard LEDs being similar in terms of required voltage, the LED in the system can be easily replaced with an LED of any wavelength for testing or optimisation purposes as well as ease of repair.

Pinhole / Aperture

Smaller pinholes / apertures increase spatial coherence [50], this is due to a pinhole restricting the light that passes to a narrow angle, resulting in less divergent rays passing, meaning in light that is more coherent after the pinhole - this is referred to as a spatial filter. The smaller the pinhole, the more restrictive this filter becomes. Should a pinhole size be comparable to the size of the wavelength of light that passes through it, the light will diffract rather, causing the resulting light to spread and reduce spatial coherence and intensity. The size also affects the overall intensity of the illumination of the sensor, as the size decreases, the amount of light passing through the pinhole decreases, which greatly reduces the intensity.

Polarizer

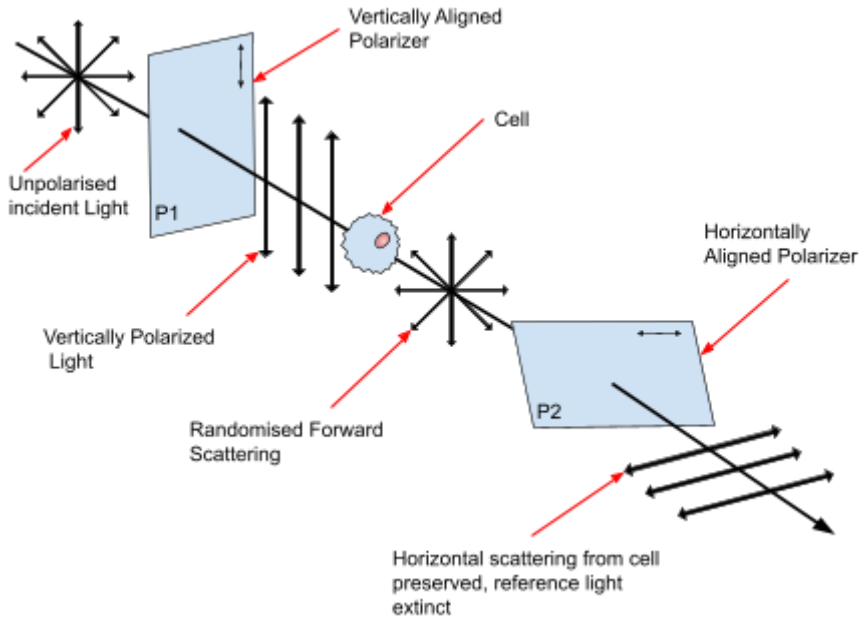

Figure 14: holography polarisation implementation diagram

The guiding theory behind polariser implementation was the potential to remove the background signal associated with the unscattered component of the input light source while preserving and sensing the light information from the light scattered by the sample.
This could be achieved by using a polarising film, P1, above the sample to polarise the input light source which, on interaction with the sample, would scatter and become un-polarised. This would allow a second polarizer, P2, below the sample, set at 90° with respect to P1, to remove the polarised light components from the source, while also allowing the unpolarised scattered light to pass through to the camera sensor. This application is described by Figure 13. The testing for polariser implementation will be discussed in the following section.

System Geometry (Z1,Z2)

For in-line holography systems, the relative sizes of each section along the working distance is just as important as the specification of the components. The total working length of a LDHM device can be thought of as being composed of two sections, ‘Z1’ (Light Source - Sample distance) & ‘Z2’ (Sample to Sensor distance). The distance parameters of Z1 and Z2 are invaluable to design and optimisation of a LDHM device.

Increasing the distance Z1 results in increased spatial coherence of the light as it reaches the sample plane, generating holographic interference patterns of greater quality[28], where the interference pattern rings produced are more distinct, having a higher contrast between bright & dark rings. This in turn generates reconstructed images of higher quality, with details appearing sharper and of higher contrast. Contrast of the final reconstruction has been chosen as the metric for image quality ; this was due to computer vision techniques responding better to high contrast images for the purposes of differentiating between object(s) & background boundaries.

Increasing the parameter Z2 has a magnifying effect. The magnification of the system, as there are no magnifying lenses integrated, relies on the ratio of these two sections. As the sample to sensor distance, Z2, is often negligible when compared to Z1, the magnification can be considered unit, with the magnification being linked to a change in the Z2 distance.[28]

Sensor

LDHM systems utilise a high resolution digital sensor to record the holograms, unlike traditional holography that uses a physical recording medium, e.g. photographic film. The digital sensors can be either charge-coupled devices (CCDs) or complementary metal-oxide semiconductor (CMOS) camera sensors.

CCDs are the superior option for image quality, offering a higher degree of pixel uniformity (where the pixel cohort has a more consistent response allowing for increased image data recording accuracy) and dynamic range (which increases contrast sensitivity of the sensor). CCD technology is less prone to the effects of digital noise compared to CMOS[51].

CMOS sensors however, offer greater readout speed than their CCD counterparts, which is particularly useful for applications where there is real-time or close to real time tracking or observation of a sample is required. The increased frame rate (frames per second, FPS) allows for moving objects to be imaged in a smoother transitioning data set, which when coupled with the faster readout speed, reduces motion blur, which is useful in applications such as a flowing sample in microfluidics. CMOS technology typically uses less power, resulting in a system that is more portable with use of integrated battery power supplies or utilising low power sources such as USB connections. CMOS additionally are lower cost than their CCD counterparts. [51]

2.4.2: Image Reconstruction

Producing high quality holograms is only half of the battle in holography; the holograms need to be reconstructed into images that are interpretable by human or computer vision software. To reconstruct these images, software that applies a wave propagation model technique to the image in order to digitally recreate the scattering object from the interference pattern. There are multiple options to choose from in terms of method, each with its own advantages and disadvantages.

Angular spectrum method utilises Fast Fourier Transforms (FFTs) to back propagate the wavefield to the point of the object plane, utilising fourier transforms to dissect the hologram into separate spatial frequency components which represent the angles of light in the wave propagation [52]. Angular spectrum method is applicable for applications where the distance between the object and the recording medium is large, relative to the wavelength of light used in the LDHM system; this distance is given same parameter as Z2, with the wavelength being defined by the LED / laser source in use. This makes the method effective at medium to far distances rather than near-field applications.The method essentially simulates the wave propagation backwards from the hologram to the object, a distance variable is used to reconstruct backwards to the object plane - this is particularly useful in 3D samples, for example a microfluidic channel, as by varying the the distance variable, you can reconstruct particles (cells) that are situated in different object planes. Using FFTs, which some programming languages support natively or have supporting libraries for, enhances the computational speed of the reconstruction, shortening the required software run-time for reconstruction. This method however can be sensitive to noise, which reduces the overall quality of the final reconstruction.

Rayleigh Reconstruction utilised the Rayleigh scattering model mentioned in a previous section; using the scattering model to reconstruct the image based on the scattering and intensity of the resultant hologram. Though for Rayleigh scattering to be prominent, the particles viewed must be smaller than or comparable to the wavelength of the light. Due to the scale of the light scattering and interactions, this method can be computationally intensive.

2.4.3: LDHM Design Summary

LDHM devices are robust by nature; as an in-line system, there are few physical components and no need for the alignment of lenses or mirrors. This allows for a device that is quite stable to misalignment by damage (i.e knocks or drops). The components used; the light-source, pinhole/aperture and camera, are not required to be particularly specialised, allowing a variety of component sizes, standards, and variables to be used. The pinhole / aperture diameter used can vary, with satisfiable results ranging from tens of microns to up to approximately 100μm [48]).This allows for a system that is flexible, allowing for optimisation for a multitude of different applications. As such it is easy to find components that are compatible with the same optical development tables (e.g. Thorlabs items), or appropriate for custom housing. The alignment robustness as well as customised housing reduces the introduction and obscuring / blocking effects of Foreign Object Debris (FOD), such as dust or other environmental particulates.

The section geometry of a LDHM device is designed so that Z1 >> Z2, e.g. Z1 = 10cm, Z2 = 100μm, allowing for a Z1+Z2 length being approximately 10 cm . This system size allows for a design that is compact, lightweight and portable. With Z2 being on the micron scale, the sample plane is extremely close to the sensor plane, allowing the magnification of the image to be approximately ‘1’ [53]. This means the image generated by the sensor is comparable to the real size of the objects, the image being the total sensor size, or the resolution of the image multiplied by the sensor pixel size should the resolution be set to lower than maximum. This provides a wide field of view (FOV) [48], making it possible to analyse a larger sample area; the larger data set allowing for reduction of the impact of anomalous data caused by factors such as non-uniform sample distribution in terms of cell spatial distribution or cell type distribution across the sensor plane.

The digital format of the image output is particularly useful, as it allows for the potential for the technology to be linked with a computer for automation of data collection and/or analysis. Automated data collection may aid untrained individuals in correct device operation. Automated data analysis will reduce the requirement for human processing, which like manual haemocytometer use, is a lengthy and tedious task. Overall, this would reduce the workload allocated to collection and processing centralised tests, as well as decrease the lead-time of results, reducing the strain for medical professionals, and providing a faster service to patients

Given the sensor size and sample channel size being small, LDHM technology can utilise small quantities of sample fluid, e.g. blood - which given the cell density of blood may allow for minimally invasive sample collection, such as a finger prick. Samples can be diluted if necessary - which may be the case for particularly dense samples - which can be imaged and analysed in real time using a microfluidic delivery system and computer vision software.

The cost to produce a LDHM device is low; as mentioned above, there are few components that can be relatively low cost and readily available. The technology is compatible with consumer grade computers, allowing for data processing without expensive or specialist computer systems.

The robustness, in conjunction with its handheld size, low complexity and integration of automation / high FOV computer vision features gives LDHM technology great potential for translation into point-of-care / at-home diagnostic technology.

2.4.4: Biomedical Applications

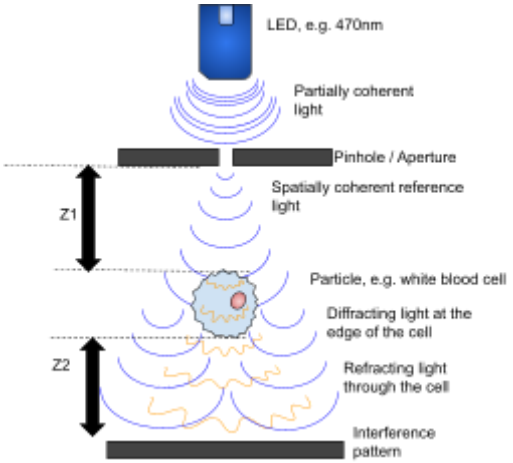

Figure 14: LDHM Diagram

A biomedical application of LDHM imaging is described in Figure 13. Due to LDHMs non-invasive operation, it has become a competitive emerging biomedical technology for high resolution imaging, particle / cell differentiation and tracking of biological samples. With in-line holography allowing for a compact system, as well as the LDHM being compatible with low-cost components, the technology translates well for blood cell analysis applications.

LDHM has the potential to produce detailed images of blood cells, which allows for the differentiation and counting of specific blood constituents e.g. RBCs, WBCs [54]. This cell count could provide fast testing, allowing for indicators of issues, such as infections or anaemia. With higher detailed imagery than is required for counting, there is the potential for LDHM to identify cell shape issues and anomalies, such as those associated with Poikilocytosis or Leukaemia. This testing could be utilised as a condition or treatment monitoring method, with test results being compared over a period of time.

LDHM outside of blood cell analysis has applications such as tracking biological sample growth over time, tissue engineering and pathogen identification. The technology is viable for these applications due to its non-invasive / non-destructive operation, allowing for prolonged testing periods without ill effects on the sample.

Comparison with competitive technologies:

LDHM allows for high throughput imaging, with a relatively large volume of sample being imaged compared to device size, especially when coupled with microfluidic flow channels, due to the observable field being equal to that of the size of the physical sensor at unit (‘x1’) magnification [53]. As the sensing area can be quite large, a range of sample dilutions can be used, as long as the particles are dilute enough to avoid stacking and clumping of particles / cells. This allows, even at low concentrations, better averaging for particle count, compared to smaller viewing methods, such as a haemocytometer. Haemocytometers in comparison have a lower throughput, being limited to small samples due to their manual method, low chamber volume and low FOV (due to traditional microscopy [48]) . For both LDHM and haemocytometers, pH of the sample is of little concern, as long as the pH is not at destructive levels for cells or the device. Compared to these methods, Coulter Counting has a much superior throughput [55], making it suitable for processing bulk samples automatically, however it is very sensitive to dilution and pH, significantly affecting the measured impedance by altering the conductivity of

the suspension medium, due to the sensing method being based on changes of electrochemical impedance due to movement of particles through an aperture.

In terms of visualisation, LDHM technology allows for digital images of cells, though this is produced by image reconstruction. These images are often monochromatic, as polychromatic images require a more multi-light source integration and increased complexity of the software required for reconstruction [48]. The reason separate coloured light sources would have to be utilised, rather than a combined source that produces white light, is that the resultant interference pattern would be a stack of all the interference patterns of the light components, producing a blurred interference pattern that would be difficult to extract information from for image reconstruction.The nature of visualisation in LDHM systems makes the technology effective at tasks such as counting objects, however detailed morphological analysis can be bottlenecked by the design, inline systems produce images of lower quality due to the presence of twinning [21], as well as the optimisation of the system for cell viewing .Traditional optical microscopy, using tools such as the haemocytometer offers direct visualisation of the cells / particles, allowing for instant viewing for a user, camera or computer. The image produced is naturally coloured, though users may include use of stains / dyes for viewing cells, as well as allow fine details of cell shape and structure to be viewed. Both visual methods can suffer from a stacking issue, where cells are situated in a vertical stack to the viewer - obscuring one or more cells, which produces a counting issue. Other technologies produce statistical data opposed to viewing, such as Coulter counter technology, which allows for rapid processing of size / count information [45] but provides little detail about the morphology of the subject.

LDHM offers a wide FOV, which in designs where the Z2 parameter is negligible, the magnification factor is approximately one, producing a FOV that utilises the entire sensor size[48]. This is an advantage over traditional methods, where the FOV is inversely proportional to the magnification, meaning that the area of the sample viewable is reduced with magnification [48]. Coulter Counting technology has no field of view, as there is no visual element produced, however in terms of capturing information as it passes through the aperture, which acts as Coulter Countings sensor mechanism, the method typically captures a single particle passing the aperture at any given time - as multiple particles passing through in close proximity can be registered as a single, larger particle, similar to the stacking issue presented in visual methods.

LDHM, while not an automated method in itself, can be coupled with concepts such as microfluidics and computer vision to design a system that achieves automated imaging, differentiation and counting of particles, as well as potentially carrying out morphological analysis. Similarly haemocytometers could also be advanced by implementing similar computer vision technologies, however as mentioned their throughput makes this less effective than when applied to LDHM systems, though it can reduce the labour involved for simple analysis [43]. Coulter Counting is naturally an automated process, needing no adaptations in its methodology, which is ideal for counting in bulk samples, but is not effective if there is a need for visualisation.

LDHM system design is highly flexible, allowing the system to be designed in a made-for-purpose manner; allowing the inclusion or exclusion of multiple components, parameters such as LED wavelength being altered based on subject and Z geometry being varied for either function or ergonomic purposes. Design variations such as off-axis holography and inclusion of lenses offer additional benefits, such as increased depth perception and resolution , however system complexity and cost both increase. Haemocytometers however are more standardised, with little variation between manufacturers, though this keeps the function consistent. Coulter Counters find a middle ground in this regard, they are rigid in the sense that they require specific equipment to function, though they can be applied to various sample types, with the sensing thresholds can be altered in the user software.

LDHM systems range in their portability, based on their designed purpose. As the design is flexible, the system design can consider size, weight and overall portability. With a limited number of components required to build a LDHM system, the design is naturally quite compact, with most of the length being attributed to geometry considerations. This allows for LDHM to be designed around the concept of point-of care diagnostics, as

portability is a major factor for at-home or decentralised use [56]. Due to their simple design and manual function, haemocytometers themselves are highly portable, allowing multiple being transported to a user, i.e a laboratory, at a single time, however a secondary device, such as a traditional microscope, is still required to visualise the cells on the haemocytometer. However, despite their portability , their manual use makes them unsuitable for untrained individuals to use. Additionally, given haemocytometers are often used with traditional microscopes, the FOV that is observable is reduced due to the method of image magnification. Coulter Counters are non-portable devices, with the device size (for current commercial products) being quite large. For example, the "Multisizer 4e" Coulter Counter from "Beckman Coulter" - a notable company in the scientific instrumentation / Medical device market - has dimensions 61cm x 64cm x 51 cm, with a weight of 45kg [57]. This means samples have to be taken to the device's location, rather than to where the sample is located / taken from - this makes it unsuitable for use in point-of-care diagnostics.

LDHM systems are low maintenance, their components are readily available, and generally low cost for replacement or repair purposes. There is no need for recalibration of the device, as all variables in a final design are generally fixed, and given the aperture/pinhole used is quite large the systems are resistant to misalignment and FOD-blocking [48]. Making use of internal drivers for the lightsource and enclosed camera (ambient light having no effect), the function remains stable overtime. However in terms of mechanical stability, physical motion can affect the quality of the results, making designs that are compact / low centre of gravity / with a heavy base beneficial. Haemocytometer durability depends on the type used, as reusable glass and disposable plastic options are available. Glass haemocytometers requires rigorous cleaning to avoid cross-contamination, making disposable options beneficial for biohazard use. Being manual devices, there is no calibration past initial microscope focusing, the device includes a referencing grid for sizing and spatial referencing. Coulter Counters fall short in this regard, requiring regular calibration and maintenance to ensure result accuracy and device function.

When making use of automation, LDHM requires minimal user labour during run-time. During set-up, the user would be required to ensure the sample is appropriately diluted, as well as inserting microfluidics and ensuring the software parameters are correct. Due to its visual nature, LDHM technology could in theory be used for manual use, which would be an extremely high labour task, especially if using the entire sensor size, as the FOV is far greater than other manual methods, i.e. haemocytometers, which have a reduced FOV but are still labour intensive to analyse. As mentioned, with Coulter Counters being a naturally automatic process, they are minimally intensive during run-time, though require precision with sample dilutions as well as knowledge of specialist equipment for initial set-up.

Being an emerging technology, there is little to no commercial options or support for LDHM systems, meaning currently most LDHM systems are bespoke. LDHM systems can make use of low cost, readily available components, which results in LDHM designs being low cost; though their bespoke nature incurs cost from the time taken for R&D, prototyping and validation prior to implementation. Conversely, haemocytometers are designed around a known standard, resulting in their ability to be mass produced and brought in bulk, therefore reducing the commercial price per item. Coulter Counters, though having a commercial presence, are expensive, relying on specialist equipment and being a specialist device themselves, making them only cost effective for regular high-throughput / bulk sample quantitative analysis as opposed to visual.

Overall, LDHM technology offers similar benefits of traditional, direct visualisation methods such as haemocytometers while also supporting high throughput and automation similar to methods such as Coulter Counting. The cost, size, robustness and simplicity of LDHM systems uniquely aligns itself as having potential for point-of-care diagnostics, without having input from trained individuals or relying on expensive, specialist equipment.

3: Design Experiments & Considerations:

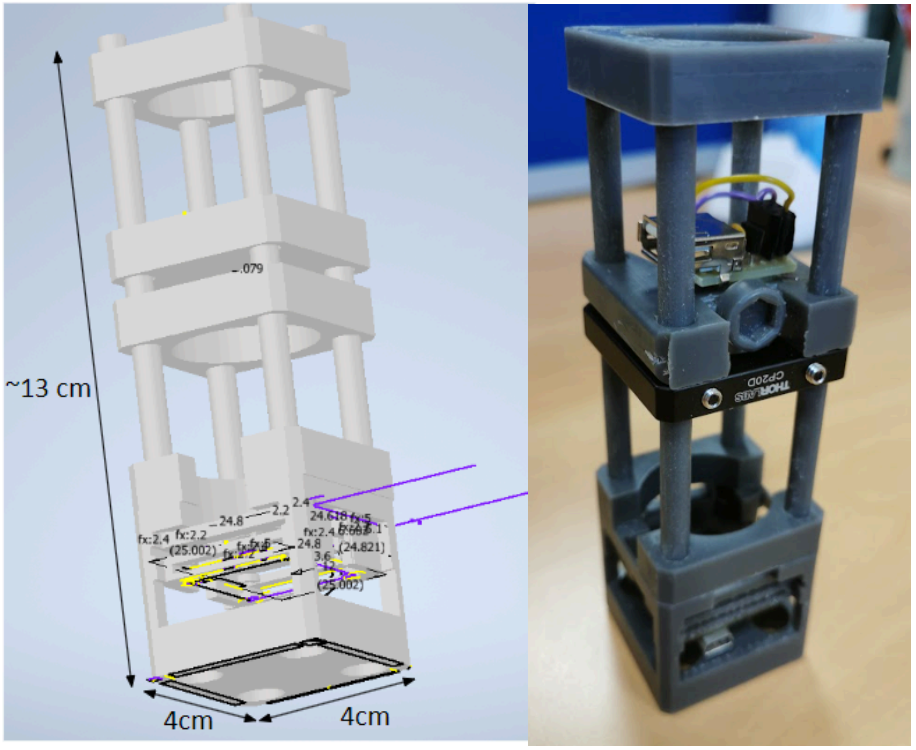

Figure 15: LDHM Experimental Set-up (variable geometry parameters), 3D model and prototype

To design an optimised system, the parameters of an LDHM system had to be thoroughly investigated.

Originally an optical workbench was used for preliminary experiments, which aided in constructing a variable set-up that allowed for moving sections and open access to the components. However a smaller design, Figure 15, was then implemented, influenced by the functionality of the optical workbench, which allowed for testing on a similar scale, handheld, as the intended for the final design.
The open style of this set-up allowed for components to be easily moved in a vertical direction whilst maintaining alignment, as well as allowing components to be changed (e.g. LED, Pinhole) whilst maintaining known section distances.This design was compatible with thorlabs components, making use of an Thorlabs aperture and pinholes for pinhole size experiments.This design allowed for the ‘Z1’ parameter to be easily changed by sliding the relevant component up or down the poles; the ‘Z2’ parameter was varied by placing 3D printed spacers between the camera and the sample.
The camera was fixed in place by M2 screws inserted into a deep seated M2 nut that was inserted into the 3D printed base.

3.1: Artificial Blood Sample

Clinical samples, in this case human blood, are difficult to work with. Blood can be a transmission vector for many diseases, such as HIV and Hepatitis, increasing the risk to those handling the sample. In the liquid form, there is additionally a greater chance of cross contamination from improperly sealed microfluidics or from mistakes in handling; given the health risks involved, and for sanitary reasons, contaminated equipment would need to be disposed of or thoroughly disinfected. There is also an ethical component to blood-work, e, resulting in blood not being able to be self donated while third party donors are required to be fully vaccinated and providing written consent, for which documents would need to be generated. Donated samples would need to be correctly disposed of, to avoid the risk of potential identification of the donors based on DNA material.

The reasons highlighted above led to the decision to use an artificial blood sample, that being a suspension of polystyrene beads, with comparable size and colour to that of the constituents of blood. The size of the particles in use are a 2µm red bead, acting as the mock RBC and a 10µm blue bead acting as a dyed WBC, albeit slightly smaller than their real counterparts. With the particle sizes being slightly smaller than real cells they would still be appropriate for experiments such as magnification & resolving factor, as viewing smaller particles is a more challenging task than larger particles - though this would mean for any size based identification, i.e. settings in software, there would have to be investigation into cell specific measurements.

An artificial sample allows little to no health risk, with accidental contamination being low risk and easy to clean. Additionally artificial blood is not subject to no ethical approval, though health and safety documents were generated by its users prior to handling. Artificial samples also offer greater manipulation of the concentrations of the mock cells, allowing for experiments to be run with either mock RBCs, WBCs or a mixed sample, which is very useful when troubleshooting issues, particularly within software, relating one size or colour of bead.

3.2: Section Size variables:

3.2.1: LED - Sample distance (‘Z1’)

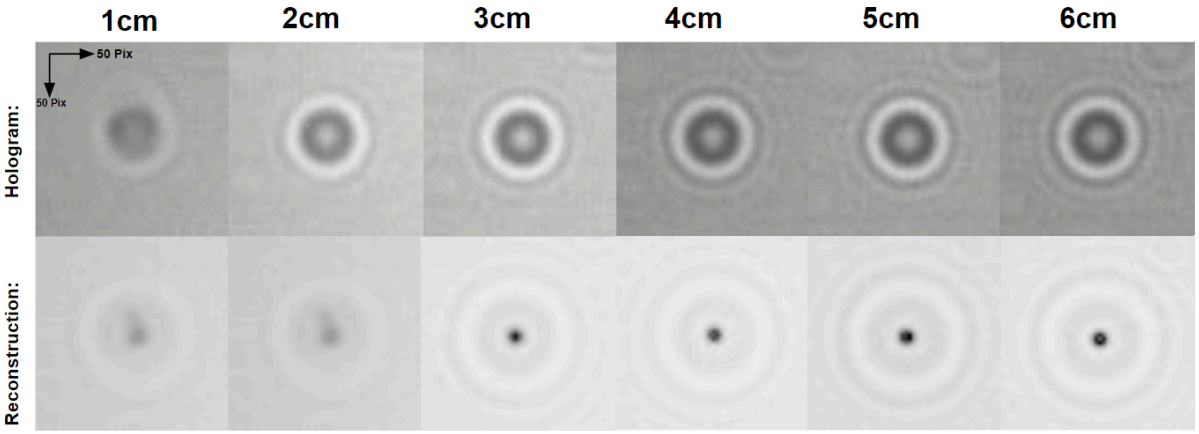

Figure 16: Experimental Image Data; ‘Z1’ variable, holographic & reconstruction images

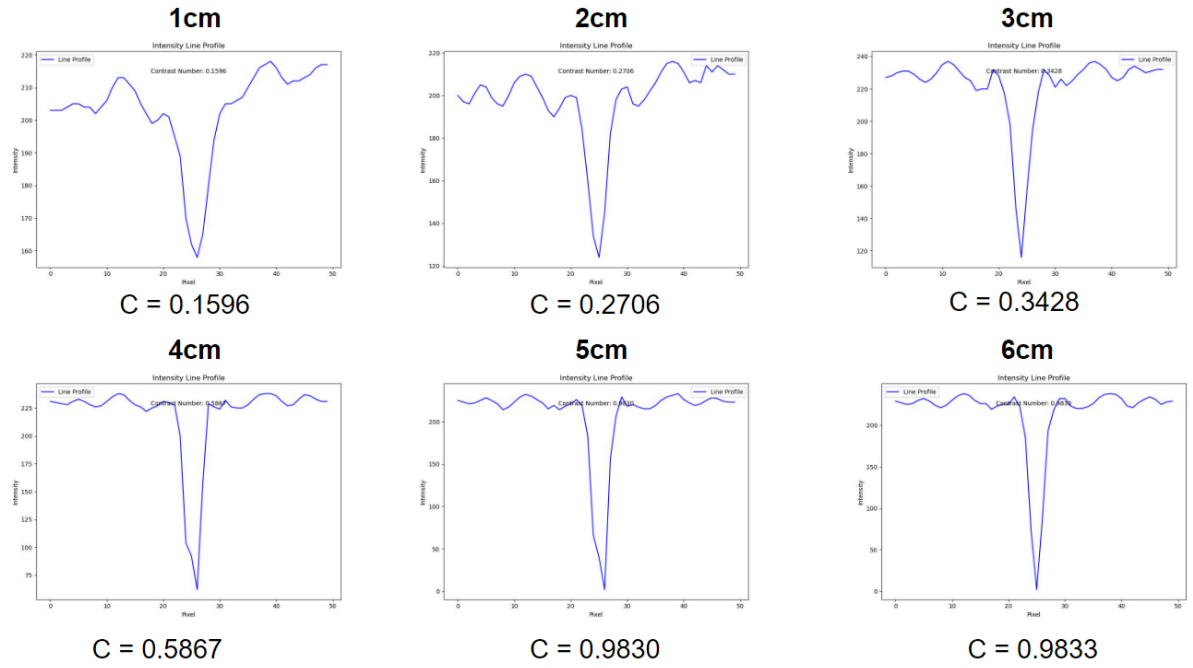

Figure 17: Experimental Image Data; 'Z1' variable, line profiles

Figure 16, shows the generated hologram and reconstructed image of a 10µm sphere as the Z1 parameter is varied. From the holographic images, there is a clear progression in quality in the distinction of the interference rings generated, this is reflected in the image reconstructions. To highlight this progression, a line profile was taken across the centre of the reconstructed particle and the contrast calculated. The line profiles, shown by Figure17, show the peaks generated by the particle increase in sharpness and height over distance - highlighting that increasing Z1 generates images where the particle is both easier to discern from the background and sharper.

3.2.2: Sample - Sensor distance ('Z2')

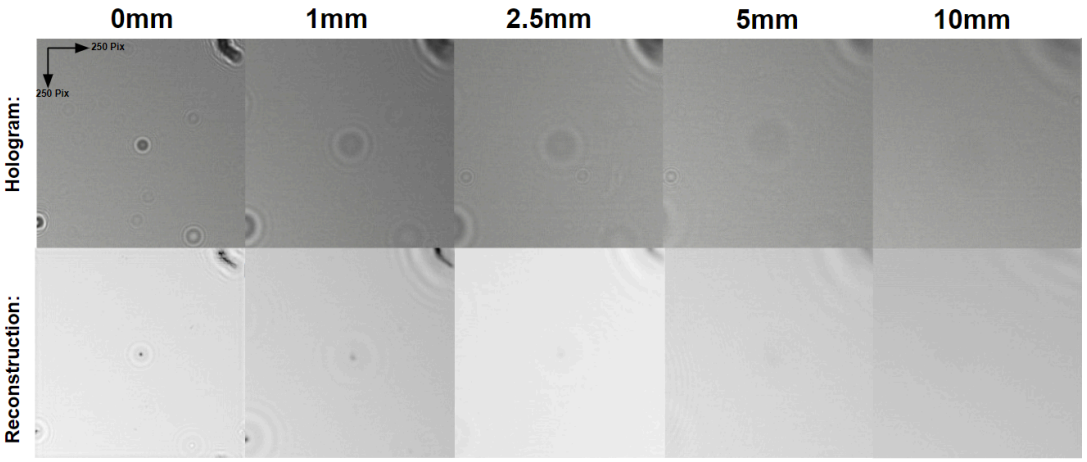

Figure 18: Experimental Image Data; 'Z2' variable, holographic & reconstruction images

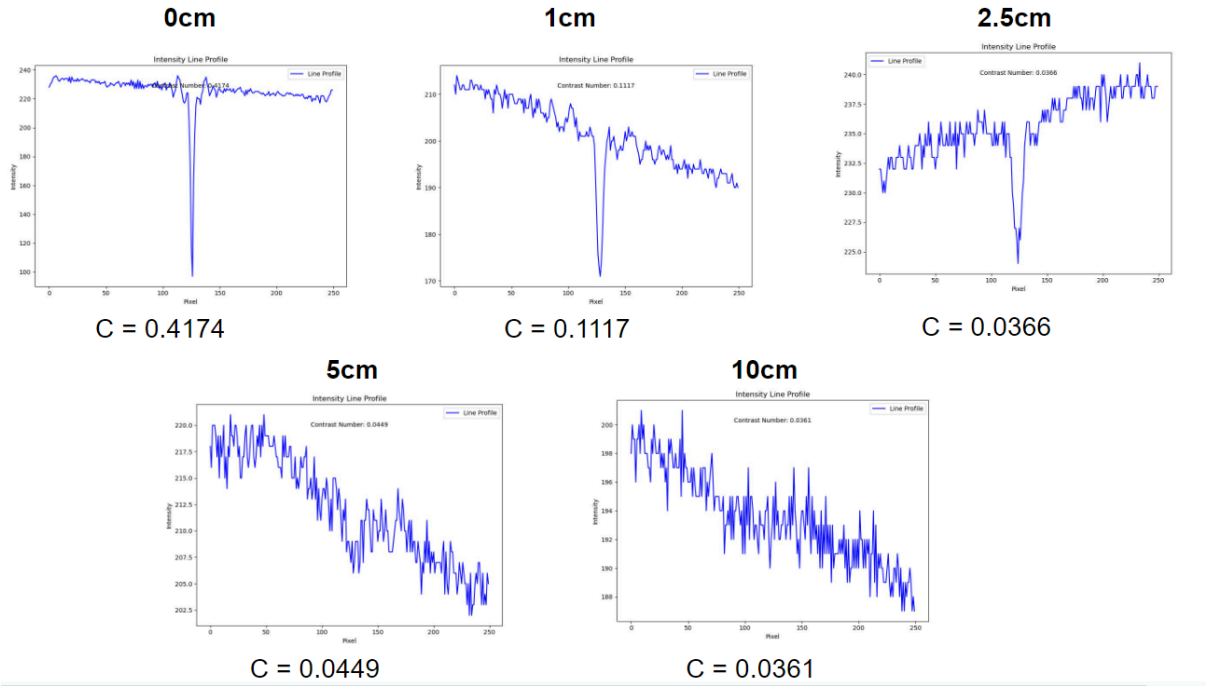

Figure 19: Experimental Image Data; 'Z2' variable, Line profiles

Figure x, shows the magnification of a particle as the parameter Z2 is increased. As shown, the hologram of the centre particle is magnified with increased distance, though this has a detrimental impact on the quality of the hologram and the related reconstruction image. As the particle is magnified, the line profile (shown by Figure 19) shows a decline in contrast over time, with the peak broadening and reducing in depth, eventually being indistinguishable from the background. The contrast calculation for the last two images do not fully represent this, as the peak is lost and the calculation is based off min/max values rather than relative to the position of the peak. The increased magnification additionally lowers the field of view (FOV) which is not ideal; as it limits the observable by the sensor, potentially increasing the impact of anomalies in the sample, such as a non-uniform distribution of particles.

3.3: Aperture Experiments

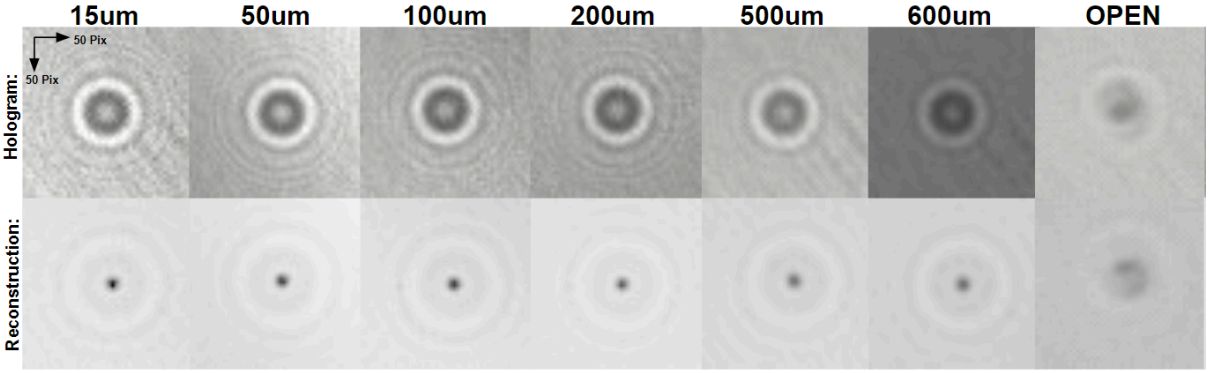

Figure 20: Experimental Image data; Aperture Variable,Holograms & Reconstruction Images

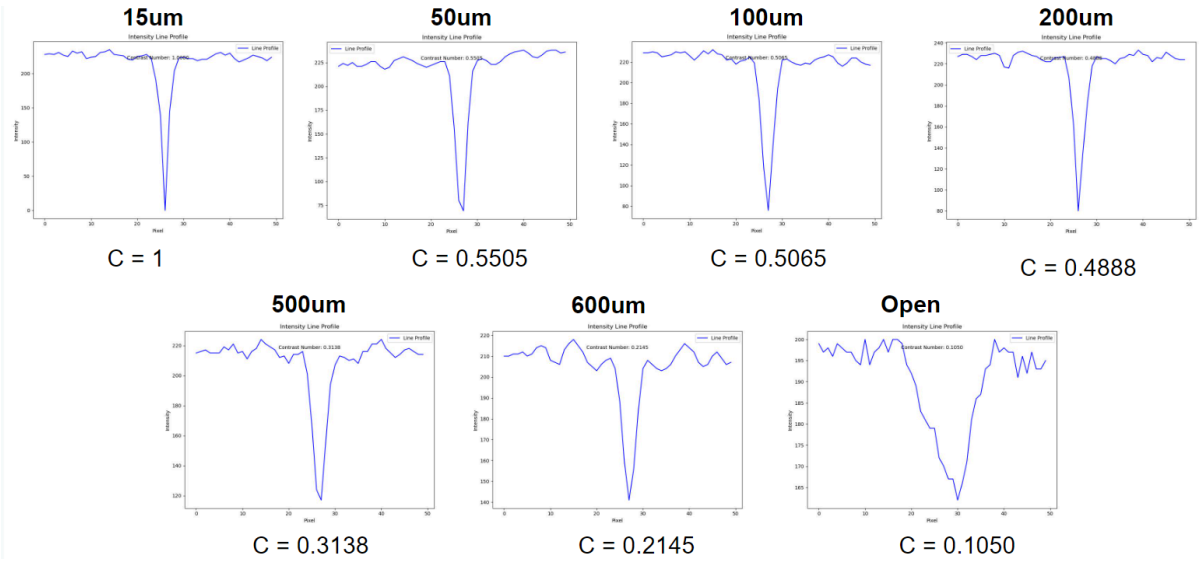

Figure 21:Experimental Image data, Aperture Variable, line profiles

Figure 20, shows the effects of varying the aperture diameter on the hologram and reconstructed image quality. As mentioned, a benefit of LDHM systems is the possibility of using a larger aperture, which decreases the risk of full or partial obstruction. The data above, Figure 21, shows an inverse relationship between the aperture size and the resultant contrast of the reconstructed image, with 15µm (the smallest pinhole tested) providing a unit contrast Figure; however the peak remains sharp and well contrasted at much larger sizes, with pinholes as large as 200µm providing good contrast and peak sharpness. The larger pinholes used, for example 600µm, shows that the reconstructed image is still discernible to the viewer, though in terms of contrast between the the background and the object as well as the sharpness of the reconstruction the quality is very diminished; this is an issue for implementing contrast edge-based particle detection and sizing later in the project. Using no pinhole / aperture (defined by 'OPEN') resulted in a interference pattern that failed to reconstruct; looking towards the relevant line profile, the contrast is significantly reduced compared to using any pinhole, with the broadening of the peak indicating a blurred image, making the particle indiscernible from the background.

3.4: Polarisers experiments

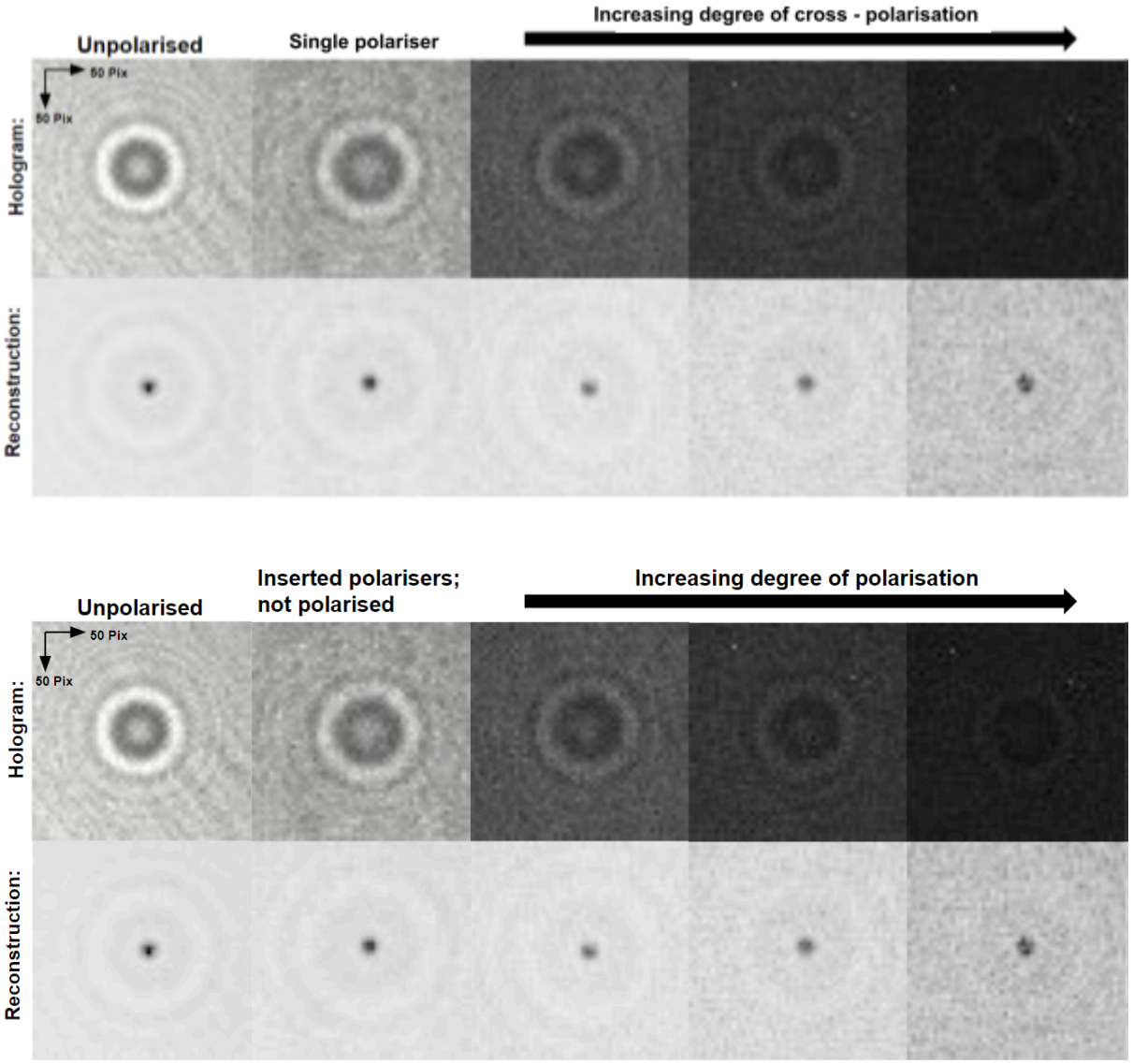

Figure 22: Experimental Image data; Polarizer Variable,Holograms & Reconstruction Images

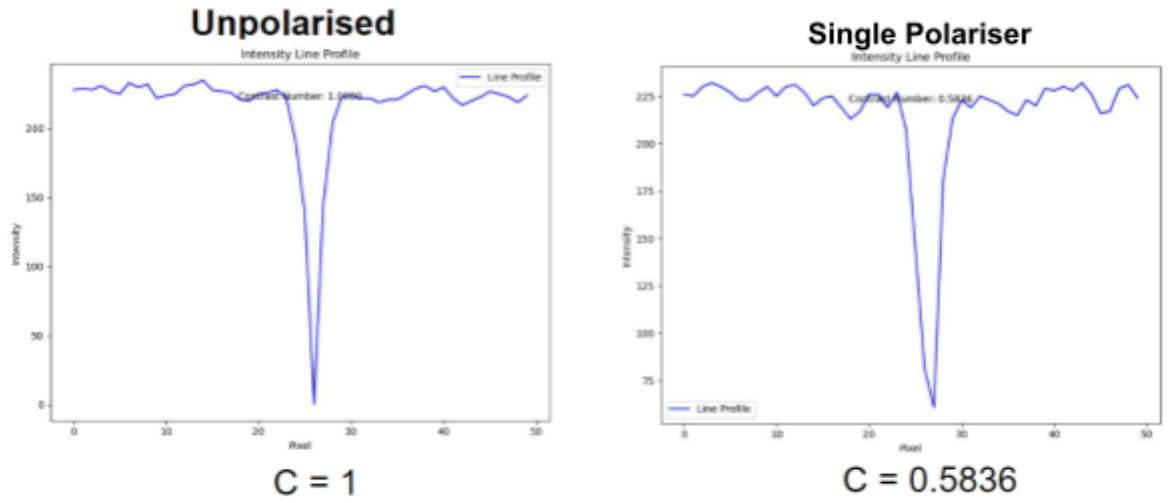

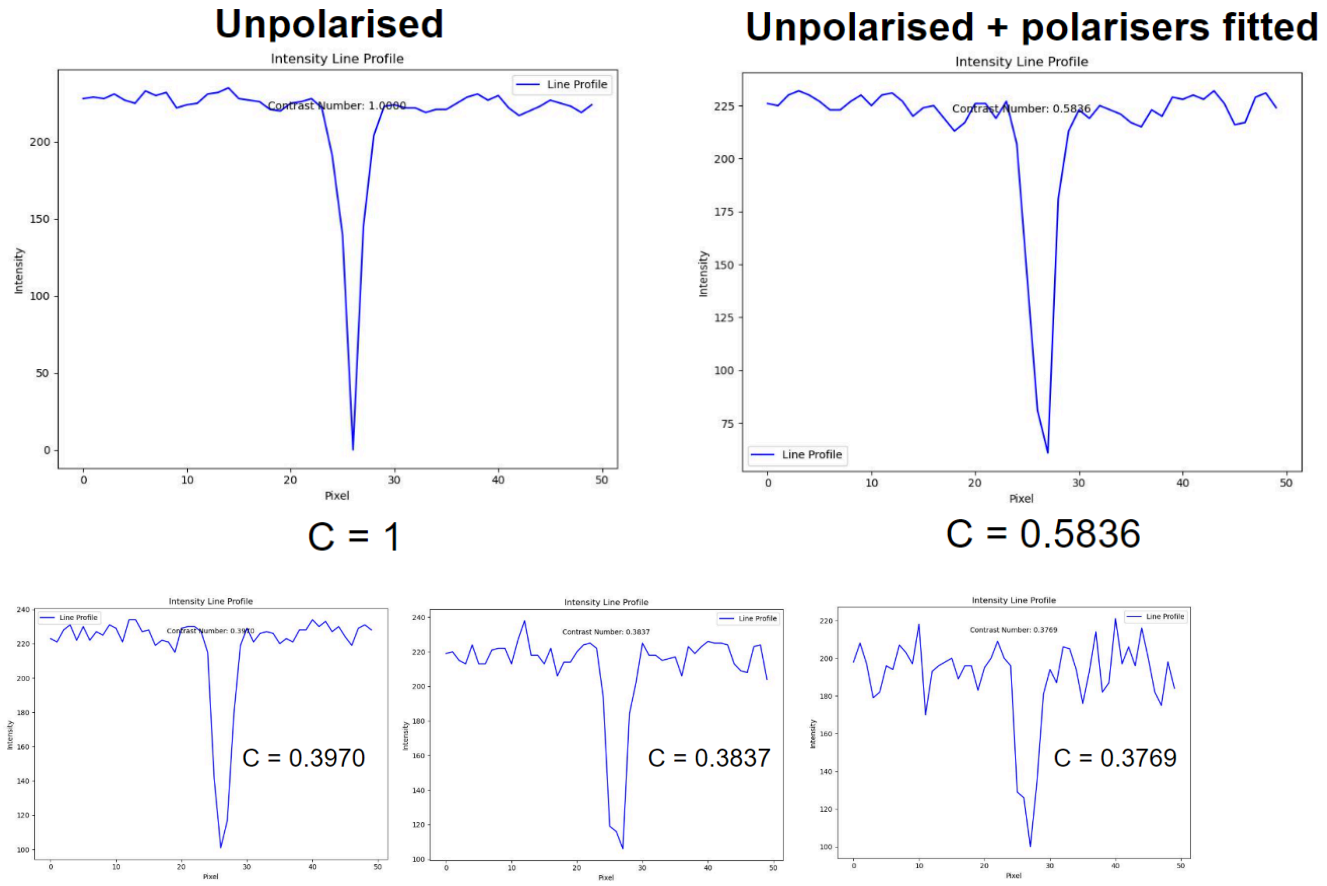

Figure 23: Experimental Image data; Polarizer Variable, line profiles

Given the potential for polarizer implementation to enhance the quality of the holograms imaged by preserving light scattered by the sample, while eliminating the reference light, discussed in section 2.4.1, an experiment was conducted to observe the effects of varying the angle between two polarisers either side of the sample. Experimentally however, the implementation of polarisers did not seem particularly useful. The inclusion of polarisers in the system had a massively negative effect on the contrast of the reconstruction, even when the polarisers used orientated in the same direction.

Increasing the degree of polarisation enhances this detrimental effect; with luminescent noise increasing (Figure 22) and while differences in contrast calculated between these levels of polarisation seem minimal, it is worth noting that the peak corresponding to the particle broadens (Figure 23). The luminescent noise in the image also increases, shown by the background level of the line profile becoming progressively more jagged, with noise peaks becoming more pronounced. However, the unresolved interference pattern in the reconstruction images, that is being attributed to the twinning effect, appears to be reduced at full polarisation - however it is unclear if the issue is fully resolved or the interference pattern is simply obscured by the increased noise. Overall, there is no benefit observed for the implementation of polarisers in this system design.

3.5: LED Driver

The decision was made to power the LED using a standard USB connection, as the device camera and LED could be powered by a single computer without need for a separate / integrated power supply or mains connection; reducing size, weight and complexity of the device.

Initially, the LED was powered simply, using the 5V supply provided via USB in conjunction with a resistor to define the LED current, as shown by Figure 24. This method was simple, cheap and quick to build; visually there seemed to be no issues with the consistency of the light intensity / brightness.USB connections supply up to 5 volt, 0.5 milliamp; making the connection appropriate to drive a single LED, e.g. 1.9V 20mA, in this manner.

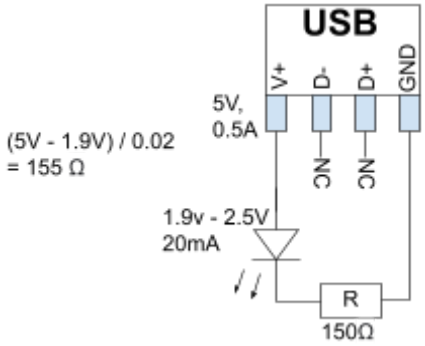

Figure 24: USB powered LED Diagram

Given a USB power supply can be inconsistent; it was decided that the power supplied to the LED from the USB had to be regulated via a driver. With the aim of constant voltage & constant current (CCCV), a driver was designed using a LM317 voltage regulator IC. The LM317 is an adjustable voltage regulator, which can also be used to supply a constant current. The LM317 generates an internal reference voltage, V_{REF}, which has a constant value of 1.25V. A resistor 'R' is then connected between the adjust ('ADJ') pin and the output, allowing the desired current & voltage to be selected and supplied, as shown in Figure 25.

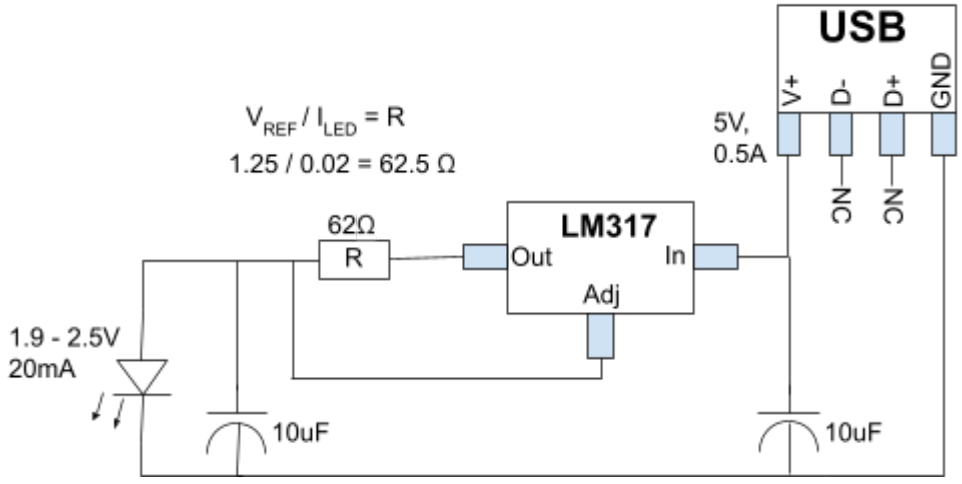

Figure 25: LM317 LED Driver diagram

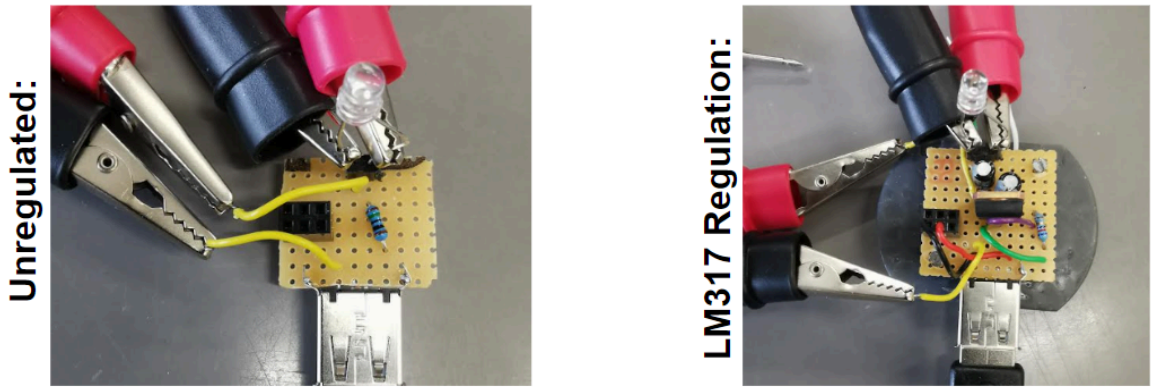

Figure 26: Unregulated / Regulated LED Testing

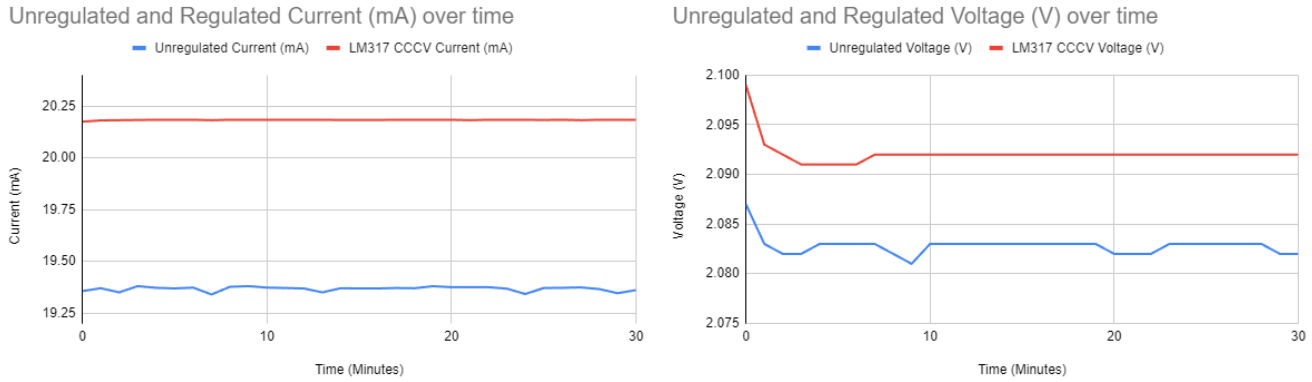

Figure 27: Unregulated Vs Regulated current & voltage graphs

As shown in Figure 27, The Current for the CCCV design was consistent, after a period of stabilising (approximately 5 minutes); the current rarely deviated, with minor fluctuation over the operating time (20.183mA ± 0.001 mA), these fluctuations were slow in nature. The unregulated design displayed rapid fluctuations, making the measurements difficult to read, with these fluctuations being approximately ± 0.03 mA.

The Voltage for the CCCV was lower than calculated; this is due to the LM317 having a 2.6V to 3V drop (due to the internal circuitry), lowering the output voltage. This reduced voltage, approximately 2.09V, is still within the operating range of the LED (1.9 - 2.5 V). The CCCV once passing a period of gradual correction (approximately 5 minutes), stabilised, any fluctuations (e.g. ±1mV) were rare and short lived (approximately lasting a second before correction). The unregulated circuit provided an output that was in constant fluctuation, making the reading difficult to read. This fluctuation was approximately ±1mV and was ever-present and rapid in nature.

3.6: Light wavelengths experiments

3.6.1: Artificial Blood Absorption

Using different wavelengths of light to exploit the difference in particle optical absorption offered another avenue for investigation. The premise being that by selectively choosing an LED with a wavelength comparable

to the absorption min/max of both particles respectively, the resultant light scattering / hologram produced would be affected, making the particles visually distinct from one another.

Using an array of diluted samples of each micro-bead, a spectrometer was used to measure the absorbance of the particle type over wavelength. Producing the graph shown in Figure 28.

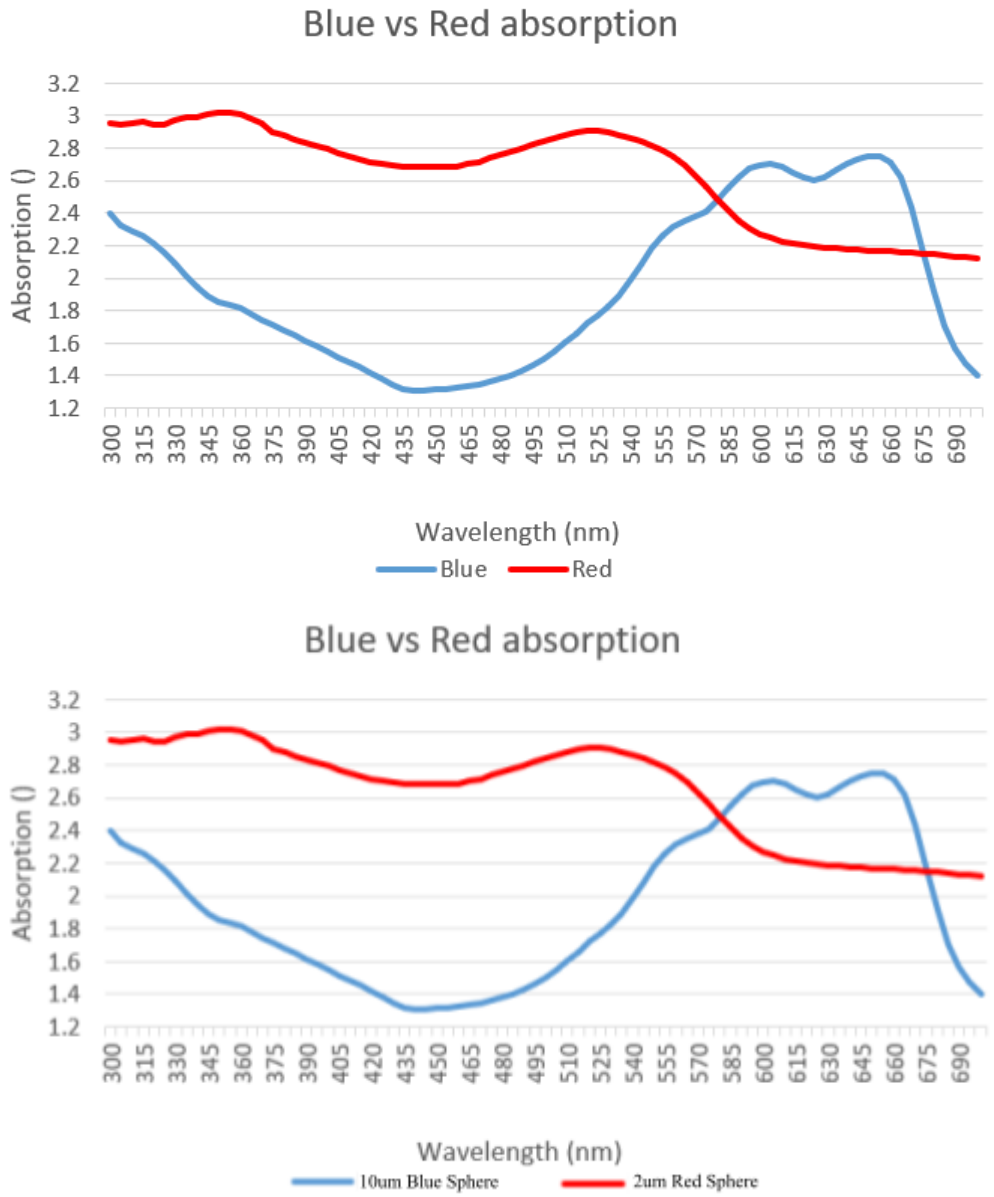

Figure 28: Artificial blood absorption measurement

This (Figure 28) highlights the opposite nature of the two coloured beads, in terms of absorption. As seen, the red particle has an increasing rate of absorption below 600nm and low absorption from 600nm onwards. The blue particle seems to be quite the opposite, with its minimum and maximum absorption mapping closely to the

maximum and minimum absorption ranges of the red particle respectively.

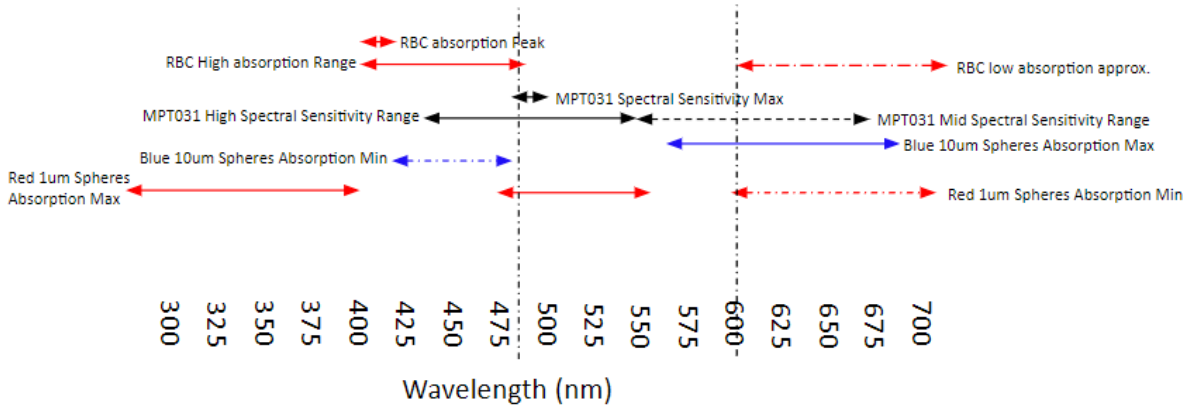

Figure 29: Compilation of absorption and spectral sensitivity sensitivity ranges

The outcomes of this experiment were compared to the RBC absorption, from literature, as well as compared against the spectral sensitivity of the camera used ,(DMM 72BUC02-ML) , as found in the suppliers technical documentation. This comparison, Figure 29, highlights how the absorption ranges for RBCs aligns with the min and max absorption of the red and blue sphere; red spheres and RBCs having similar values while blue spheres are the inverse. This allowed for two potential LED wavelengths to be identified, approximately 470 nm and 600 nm. This additionally shows that the artificial blood is a good match for a blood replacement for use in experiments with variables such as absorption wavelength / LED colour.

3.6.3 Blinking circuit integration consideration

Integrating twin red/blue flashing LEDs into the design was considered; with the premise that the complete system could utilise the separate accentuation of red or blue particles to differentiate them from each other.

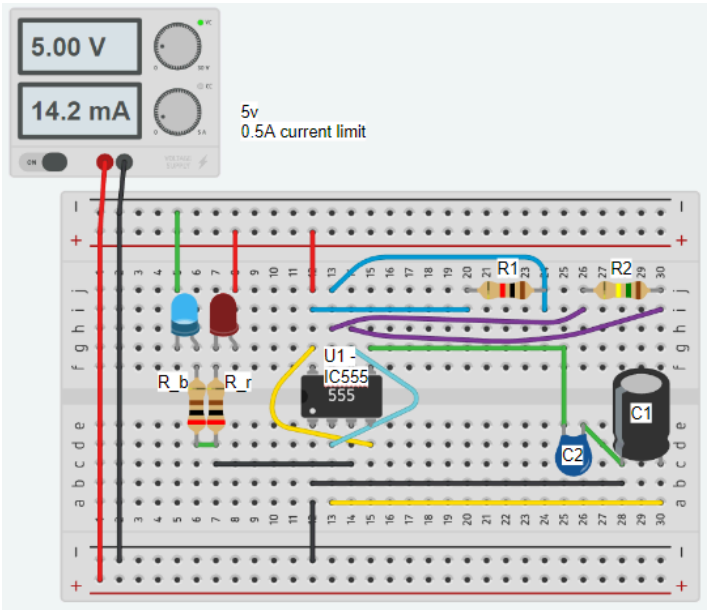

Figure 30: IC555 Based blinking circuit diagram

With research into the simplest method of achieving this effect; it was decided to utilise the readily available IC555, as shown by Figure 30. This allowed for flashing LEDs that were self triggering, with low cost, commonly used components, resulting in a low power, small circuit that could be mostly sourced internally. Low power being vital to run off a simple USB connection, while the small size of the circuit would help with easy integration into the device.

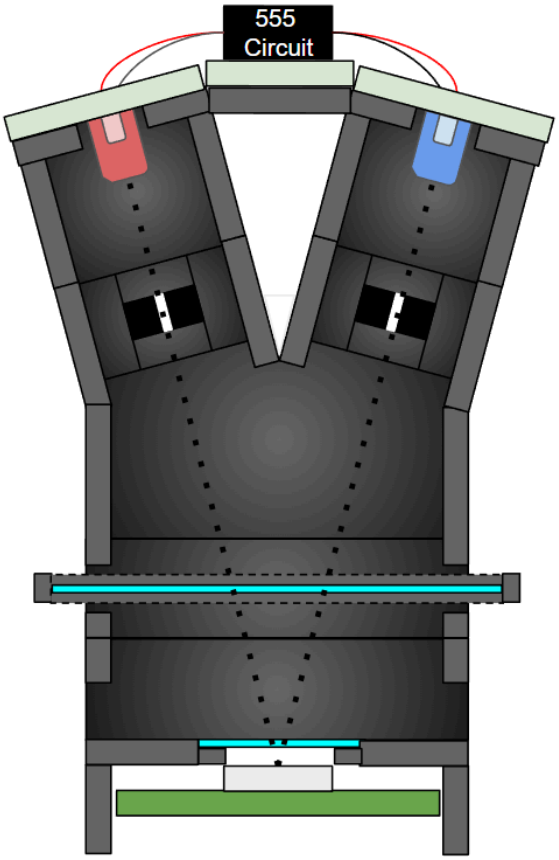

Figure 31: Blinking LED LDHM Design

This design, shown by Figure 31, resulted in a few issues. A minor issue was physically integrating two LEDs that were pinhole and sample aligned.The LED and pinholes would have to be angled due to the size of the pinhole's outer body being large, meaning if two were placed side by side, the resultant light passing through the pinhole would be out of alignment with the camera. The issue remains for having two LEDs close, as they would both be misaligned for a single pinhole..This resulted in design variations such as having a 'Y' shaped design, with the LEDs each having its own pinhole and angled so that the resulting light intercepted the sample at approximately the same point. While this was certainly an achievable design, it increased the size and bulkiness of the design, as well as increasing the cost of the design.

However the main issue was synchronicity; with the project plan including computer vision, the timing of alternating the lights would need to be synchronised with the image capture timing of the software. This is due to ensuring equal samples under each light source for a given capture rate of the batch image collection. This would prove to be a tedious task, as for the above circuit design, the LED blink timing was component based and was independent of software control; though time period can be matched by selectively choosing components or by using an alternative software timing; the synchronisation cannot be accurately matched by the user. This could be rectified by including LED control based on software via a controlling component, such as a Raspberry Pi or an Arduino microcontroller, or to base image processing on a physical reference to determine

the light source. Additionally the design would have to be amended to drive the separate LEDs in a more stable manner.

3.6.2: LED Colour

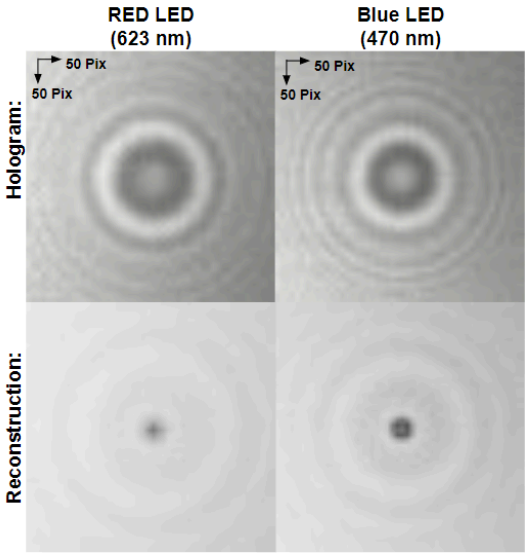

Figure 32: Red & Blue light holograms & reconstruction

Given the difficulty involved in implementing more than one LED, it was decided to focus on differentiation by particle size rather than an absorption-based method. The LED chosen was based on the theory that a smaller wavelength should grant increased resolving power.

Experimentally, a red (623 nm) & blue (470 nm) LED were used to image a 15µm white polystyrene based bead (SigmaAldrich 74964). This allowed for the resolving power based on light wavelength to be assessed with minimal impact from absorption effects. The holographic and reconstruction results are displayed by fire 32.

Visually, as seen in Figure 32, the particle viewed under blue light produces a more defined interference pattern, with the reconstruction of the particle being more pronounced than the same particle viewed under red light. This is reflected in the increased contrast for blue light as seen in the line profiles in Figure 33

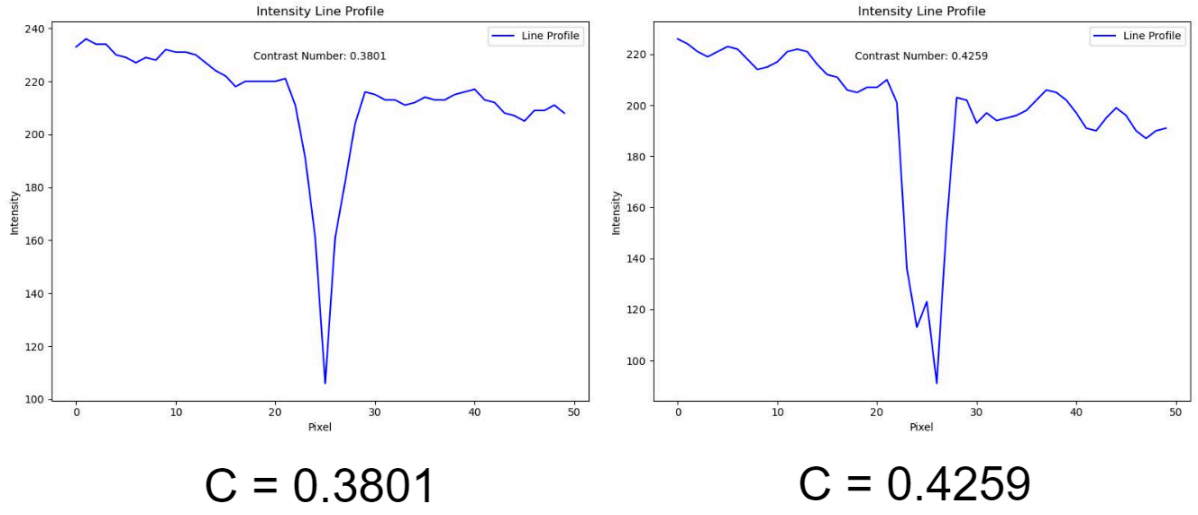

Figure 33: Red & Blue light line profile

3.8: Design Influence

The experiments in this section were conducted in order to have a practical understanding of the theory behind LDHM systems; the resultant data can therefore be used to influence the design of bespoke LDHM device, as well as optimise the design for appropriate use for the context of the project.

The geometry of the device, namely the Z1 & Z2 parameters, had a large impact on the quality of the image quality, both in terms of contrast and sharpness but also in terms of FOV for Z2. If the sample is placed directly on the sensor, only separated by the glass thickness of the slide / microfluidic, the Z2 parameter can be on the micron-scale, with the microfluidic device discussed further on in section 5 (Microfluidics) having a glass thickness of approximately 130 - 160µm , with a channel thickness of approximately 100µm. This provides a Z2 between 130-260um, however, if the 3D printed camera guard (designed for component protection) is used, Z2 is increased by 1mm. With parameter Z2 being smaller, the size is negligible in regards to the total size of the device, the FOV is approximately unit to the sensor size (or the size of captured image if resolution is not maximum when defined in code or photo application) and the image quality is increased. This allows the majority of the length of the device to be defined by the parameter Z1. which increases image quality with distance, though it is important to consider the compactness of the device for larger distances, with the goal of the final device being handheld, the length of 6cm was chosen for Z1.

The pinhole chosen was 15µm, as this provided the reconstruction with the highest quality; while larger size pinholes could be used with a relatively good resultant image quality, there are little benefits to do so. The potential for pinhole blocking due to FOD is increased with smaller pinholes, however in devices with a sealed casing, built in a clean environment, this issue should be unlikely. The main issue with the pinhole being smaller is that slight variations in alignment during the construction stage or LED position increased the effects of any misalignment, i.e. the sensor is not illuminated centrally.
Despite every effort made to make the final design robust to misalignment; the implementation of a fine-tune system for pinhole position was useful to ensure optimal alignment. A simple method was to introduce deep seated aligning screws (e.g. M.2 screws) coupled with springs to allow for X,Y movement of the pinhole / LED by carefully rotating the screws, as shown by Figure 34. This was completed just after the construction stage of device set-up and then locked in place using epoxy to avoid misalignment. This design feature does slightly increase the complexity of the device, however it is a feature that the average user would not need to interact with, mainly existing for device initial set-up. Furthermore the effect of the size and weight on the device is negligible.

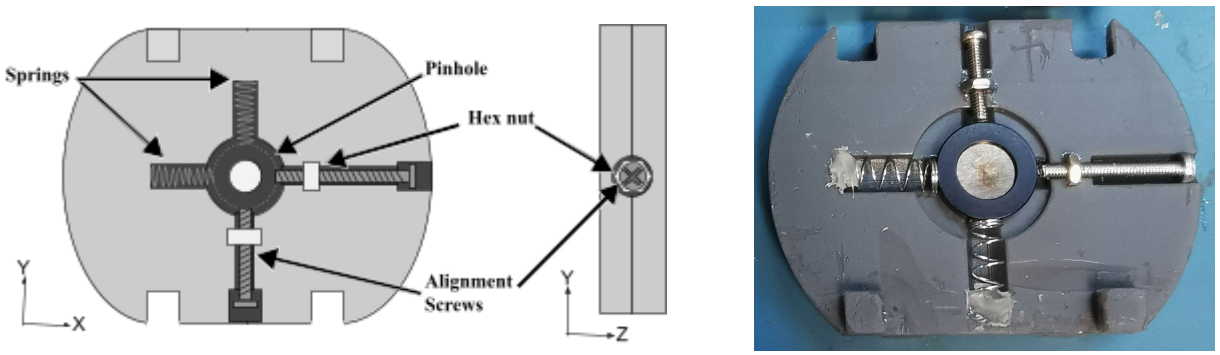

Figure 34: XY Alignment mechanism

The polarizer inclusion seemed particularly useful in allowing a user to manually adjust light levels, to avoid dead zones in the image from high intensity input light. A user operated component however introduces potential human error, and if used incorrectly, the level of polarisation can change within the same imaging session. For this to be included, and be appropriately designed for an untrained user to operate, the polariser would need to be internally seated, aligned against a reference / metric / specification, after construction by a

trained individual, then locked using a method such as RTV / epoxy to avoid alteration. Ultimately, the inclusion of polarisers offered no benefits, with a detrimental effect on image quality in terms of luminescent noise and reduction of contrast, resulting in polarisers not being implemented into the final design.

With its synchronicity issues, alongside the altered physical design, integrating flashing twin LEDs seemed to be vastly overcomplicating the design and increasing the unit cost for very little benefit, especially considering the reduction in resolving power when switching between LED wavelengths. Additionally to fully take advantage of any absorption effects, the WBCs would have to be dyed blue, which defeats the LDHM benefit of label-free imaging. Ultimately twin-LED designs were abandoned in favour of single blue LED designs, which offered more simplistic LED driving, increased resolving power and image quality.

When weighing the advantages and disadvantages of CCD vs CMOS, it was decided to utilise CMOS technology over CCD, due to the ability to power the CMOS devices via simple connections such as USB. The CMOS camera ,the DMM 72BUC02-ML, was chosen to allow for its low power consumption, allowing the camera to be powered and transfer data to a computer directly via a standard USB connection. The camera utilises a MT9P031 sensor, allowing for high resolution images (2592 x 1944 pix [5MP]), a large sensing area (1/2.5 inch format) and a high quantum efficiency (QE) range (approximately 450-550 nm) that matches the LED .

The ‘Artificial Blood’ used to validate the device was changed, focusing on sizing differentiation rather than absorption. This resulted in the change to multiple sized beads (45µm, 15µm & 10 µm) rather than the 2µm Red and 10µm blue previously used. 2µm beads proved difficult to image, with their interference pattern being weak, making them difficult to capture. The change still provides comparable sizes to WBCs and RBCs for 15µm and 10µm respectively, 45µm beads being much larger was easier to differentiate visually, giving the user confidence that the sample was well mixed as well as a reference for software sizing.

An issue with the open-design is the effects of changes in ambient light levels, which resulted in most experiments being conducted in a dark environment. These working conditions were less than ideal; making it necessary to shield the components from outside light influence. To resolve this issue, a 3D printed casing was designed to hold the components in place, as well as shield them from outside light.

Final Specification:

Parameter	Specification	Cost	Note(s)
Z1	6cm	-	Compromise between image quality and device compactness
Z2	130µm - 260µm 1.13mm - 1.26mm (camera guard)	-	Coverslip thickness & channel thickness / With camera guard
Pinhole	15µm	£69.42	Fine-tune system implemented, potentially use up to 200 µm
Polariser	n/a	n/a	Not implemented in final design
LED	470 nm Wavelength, 15 nm Bandwidth	£0.22 (LED (+≈£5) LM317 Driver	Blue LED LM317 Driver

Camera	DMM 72BUC02-ML	£101.37	Micro-USB Powered, high resolution, QE matches light source
Reconstruction Method	Angular Spectrum		
	-	£176.01	-

Table 2: Final Prototype Specification

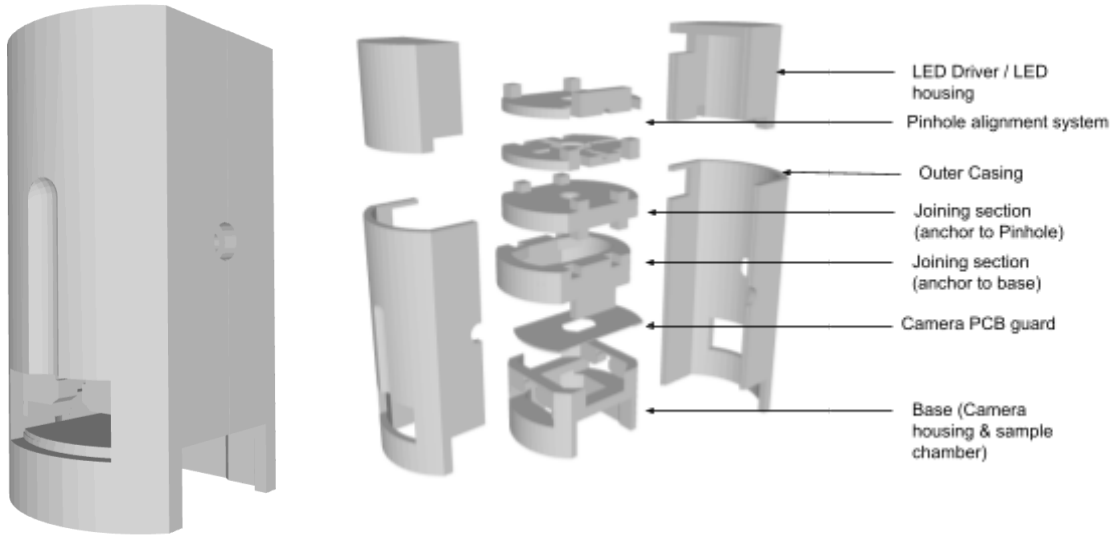

Figure 35: 3D model of final Design (whole & 'exploded' models)

4: Microfluidics:

4.1: Overview

Throughout the various design iterations explored in the project, the method of sample use was also subject to change.

Perhaps the most instinctual method for microscopic sample preparation is the use of smear style slides; this method allows for easy sample collection and use, low cost and likely to be well known to most people. The issue with this method is that smear samples from a raw source, such as from a finger prick, are quite particle dense and not necessarily uniform in the particle distribution. This, for a LDHM application, has issues such as complex overlapping of particle holograms, which would require a reconstruction method to generate meaningful results from, with potential for closely situated particles to be indistinguishable. This issue only becomes more severe at higher particle concentrations, making a low concentration sample desirable. However, with lower concentrations, any error in the measurement accounts for a larger value of the overall result.A smear approach would also only allow for a single image data set to be collected, as to collect more from a single slide would require moving camera / light components or a shifting sample mechanism; which increases complexity and would also shift the view of static contamination particles, meaning they could not be subtracted, which would affect the error rate.

The addition of microfluidics into the design has many benefits. With particles having a tendency to clump together in higher concentrations; a solution to this is to introduce low concentration microfluidic flow, so that the flow can be sampled over time and averaged to reduce the impact of any errors, including clumping and a non-uniform sample mix. Other benefits include the sample being the only moving component images; allowing for image subtraction with an image background to remove contaminants on the polarizers, camera or sample slides that would otherwise be counted and introduce error. This requires more design work to implement and is slightly more complicated to use compared to a static slide; however in the recent years, i.e the COVID-19 pandemic, microfluidic diagnostic technologies have been widely distributed and used by the public. This provides evidence that microfluidic based solutions can be appropriately and effectively utilised by untrained individuals on a national and international scale and relieve pressure felt by healthcare services by utilising decentralised diagnostics.

4.2: Smear Sample:

Smear samples were easily produced by using a pipette to place a small amount of sample onto a cleaned slide, and placing a coverslip on top to naturally allow the sample ot evenly distribute the sample; these would be left to dry in order to produce a sample that is static and has no risk of leaking.

Smear samples proved to be the easiest sample to work with for preliminary testing, the static samples allowing for testing to reference the same particle as variables were altered with no risk of samples leaking, which would result in contamination of the set-up and potentially damaging electronic elements such as the camera. This further allowed for experimental images to be captured and analysed with software such as ImageJ.

However, this method had some disadvantages. Smears did not always result in uniform sample distribution, sometimes drying in a way that resulted in densely populated rings due to the coffee-ring effect. This made holographic images unclear , due to the overlapping interference patterns, as well as resulting in reconstructed images where separate particles were hard to distinguish. Contour / edge detection software also failed to discern particles with these issues. With a single experimental image being taken for a sample, software also was

sensitive to FOD on the slide glass or camera sensor surface, resulting in obscuring particles unless all components were cleaned to a high standard regularly.

Due to these issues, it was decided to move to a microfluidic approach; this would allow images to be taken before and after sample loading, which would aid in background / contamination subtraction as well as offering other benefits such as a higher throughput and more rapid testing (such as varying sample concentrations).

4.3: Microfluidic Channel

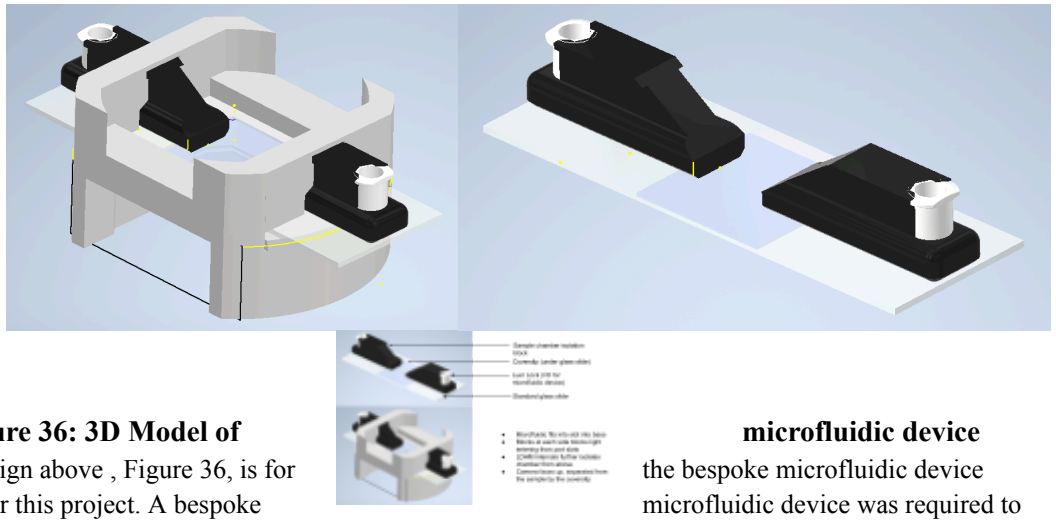

Figure 36: 3D Model of microfluidic device

The 3D design above , Figure 36, is for the bespoke microfluidic device designed for this project. A bespoke microfluidic device was required to satisfy four criteria to be considered compatible with the LDHM system design; transparency, leak proof, low thickness and durability.

The base of the microfluidic is made from a standard microscope slide; due to the material being transparent and durable, with the slides themselves being readily available and having a standard size. Being glass, materials such as the slide and coverslip could be inspected using the LDHM device before construction to ensure that the surfaces were free of contamination, resulting in channels that contained no image-obstructing FOD. These slides could be drilled into, creating an inlet / outlet through the slide. Using microfluidic tape, a channel could be created on one side of the slide, with a thin coverslip capping the channel. The coverslip would be placed directly against the imaging sensor, resulting in a Z2 parameter that is 130µm - 260µm thick. In order to move samples in and out of these ports, a luer lock block was designed; these parts could easily be 3D printed, and attached to the drilled inlet / outlet. Designing the luer lock block allowed for the ports to be compatible with syringes or microfluidic tubing. While the designs could of been designed to simply sit on top of the ports, it was decided to create a thick block either end, allowing for the microfluidic device to slide into the base of the LDHM device with ease, while naturally covering the access port to avoid introducing ambient light into the imaging chamber. To ensure the device was leak proof, clear epoxy was applied at the boundaries between the luer lock blocks and the slide, as well as boundaries between the slide and the coverslip; this attributed no extra thickness to the to the device in terms of Z2 or inhibited the insertion of the device while ensuring no sample breached the channels. Microfluidic devices made could be tested before use, using deionised water to validate the sealed channel before using potentially hazardous samples.

The move to microfluidic devices allowed for the software to be further developed, with advancement being made for particle detection, contamination subtraction, and automated bulk sample analysis.

4.3.1: Construction of Microfluidic Channel

For the microfluidic to be successful in its purpose, the method of construction is very particular:

1. Gather components
    a. Standard glass slide
    b. 3D printed Luer ports
    c. Glass coverslip (22mm x 55mm recommended)
    d. Microfluidic tape
    e. Epoxy (optional)
2. Gather tools
    a. Scalpel
    b. Cutting mat / board
    c. Diamond coated drill bit
    d. Compatible dremel / pillar drill
    e. Epoxy applicator (optional)
    f. Epoxy mix palette (optional)
    g. Syringe
    h. Microfluidic tubing (Optional)
3. Drill I/O holes through the glass slide:
    a. Measure and mark appropriate positions for the I/O port holes. The holes should be equidistant to the centre and spaced so that the holes can be covered by the glass coverslip used, while leaving a perimeter along the edge of the cover slip for microfluidic tape.
    b. Using a diamond coated drill bit, use a pillar drill or dremel to carefully drill two holes in the glass slide,using water to remove debris. These holes can be anysize as long as it is compatible with the 3D printed I/O Ports - in this case 1mm holes were used.
4. Clean components
    a. The glass components (slide, coverslip) have to be thoroughly cleaned to remove unwanted FOD.
5. Create a channel on the glass slide
    a. Using a Scalpel, cut a section of microfluidic tape the size of the coverslip, keeping the film layer on each side of the tape intact.
    b. Place the tape section on the glass slide and mark the position of the I/O port holes
    c. Using a Scalpel, cut a channel between the two points to form a channel. The perimeter of the channel should be one section with no cuts or creases.
    d. Peel one side of the film and place the tape on the glass slide, ensuring that the I/O ports are either side within the channel.
6. Seal the channel
    a. Place the coverslip over the channel, making sure the entire surface of the slide and coverslip are in contact with the tape.
7. Add 3D printed ports
    a. Using a Scalpel, cut two sections of microfluidic tape the size of the port sections, keeping the film layer on each side of the tape intact.
    b. Using a Scalpel, cut a channel in the tape to allow flow between the 3D printed port and the glass porthole. The perimeter of the channel should be one section with no cuts or creases.

c. Peel one side of the film and place the tape on the glass slide, ensuring that the I/O ports are not obstructed, and press the 3D printed sections firmly on top of each side.

8. Epoxy boundaries (optional)
    a. To further leakproof the design, epoxy can be applied to the 3D printed port - slide boundary as well as the slide-coverslip boundary
9. Leak test
    a. Method 1:
        i. To leak-test the microfluidic, you can place your thumb over one port, and use a syringe to pull the air out of the other.
        ii. Wait a few moments
        iii. Remove thumb from port
        iv. If pressure was maintained (i.e. channel sealed) then suction should be experienced when removing the thumb. If pressure was lost, there may be a leak in the system.
    b. Method 2:
        i. Connect microfluidic tubing to the ports
        ii. Using a syringe, pump deionised water into the microfluidic
        iii. Any leaks in the system should become evident.

5: Software:

5.1: Purpose:

Digital Holographic Microscopy can be used for viewing samples in a comparable way to that of a traditional optical microscope, with the exception of a reconstruction stage to view the sample as a real image. The purpose of the software coupled with the physical device is to handle this reconstruction stage, as well as allow for Computer Vision implementation for the purposes of particle detection, sizing and categorisation.

5.1.1: Python

There are many capable programming languages and softwares available for the uses of image capture, processing and analysis - Java, C, MATLAB and ImageJ to name a few. This project focused on developing supporting software in the programming language 'Python'.

Python allows for rapid prototyping, as the syntax of the language is relatively simple, making it easy to learn, read, and overall more flexible in its use when compared to other languages (e.g. flexible variable data type). Python has a large library ecosystem, with libraries specifically tailored around computer vision (OpenCV), image processing (PIL), multidimensional array support (NumPy) and scientific computing support (SciPy). These libraries have extensive community support, with documentation, FAQs and troubleshooting advice readily available.

Developing in python introduces a degree of future proofing into the project. Python code can be integrated with other programming languages, like Java or C, meaning the software can evolve over time by being implemented into applications that utilise these languages. As such, Python code can be executed with little issue on most standard operating systems, such as Windows, MacOs & Linux, further allowing python code to run on any device that operates based on these operating systems.

5.2: Camera utilisation

5.2.1: Live video feed

A major advantage of using a digital sensor for capturing of image data is the possibility to view the sample in real time. By utilising a live video feed, the user can view the sample as it traverses the microfluidic channel, as well as be aware of issues such as micro/macro leaks or microfluidic contamination. The subtraction method, discussed later in this section, relies on the user generating a background and subject image while aided by the instructions provided by console postings and the live video feed.

```
# Video Capture Code
deviceCamera = cv2.VideoCapture(0, cv2.CAP_DSHOW)  # '0' indicates default camera, '1' secondary (LDHM Device)
deviceCamera.set(cv2.CAP_PROP_FRAME_WIDTH, 2592)  # Resolution X
deviceCamera.set(cv2.CAP_PROP_FRAME_HEIGHT, 1944)  # Resolution Y
```

Figure 37: Code; camera initialization

```
# Get the camera's resolution
width = int(deviceCamera.get(cv2.CAP_PROP_FRAME_WIDTH))
height = int(deviceCamera.get(cv2.CAP_PROP_FRAME_HEIGHT))
imageXY = 640  # Change this to your desired size

# Calculate the crop coordinates to get a 640x640 square in the center
crop_x = (width - imageXY) // 2
crop_y = (height - imageXY) // 2
```

Figure 38: Code; camera initialisation & crop

The initialisation of the video capture object is displayed by Figure 37; “deviceCamera” is captured using the openCV function cv2.Videocapture(integer, cv2.CAP_DSHOW), where the integer represents the camera utilised by the code , ‘0’ being device built in camera (e.g. webcam), and ‘1’ onwards being secondary cameras . The integer used depends on the number of cameras available to the device the code is running on. The second and third lines set the video capture to the maximum resolution supported by the camera used, in this case the max resolution being 2592x1944 pixels.
The width and height of the camera resolution is then stored in variables for use in cropping the video feed. The image processing requires the images to be square, meaning the video feed and the images captured must also be squared. To do this, a parameter imageXY, is set to define the pixel height & width of the videofeed. The imageXY should be no more than the native camera resolution height. Given approximately unit magnification - the FOV of the device is defined as the square of imageXY multiplied by the physical sensor size, in this case 2.2 microns. The video feed is cropped to maintain a central view from the camera, for example 640x640.

```
    success, frame = deviceCamera.read()
    # Crop the frame to 640x640 centered
    cropped_frame = frame[crop_y:crop_y + imageXY, crop_x:crop_x + imageXY]

    # Resize the cropped frame to imageXY before saving
    cropped_frame = cv2.resize(cropped_frame, (imageXY, imageXY))

    cv2.imshow("Live LDHM Video", cropped_frame)
```

Figure 39: Code; live video feed

In Figure 39, using deviceCamera.read(), a frame is captured from the selected camera and temporarily stored in parameter ‘frame’. This captured frame is then cropped to the imageXY size, while maintaining the centrality of the frame. Finally, this cropped video feed is displayed for the viewer to observe the sample and take background / subject images.

5.2.2: Image Collection

The live video aids in the collection of images for analysis. Image collection is handled by the user, allowing the user to select a specific folder to save image data as well as capture the necessary background image and desired sample photo.

```
pathPass = 0
while pathPass == 0:
    instructionSet(0)
    file_path = input("Enter the file path of your folder: ")  # input path
    titleBanner("File path is reachable", True)
    if os.path.exists(file_path):  # Test if path is real
        pathPass = 1
    else:
        titleBanner("ERROR: File path is unreachable", True)
```

Figure 40: Code; Folder Selection

In Figure 40, the user is prompted to provide a file path as a location to store image data from the software. The file path is checked, using the method“os.path.exists(file_path)”, to ensure correct saving of image data.

```
    if cv2.waitKey(1) & 0xFF == ord('b'):  # button press for background image capture
        if backgroundTaken == 0:
            cv2.imwrite(os.path.join(file_path, 'LDHM_Raw' + "_Background" + '.tiff'), cropped_frame)
            background_image_path = os.path.join(file_path, 'LDHM_Raw' + "_Background" + '.tiff')
            backgroundTaken = 1
            titleBanner("Background Image Taken", True)
            instructionSet(2)

    if cv2.waitKey(1) & 0xFF == ord('s'):  # button press for subject image capture
        if subjectTaken == 0:
            cv2.imwrite(os.path.join(file_path, 'LDHM_Raw' + "_Subject" + '.tiff'), cropped_frame)
            subject_image_path = os.path.join(file_path, 'LDHM_Raw' + "_Subject" + '.tiff')
            subjectTaken = 1
            titleBanner("Subject Image Taken", True)
```

Figure 41: Code; Background & Subject image capture

The if statements above, Figure 41, are embedded in a while function that checks if parameters “backgroundTaken” & “subjectTaken” are both not equal to ‘1’. Using key presses, the background and subject images are taken from the live video feed at the moment of button press.

5.3: Particle detection

5.3.1: Image subtraction & denoising

```python
def subtractionDespeckle(background_path, subject_path):
    # Read the background and subject images
    background = cv2.imread(background_path, cv2.IMREAD_GRAYSCALE)
    subject = cv2.imread(subject_path, cv2.IMREAD_GRAYSCALE)

    if background is None:
        print(f"Error: Could not read the background image at '{background_path}'")
        return

    if subject is None:
        print(f"Error: Could not read the subject image at '{subject_path}'")
        return

    # Convert the images to NumPy arrays
    background_array = np.array(background)
    subject_array = np.array(subject)

    # Subtract the subject image from the background to get the original image
    original_image = background_array - subject_array

    # Invert the image for erosion and dilation
    inverted_image = cv2.bitwise_not(original_image)
    # Perform erosion and dilation to remove small speckles
    kernel1_1 = np.ones((1, 1), np.uint8)
    kernel3_3 = np.ones((3, 3), np.uint8)
    inverted_eroded = cv2.erode(inverted_image, kernel3_3, iterations=2)
    inverted_dilated = cv2.dilate(inverted_eroded, kernel3_3, iterations=2)

    # Apply Gaussian blur to the inverted dilated image
    blurred_image = cv2.GaussianBlur(inverted_dilated, (9, 9), 0)

    # Invert back the blurred image
    dilated = cv2.bitwise_not(blurred_image)

    #Contour Fill
    lower = 0
    upper = 100
    thresh = cv2.inRange(dilated, lower, upper)
    threshinvert = 255 - thresh

    des = cv2.bitwise_not(threshinvert)  # threshinvert
    contour, hier = cv2.findContours(des, cv2.RETR_CCOMP, cv2.CHAIN_APPROX_SIMPLE)

    for cnt in contour:
        cv2.drawContours(des, [cnt], 0, 255, -1)

    invertedfill = cv2.bitwise_not(des)
    cv2.imshow("Contour Fill",invertedfill)
    # Save the image subtraction as "temp_subtraction.tiff"
    #cv2.imwrite("temp_subtraction.tiff", original_image)
    Reinvertedfill = 255 - invertedfill
    Output_eroded = cv2.erode(Reinvertedfill, kernel3_3, iterations=1)
    inverted_dilated = cv2.dilate(Output_eroded, kernel3_3, iterations=1)
    cv2.imshow("Contour Fill_ Eroded/Dilated", inverted_dilated)
    FinalOutput = 255 - inverted_dilated
    # Display the images side by side
    stacked_images = np.hstack((background, subject, original_image, FinalOutput))
    #stacked_images = np.hstack((subject, original_image, FinalOutput)) #alt
    cv2.imshow("Background - Subject - Subtraction - Output", stacked_images)
    #cv2.imshow("Output", dilated)
    # Wait for a key press and then close the windows
    cv2.waitKey(0)
    cv2.destroyAllWindows()

    # Return the blurred image
    return FinalOutput
```

Figure 42: Code; subtractionDespeckle Function

The background and subject images captured are not perfect; with noise captured in the image as well as physically captured contamination on the microfluidic device / camera. The aim of image subtraction and denoising is to remove contaminant particles from the experimental images, as well as remove artefacts caused by noise. The reduction of this noise and contamination artefacts allows for more accurate particle detection, aiding in producing more reliable further analysis.

Function “subtractionDespeckle(background_path, subject_path)”, shown by Figure 42, is designed to resolve the contamination / noise issues. The inputs of this function are the captured images for background captured during the image collection stage by the user. These images are read as grayscale images, using “cv2.imread” with the “cv2.IMREAD_GRAYSCALE” flag. These images are converted into NumPy arrays to allow easy manipulation of the image data, such as subtraction. The subject array is subtracted from the background array; this allows the differences between the two images (e.g. particles) to be highlighted, while shared details (e.g. static contamination) is ignored. The image produced is then inverted to allow erosion / dilation operations to be performed on the image effectively.
Two iterations of the erosion and dilation operations are then carried out on the image, utilising a 3x3 kernel. Using a gaussian blur filter smooths the final result of these operations. The image is then re-inverted back to its original form. A black/white threshold is applied to the image, which is then inverted to allow for contour filling; this allows the particles detected to be drawn as solid, aiding in finding their centres as well as giving the particles a more solid / dense appearance. The image is then inverted to allow for a further reduction of artefacts that may have increased due to the contour filling, as well as better defining particles that are close together. The output is then re-inverted, to produce a final, refined image, called “FinalOutput”. These images can be displayed as a stacked image set, with the function returning the “FinalOutput” image.

Parameters used, such as kernel size and number of iterations are dependent on the level of noise / size of artefacts in the subtraction images, with larger kernels being more aggressive in the relevant operation, and smaller kernels carrying out the function with a lighter touch. Therefore these parameters will need to be altered for different LDHM device designs.

5.3.2: Particles, Fragments and Obstructions

```python
def find_centers(image, min_contour_area=150, max_contour_area=500):
    # Find contours in the binary image
    contours, _ = cv2.findContours(image, cv2.RETR_EXTERNAL, cv2.CHAIN_APPROX_SIMPLE)

    BGRimage = cv2.cvtColor(image, cv2.COLOR_GRAY2BGR)
    particles_centers = []  # List to store particle centers
    particles_tags = []  # List to store particle tags
    fragments = 0
    particles = 0
    obstructions = 0

    for idx, contour in enumerate(contours):
        # Calculate the center of each contour if the contour area is greater than zero
        M = cv2.moments(contour)
        if M["m00"] > 0:
            center_x = int(M["m10"] / M["m00"])
            center_y = int(M["m01"] / M["m00"])
        else:
            center_x, center_y = 0, 0

        contour_area = cv2.contourArea(contour)

        # Draw a small circle at the center of the contour and add a tag
        tag = ""
        color = None
    if contour_area >= min_contour_area and contour_area < max_contour_area:
        color = (0, 0, 255)  # Red color for particles
        cv2.circle(BGRimage, (center_x, center_y), 5, color, -1)
        particles += 1
        tag = f'P{particles}'
    elif contour_area >= max_contour_area:
        color = (255, 0, 0)  # Blue color for obstructions
        cv2.circle(BGRimage, (center_x, center_y), 5, color, -1)
        obstructions += 1
        tag = f'O{obstructions}'
    else:
        color = (0, 255, 0)  # Green color for fragments
        cv2.circle(BGRimage, (center_x, center_y), 1, color, -1)
        fragments += 1
        tag = f'F{fragments}'

    # Get the dot color and use it for the tag text
    dot_color = tuple(color)
    cv2.putText(BGRimage, tag, (center_x + 10, center_y + 10), cv2.FONT_HERSHEY_SIMPLEX, 0.5, dot_color, 1)

    # Store particle centers and tags separately in their respective lists
    if contour_area >= min_contour_area and contour_area < max_contour_area:
        particles_centers.append((center_x, center_y))
        particles_tags.append(tag)
return particles_centers, particles_tags, BGRimage, fragments, particles, obstructions
```

Figure 43: Code; find_centres Function

The “subtractionDespeckle” method is quite effective at extracting the particles. However these particles still need to be identified, as well as differentiated from fragments (i.e leftover noise / artefacts) and obstructing objects (e.g. air bubbles). Using the a binary input image, the function “find_centres” , Figure 43,identifies contours in the image, categorises the particles based on contour area, calculates their centre of mass, and assigns a descriptive tag ("P" for particles, "O" for obstructions, and "F" for fragments) along with a number to each object and displays it near the centre.

Using the function “cv2.findContours”, the contours in the binary image are identified. The counters for each category are initialised, with the counts starting at ‘0’. For each contour found, the centre of mass of the contour is calculated using “cv2.moments(contour)” and checks if the size is greater than ‘0’, and generates coordinates

for the centre. Based on the area size, found by “cv2.contourArea”, the contours are categorised as fragments, particles or obstructions and assigns the relevant tag and number for each. This information is sorted in the lists “particle_centres” and “particle_tags”. This function returns these lists, as well as the fragments, particles and obstructions count.

5.4: Reconstruction Image Processing

While the particle positions can be identified, the size of the particles cannot, as the raw images produced by the LDHM device are of the particle holograms. Therefore a reconstruction method must be used to reconstruct the images to more comprehensible images. The “angularSpectrum” function here is taken from PyDHM, an open source library produced by Castañeda R, Trujillo C, Doblas A (2022) [58], for DHM applications.

```
def angularSpectrum(field, z, wavelength, dx, dy):
    '''
    Function to diffract a complex field using the angular spectrum approximation
    Inputs:
    field - complex field
    z - propagation distance
    wavelength - wavelength
    dx,dy - sampling pitches
    '''

    field = np.array(field)
    M, N = field.shape
    x = np.arange(0, N, 1)
    y = np.arange(0, M, 1)
    X, Y = np.meshgrid(x - (N / 2), y - (M / 2), indexing='xy')

    dfx = 1 / (dx * M)
    dfy = 1 / (dy * N)

    field_spec = np.fft.fftshift(np.fft.fft2(np.fft.fftshift(field)))
    phase = np.exp(
        1j * z * 2 * math.pi * np.sqrt(np.power(1 / wavelength, 2) - (np.power(X * dfx, 2) + np.power(Y * dfy, 2))))

    tmp = field_spec * phase

    out = np.fft.ifftshift(np.fft.ifft2(np.fft.ifftshift(tmp)))

    return out
```

Figure 44: Code; PyDHM based Angular Spectrum Reconstruction

The “angularSpectrum” function (Figure 44) requires five inputs; “field” (hologram image), “z” (propagation distance), “Wavelength”, “dx” (sampling pitch x), “dy” (sampling pitch y). The field is converted into an array using NumPy. The function generates a grid, representing pixel positions in the field. The coordinates are adjusted to be centred at “(0,0)” to be appropriately formatted for fourier transforms. Based on the sampling pitches provided, spatial frequencies (“dfx”,”dfy”) are calculated. Using a 2D fourier transform (“np.fft.fft2”) on the field array, the domain is transformed from the spatial domain to the frequency domain.
Using the given wavelength and propagation distance and calculated spatial frequencies, the phase information is calculated, which simulates the phase shift caused due to propagation over the distance. The field (frequency domain) is then multiplied by the phase information, after which an inverse fourier transform can be applied to obtain the field at propagation distance ‘z’.

5.5: Particle Sizing via line profiling

With the particles detected, central coordinates found and holograms reconstructed, the next step is to size the particles in order to categorise them. Given the image is of a known physical size, using the pixel length of a reconstructed particle (multiplied by the physical pixel sensor size in microns) should yield the particle size in microns. The pixel length of the particle can be calculated using a line profile across the particle and its background and use an appropriate line profile threshold to differentiate between the particle and background.

5.5.1: Line profile Extraction

```
def extract_horizontal_line_profile(image, center_x, center_y, line_length):
    h, w = image.shape[:2]
    if center_y >= h or center_x >= w:
        return None
    start_x = max(center_x - line_length // 2, 0)
    end_x = min(center_x + line_length // 2, w - 1)

    # Change the line length here to take profiles 2 pixels higher
    line_profile = image[center_y - 2, start_x:end_x + 1]

    return line_profile
```

Figure 45: Code; extract_horizontal_line_profile Function

Figure 45 displays the function used to extract the line profile; the inputs of this function is the particle image, the X & Y coordinates for the particle and the pixel length of the line profile. The line profile must be within the bounds of the image, indicated by the height ‘h’ and width ‘w’ parameters, with ‘none’ indicating a line profile cannot be extracted. The code calculates the line profile start and end (‘start_x’ & ‘end_x’) in order to place the horizontal line between these values, with the y-coordinate for each being the particle centre_y parameter. The line profile is adjusted slightly for height, as the particle denoising technique used (i.e erosion) may slightly compress the detected particle in the Y-axis. The result of this function is a one dimensional array of the intensity values along this line profile. This function will later be used to extract the line profiles of each detected particle at each step along the reconstruction length.

.

```
for idx, image in enumerate(image_array):
    image_rgb = cv2.cvtColor(image, cv2.COLOR_GRAY2RGB)  # Convert image to RGB
    for center, tag in zip(particles_centers, particles_tags):
        center_x, center_y = center
        color = (0, 0, 255)  # Red color for particles
        add_center_highlight(image_rgb, center_x, center_y)
        cv2.putText(image_rgb, tag, (center_x - 10, center_y + 20), cv2.FONT_HERSHEY_SIMPLEX, 0.5, color, 1)

        # Extract horizontal line profile
        line_profile = extract_horizontal_line_profile(image, center_x, center_y, line_length)

        # Store line profiles in the corresponding dictionary based on their tags
        if line_profile is not None:
            line_profiles_by_tag[tag].append(line_profile)

        # Draw the line profile on the image
        if line_profile is not None:
            line_y = center_y
            line_x1 = center_x - line_length // 2
            line_x2 = center_x + line_length // 2
            cv2.line(image_rgb, (line_x1, line_y), (line_x2, line_y), (255, 255, 255), 1)
    cv2.imwrite(f"Edited_Image_{idx}.png", image_rgb)
    imageEdit.append(image_rgb)
```

Figure 46: Code; Line profiles of detected particles

```
# Save line profiles for each tag
for tag, line_profiles in line_profiles_by_tag.items():
    tag_folder = f"Line_Profiles_{tag}/"
    os.makedirs(tag_folder, exist_ok=True)
    for idx, line_profile in enumerate(line_profiles):
        profile_filename = os.path.join(tag_folder, f"{tag}_profile_{idx}.txt")
        np.savetxt(profile_filename, line_profile)
```

Figure 47: Code; saving line profiles

Figure 46 shows the code relating to the extraction of horizontal line profiles of each detected particle. The code iterates through each holographic intensity image and for each detected particle extracts a line profile centred at the coordinates of each particle. These line profiles are then stored in a dictionary, “line_profiles_by_tag” (Figure 47), categorising the line profile by the P-tag (particle number). The line profile is also drawn over the intensity images, allowing the position of the line profile relative to the particles to be observed. This code allows each particle’s line profile, over the reconstruction length, to be archived for future analysis for each individual particle.

5.6.5: Particle Sizing

```
# Loop through the particle tags and analyze them
for tag in particles_tags:
    if tag.startswith("P"):
        line_profiles_to_plot = line_profiles_by_tag[tag]

        # Find the profile with the minimum intensity
        min_intensity_profile_idx = np.argmin([np.min(profile) for profile in line_profiles_to_plot])
        min_intensity_profile = line_profiles_to_plot[min_intensity_profile_idx]

        # Calculate the threshold as intensity of the minimum point plus half of the range
        threshold = np.min(min_intensity_profile) + (
                    np.max(min_intensity_profile) - np.min(min_intensity_profile)) / 2

        # Round the threshold crossings to the nearest integer
        threshold_crossings = find_threshold_crossings(min_intensity_profile, threshold)
        threshold_crossings = np.round(threshold_crossings).astype(int)

        # Calculate the particle size
        sensor_pixel_um = 2.2
        particle_size = calculate_particle_size(threshold_crossings, sensor_pixel_um)
        Z3 = Z2 + (mmStep * min_intensity_profile_idx)
        magFact = Z1 / (Z1 + Z3)
        sensor_pixel_um = 2.2
        if len(threshold_crossings) >= 2:
            total_length_below_threshold = threshold_crossings[-1] - threshold_crossings[0]
        else:
            total_length_below_threshold = 0
```

```
        particle_size = (total_length_below_threshold * sensor_pixel_um) * magFact

        # Categorize the particle based on its size
        category = find_particle_category(particle_size)

        # Print the particle tag and size category
        print(f" ")
        print(f"Particle Tag: {tag}")
        print(f"Particle Size: {particle_size:.2f} microns")
        print(f"Particle Size Category: {category}")

        # Save the reconstruction image for this particle
        if category != "UnderBounds":
            reconstruction_image = image_array[min_intensity_profile_idx]
            reconstruction_filename = os.path.join(file_path, f'{tag}_Reconstruction.tiff')
            cv2.imwrite(reconstruction_filename, reconstruction_image)
            #print(f"Reconstruction image for {tag} saved as {reconstruction_filename}")
```

```
            # Save the line profile graph as P[number]_Profile in an appropriate image format
            profile_plot_filename = os.path.join(file_path, f'{tag}_Profile.png')
            plt.figure()
            plt.plot(min_intensity_profile, label=f"Profile {min_intensity_profile_idx} (Min Intensity)")
            plt.axhline(y=threshold, color='r', linestyle='--', label='Threshold')
            avg_profile = np.mean(np.array(line_profiles_to_plot), axis=0)
            plt.plot(avg_profile, label=f"Average Profile")
            plt.xlabel("Position")
            plt.ylabel("Intensity")
            plt.title(f"Line Profiles for Tag {tag} - Min Intensity with Threshold Line")
            plt.legend()
            plt.savefig(profile_plot_filename)
            plt.close()

titleBanner("Final Readout", True)
print("Total Number Of Particles:", particles)
print("Number of RBC:", catCountRBC)
print("Number of WBC:", catCountWBC)
print(" ")
cv2.waitKey(0)
cv2.destroyAllWindows()
```

Figure 48: Code; Particle Sizing

The archived line profiles are then used later, shown by Figure 48 (which forms a single code block). The purpose of this code section is to utilise the archived line profiles to detect the point of minimum intensity (assumed point of reconstruction), and use this line profile and thresholding to differentiate between the particle and background inorder to calculate a pixel length that is then used to size and categorise the particle.

The code block functions by iterating through the P-tags (ignoring obstructions [O-tags] and fragments [F-tags]), and for each particle selects the relative line profiles. Using this batch of line profiles, the line profile that displays minimum intensity is selected as the reconstruction image. To size the particle, the threshold of the midpoint of intensity range, is used - allowing adequate differentiation between the particle and background, which should already be well contrasted. Using the central crossings (where the line profile intersects the threshold), a pixel distance is calculated which is the calculated particle pixel diameter, which is multiplied by the pixel sensor size and a multiplier based on the reconstructed distance (only required for larger Z2s such as with camera guard). This results in a particle size, for each particle, in microns, which is categorised based on the defined size range & tolerance for each particle type.

6: Testing

6.1: Sample Preparation

6.1.1: Artificial Blood Samples

As mentioned, for the majority of testing, an artificial blood alternative was used to avoid biohazard and ethical issues surrounding clinical samples.

Three sized particles were used, 45µm, 15µm, 10µm. The 15µm and 10µm are comparable to WBCs and RBCs respectively. Extremely dilute suspensions of these particles are created, with a mixture of three also being created. As dilution increased, the particles were easier to differentiate and count as well as being less likely to form aggregates, with ideal dilution depending on the channel thickness / volume, as being a visual method is susceptible to particle stacking / crowding.

The samples needed to be regularly shaken to avoid particles falling out of suspension and forming a pellet at the bottom of 1 mL PCR tube.

6.1.2: Clinical Sample

A biological sample was required for further practical validation of the use of the bespoke LDHM device for differentiation and count of particles; specifically blood cells in the context of this project.

For testing with a blood sample, the decision was made to use lab rat blood samples opposed to human samples. The use of human blood requires screening the blood against bloodborne diseases, as well as carries ethical considerations and justifications. The lab rats used are known to carry no bloodborne diseases, and the sample is taken in a minimally invasive way so as to not cause any long term harm to the animal. Rat blood is also comparable to human blood in terms of cell size - with rat RBC being 6.5 microns[60], and human RBCs being 7.5 - 8.7 microns [59].

Two blood samples were used: whole blood (diluted) and a RBC lysed sample (inorder to isolate the WBC population). The two different samples allowed for easy identification and categorization manually, before introducing computer vision analysis.

A whole blood sample batch was made using a small amount of blood, 100ul, suspended in 1 ml of Phosphate Buffered Saline (PBS). This sample itself proved to be too cell-dense for LDHM use, and required heavy dilution to avoid large cell populations or aggregation.

A similar sample was created for a RBC lysed sample. This sample was further suspended in 1ml of ammonium chloride, which was then incubated over ice for 5 minutes. This was then vortexed and incubated for further 5 minutes, after which 3 ml of PBS2%FBS was added, and the mixture centrifuged for 5 minutes at 300xg. This created a cell pellet and supernatant fluid, the latter of which was removed. The cell pellet was then resuspended in PBS. The results in a sample that is mostly white blood cells, which is particularly useful for reference when identifying them in mixed samples.

6.2: Experimental Plan & Device Operation

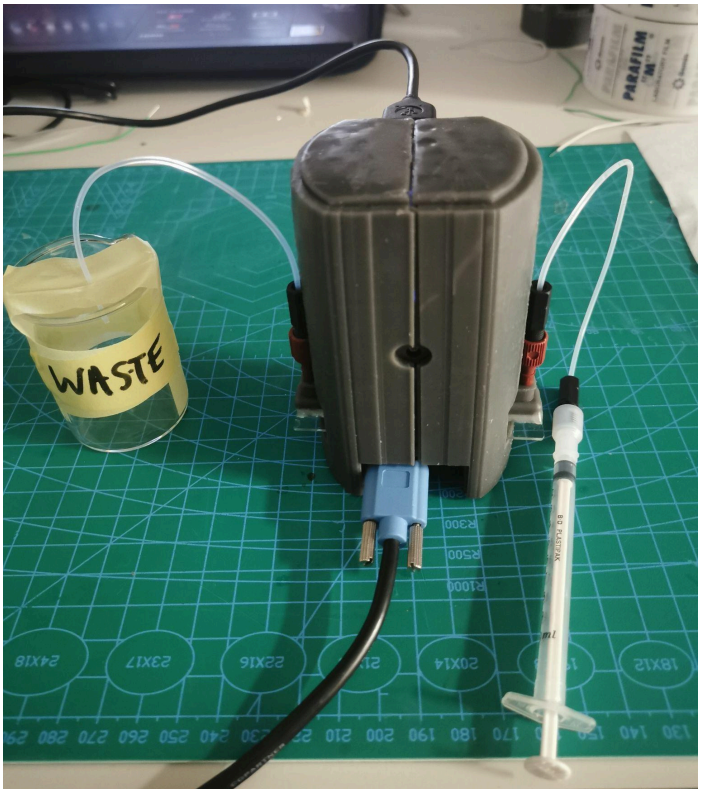

Figure 49: Experimental Prototype

To validate the device's operation, experiments had to be performed using artificial and biological samples.

As part of an iterative design process, experiments had to be performed using artificial samples and the computer vision software, in order to ensure that the software performed as intended. The data from these experiments were used to further develop the software and combat issues discovered over the course of experimentation, such as contamination handling, utilising denoising techniques,etc. Once results were obtained for artificial samples that displayed good accuracy, the direction of experimentation would shift to biological samples.

The prototype device, Figure 49, has a specific procedure of operation to ensure functionality as intended.

Experimental Operation:

1. Set-up device:
    a. Place components (i.e. Camera, pinhole, LEDs, circuit boards & wiring) into the appropriate 3D printed holders / sections.
    b. Construct the internals of the device (i.e the holders) into the correct vertical stack, the holders are only compatible with the relevant connectable parts.
    c. Attach the device casing to the outside of the internal stack, holding the internals together.
2. Set-up software:
    a. Create an empty folder for image data.
    b. Ensure that the correct device camera is selected in code, ‘0’ being default device camera, ‘1’ being secondary, as well as the resolution defined.
    c. Ensure that important settings, such as wavelength, reconstruction distance are set.
3. Clean microfluidic glass:

    a. Thoroughly clean to remove settled dust, fingerprints and other FOD from the surface. Liquid such as de-ionised water or isopropyl alcohol can be used to clean the surfaces, as long as the surfaces are fully dry before use. The inner channel and surfaces should remain clean from the microfluidic assembly stage.
4. Insert microfluidic casing slot:
    a. The microfluidic device should be inserted so that the end sections of the I/O ports block the casing slot, shielding the sample chamber from ambient light.
5. Connect microfluidic tubing to ports
    a. Tubing should be connected to the microfluidic I/O ports securely, to avoid leaking or disconnecting.
6. Connect a waste collection to outlet
    a. The outlet tubing should be flowing into an appropriate waste collection container. This container should be appropriately labelled and disposed of later.
7. Start the software
    a. Start the software, follow instructions provided by the console postings
    b. A windowed live videofeed of the device camera should appear if set-up correctly. If not, check wired connections, software settings or camera functionality via the inbuilt camera app.
8. Align pinhole / LED (optional)
    a. The LED / Pinhole may display alignment issues, if the appropriate sections are used (i.e the XY shifting holders), one or more of these sections should be able to be shifted by moving the alignment screws.
9. Flood the microfluidic channel with a buffer solution.
    a. Using a syringe, flood the microfluidic channel with a buffer solution, this task can be aided by the live videofeed.The microfluidic channel should be free of air bubbles.
10. Capture background image.
    a. When the channel is appropriately filled with buffer solution, use the software to capture the background image. After this image is captured, the device is sensitive to movement and changes in light levels - if the microfluidic moves , or ambient light changes, after this stage then the subtraction code will produce errors.
11. Using a syringe introduce sample to microfluidic.
    a. Using the syringe, pump the sample into the microfluidic channel. Be careful not to move the microfluidic device, the LDHM device or introduce air bubbles into the channel. Ensure the sample fluid has flowed completely to the end of the channel before beginning the next step - particles should be visible to indicate to what point the sample has flowed to in the channel.
12. Take experimental images.
    a. Using software, take an experimental image.
    b. (optional) View images in folder, confirm you want to use the images collected.
13. Data automatically collected, analysed and output provided.

6.2: Artificial Sample

6.2.1: 45 Micron Spheres

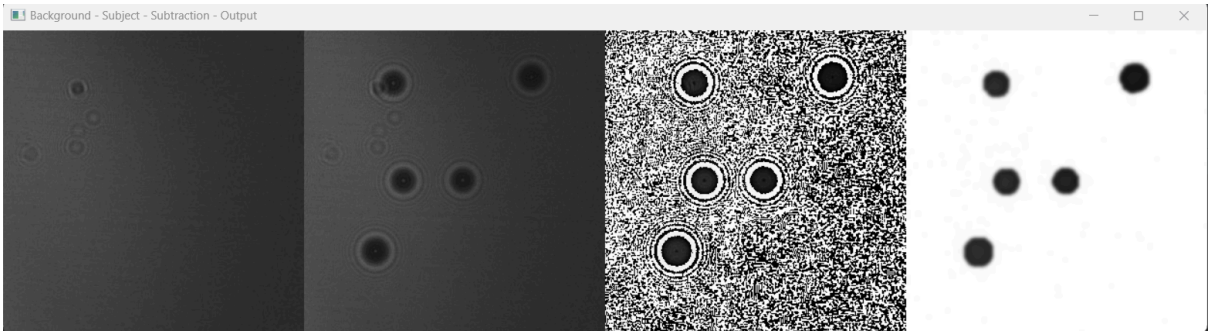

Figure 50: Stacked images; 40µm spheres

Figure 50 shows a series of 4 output images: The background image, the subject ("experimental") image, a subtraction image and an extracted "output" particle image.

The background image is a raw image taken of the microfluidic channel, loaded with a buffer fluid. The background is mostly uniform, some particles are observed in the top left corner of the images; these are small particles, i.e. dust particles, on either the camera or microfluidic glass. FOD, such as dust, is minimised by cleaning the microfluidic device / camera before insertion; despite this, the image is rarely free from all contamination, making the subtraction and extraction of true particles necessary. The microfluidic is flooded with buffer fluid prior to taking this background image to avoid the background and subject images varying due to the refraction effects of introducing fluid.

The subject image is the image taken after a sample has been introduced, in this case 45µm spheres. In this image large particles can be seen, with the interference pattern of contamination intersecting that of the particles. This intersection makes contour detection without particle extraction difficult, as the contamination-particle mix would resolve into a single entity.

The subtraction image, as described in section 5, is a literal subtraction where the two images are converted into a two-dimensional matrix and bitwise subtracted to produce these subtraction images. This image's purpose is to highlight the difference between the two images, such as the introduction of particles, while ignoring the similarities between, such as the static contamination. Ideally, the result should be only the particles that have entered the scene, however, noise that varies between images is also captured. Depending on the noise level, it may be beneficial to employ denoising techniques such as gaussian blur to both images prior to subtraction.

The extraction image is a product of using erosion and dilation functions on the subtraction image; as previously mentioned erosion "erodes"(removes) small, black details in an image; this aids in removing the noise captured, though results in larger black details, such as the particles, being 'squashed' or reduced in size. Once smaller details are removed, a dilation function, used to expand dark features in an image, is used to reverse this, allowing the particles to be expanded to a shape and size comparable to their original size. This results in an image that highlights only the particles that were introduced when the sample was inserted.

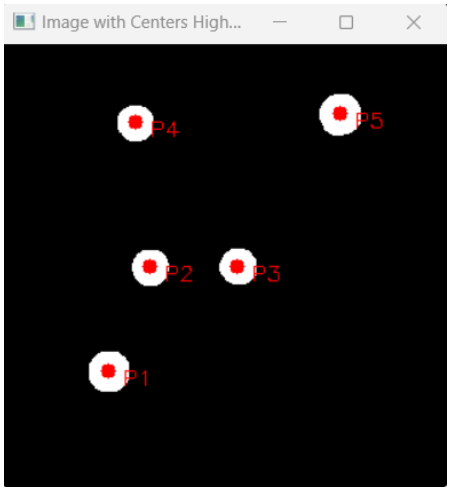


```
Number of Fragments: 0
Number of Particles: 5
Number of Obstructions: 0
```

Figure 51: Detected particle & Initial Count (45µm)

This extraction image, cannot easily be used for particle differentiation and sizing past situations where there is a large difference between particles and the particles have a known size for these respective groups. Therefore a method of sizing particles had to be implemented and differentiate these cells into groups based on this size. Figure 51, shows an inverted extraction image, which using a centre of mass function, the centre of each particle has been located and tagged, producing a preliminary total count of particles, fragments (e.g. unremoved noise / interference pattern artefacts, defined as size less than 150 (area) by default settings) and obstructions (large blocking objects - defined as being too large for a particle, by default defined as greater than 500 (area) by default settings). The tagging is important for processing particles individually, as well as later defining them by a group sizing tag.

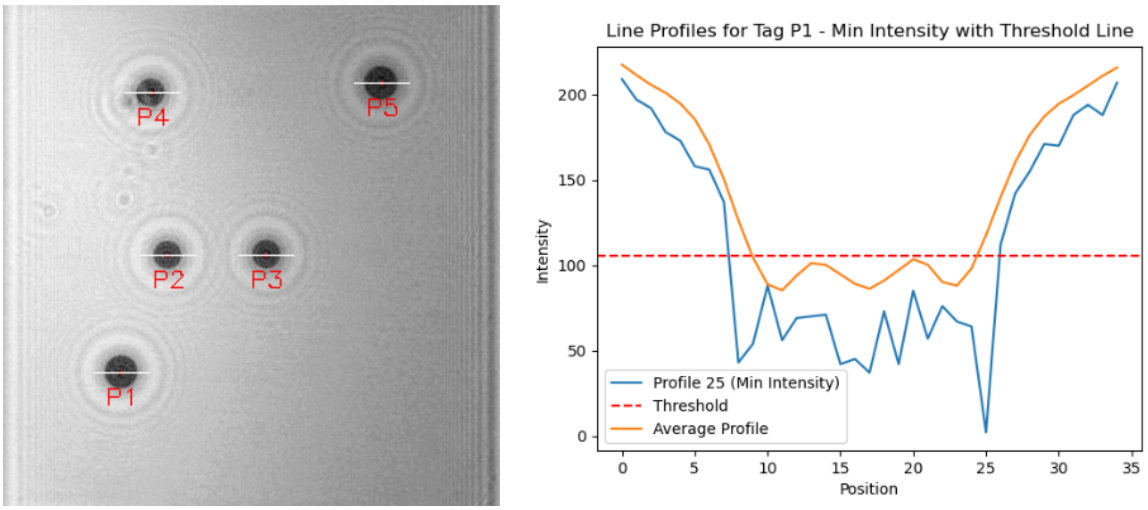

Figure 52: Line Profiled Reconstruction & example line profile

Using these centres identified, a line profile is created horizontally across the position of the particles, using the centre coordinates as the midpoint of the line profile. This line profile is calculated for each particle during each step stage of the reconstruction. Figure 53 shows a point in the reconstruction with the line profiles drawn through the tagged particles. Each particle therefore has a batch of line profiles, the line profile that shows the largest contrast (i.e the profile that has the point of minimum intensity comparatively) is selected as the point of reconstruction for that particle. The line profile is then analysed; using a threshold equal to the midpoint of intensity range across the line profile. At the points of crossing, where the threshold meets the line profile, the

length of the particle is taken, assuming the magnification is unit, and with a physical pixel size of 2.2µm, the true particle size can be calculated.

```
Particle Tag: P1
Particle Size: 46.27 microns
Particle Size Category: 45um
Particle Tag: P2
Particle Size: 36.89 microns
Particle Size Category: 45um
Particle Tag: P3
Particle Size: 44.73 microns
Particle Size Category: 45um
Particle Tag: P4
Particle Size: 44.89 microns
Particle Size Category: 45um
Particle Tag: P5
Particle Size: 53.54 microns
Particle Size Category: 45um
```

```
Total Number Of Particles: 5
Number of 10um Particles: 0
Number of 15um Particles: 0
Number of 25um Particles: 0
Number of 45um Particles: 5
Number of Unknown Particles: 0
```

Figure 53: Particle sizing, categorisation & final readout

This calculation produces a readout of the particle tag and their calculated size, as shown in Figure 53. Then the total particle count is reiterated - which may be amended - as well as the number of particles in each group; the example in image X uses example categories defined in code; these groupings can be altered depending on the application / particle sizes.

6.2.2: 15 Micron Spheres

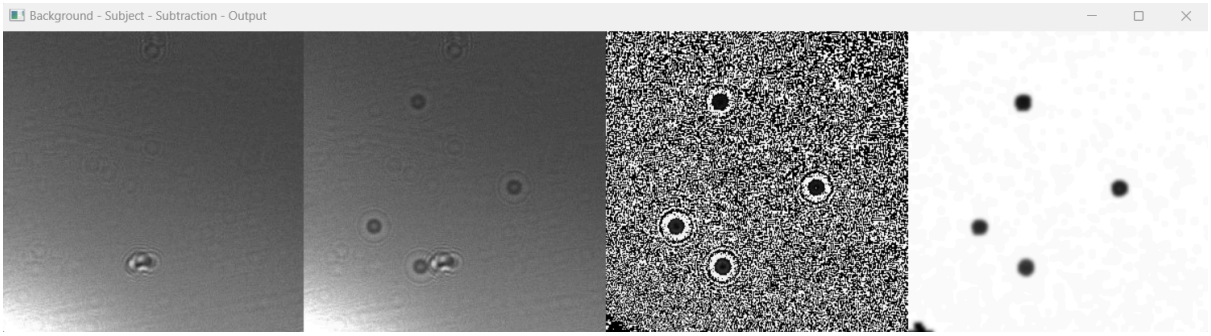

Figure 54: Stacked Images; 15um Spheres

Figure 54 shows a similar “Background,Subject,Subtraction, Output” image for an example using 15µm particles. Included in this example is a larger contamination particle just below the centre of the image, as well as a visual obstruction in the bottom left corner of the image, caused by The LED brightness being increased resulting in a bright spot / visual dead zone on the captured image. As a result, the bright spot causes the subtraction to generate a false particle, tagged as “P1” in Figure 55 also resulting in an incorrect readout, producing a count of 5 particles, rather than the 4 particles in this example. The method for extracting the particles however remains resilient against FOD, despite in this example being comparable to the size of the particles.

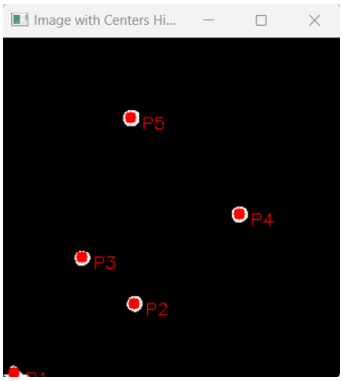


```
Number of Fragments: 0
Number of Particles: 5
Number of Obstructions: 0
```

Figure 55: Particle detection & initial readout; 15µm sphere


```
Particle Tag: P1
Particle Size Category: OutOfBounds
```

Figure 56: False Particle ('P1') Out Of Bounds Sizing

However, the line profile for false particle 'P1' does not have multiple crossings observed in a peak caused by a particle, this results the false particle to be categorised as "OutOfBounds" (Figure 56); a categorisation for disregarding particles that are partially imaged, where the resolved particle is either fully or partially out of view at the edges of the captured image. This results in the particle being declassified as a particle, reducing the original count from 5 particles to 4; the correct number of particles.

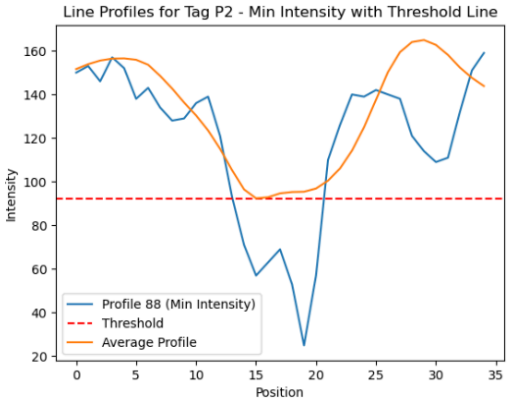


```
Particle Tag: P2
Particle Size Category: 25um
```

Figure 57: Particle ('P2') incorrect Sizing (interference)

Particle 'P2' is the particle that is intersected on the right by a relatively large contaminant particle. While this contaminant is able to be removed for extracting and identifying P2 as a separate entity, due to the line profile being taken from the reconstruction image, the FOD is still included, which is unavoidable due to reconstruction not being viable on the subtracted or extraction images. As a result, as the interference pattern of the FOD is reconstructed, the particle's reconstruction is affected, this results in the right side in the line profile being

disturbed; resulting in the peak being broadened and the resultant particle sizing being falsely calculated as a result, as shown by Figure 57.

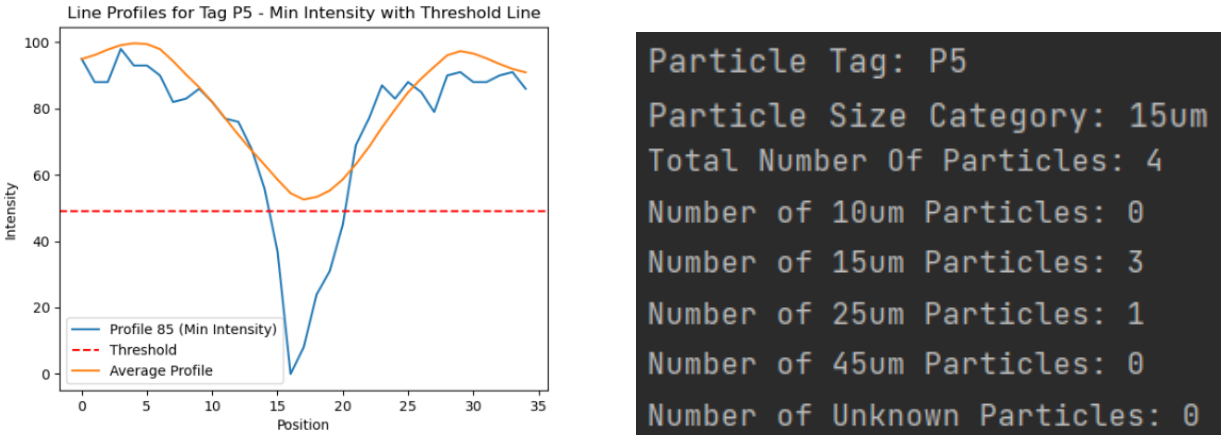

Figure 58: Particle ('P5') Correct Sizing and final readout.

Using particle 'P5' as a line profile example, particles ''P3', 'P4' & 'P5', being true particles unaffected by FOD, were reconstructed successfully and correctly categorised as 15µm particles, as shown by Figure 58. Given the two errors, the count was amended to the true amount of particles, though the size of particle 'p2' was still calculated in error, The final readout shows the correct total number of particles, with the calculated size groups.

6.2.3: 10 Micron Spheres

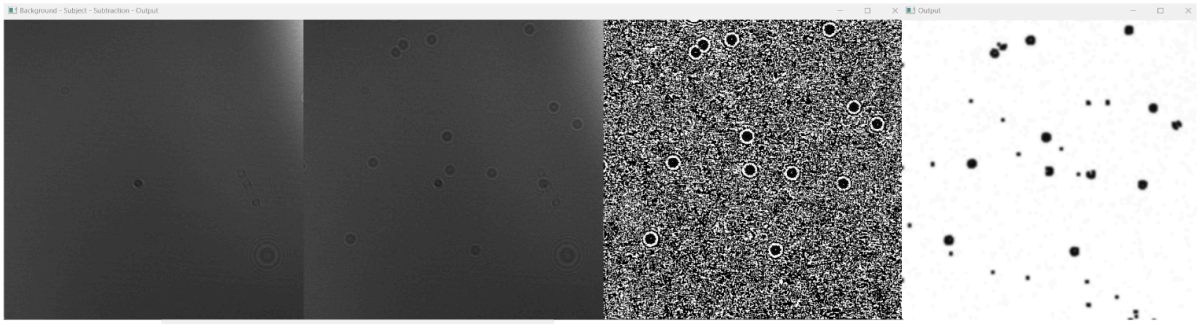

Figure 59: Stacked Images; 10µm Spheres

Figure 59 shows a similar "Background, Subject, Subtraction, Output" image for an example using 10µm particles. However, in this example, the notable difference, other than particle size, is the artefacts that exist in the particle extraction image. These artefacts exist where random noise resulted in dark clusters that survived the erosion function, and then expanded by the dilation function.

In Figure 60, these small artefacts are tagged as fragments, as their size falls into the relevant category. As mentioned, these do not get processed. The initial readout notes the number of these fragments in the image, as well as the correct number of 10µm particles.

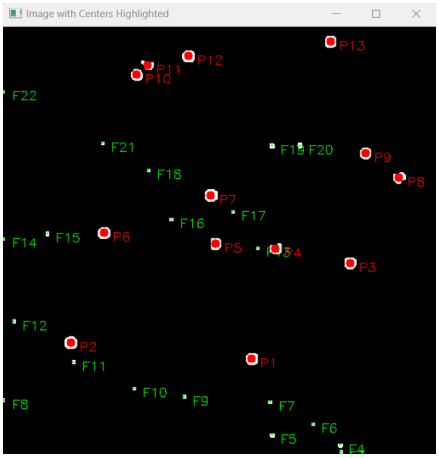


```
Number of Fragments: 22
Number of Particles: 13
Number of Obstructions: 0
```

Figure 60: Particle Detection; 10µm Spheres & initial readout

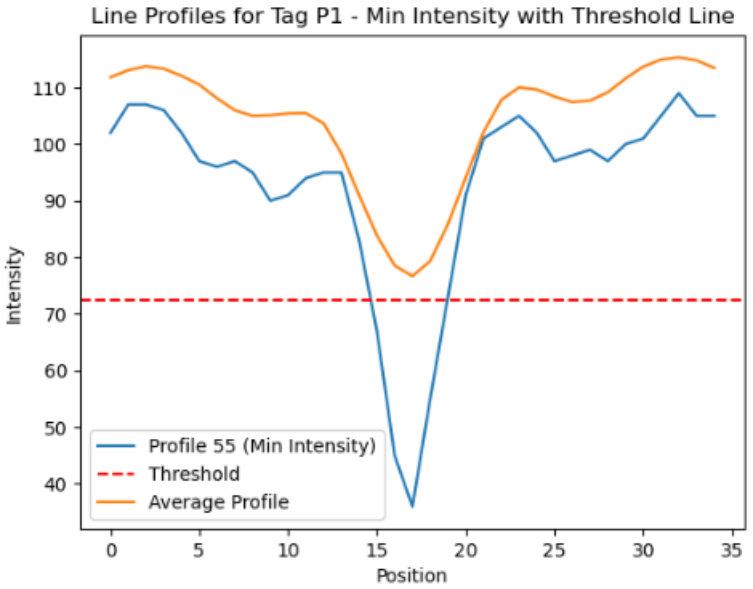


```
Total Number Of Particles: 13
Number of 10um Particles: 13
Number of 15um Particles: 0
Number of 25um Particles: 0
Number of 45um Particles: 0
Number of Unknown Particles: 0
```

Figure 61: Particle ('P1') Correct sizing and Final Readout

Using particle 'P1' as an example, shown in Figure 61, the particles in this example reconstructed well, producing well defined peaks that allow for easy differentiation from the background resulting in all particles corresponding to the 10µm category.

6.2.4: Mixed Sphere Sample

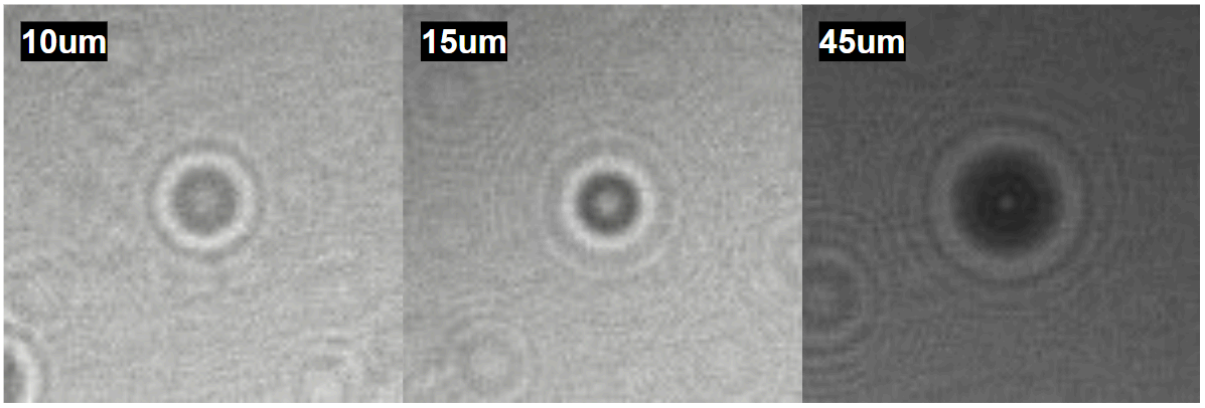

Figure 62: Stacked Images; 10µm , 15µm, 45µm sphere holograms

To validate the ability to differentiate between particles, mixed particle samples were also used. Figure 62 shows a compiled comparison of a 10,15 and 45 micron particle. The similarity in the appearance of the 10µm and 15µm holograms in particular highlight why holographic image based differentiation is a difficult task for human and computer alike, resulting in the need for a reconstruction based method.Figure 63, shows the sizing for each particle category.

```
def find_particle_category(particle_size):
    # Define the size ranges for each category
    size_categories = {
        "OutOfBounds": (0, 0),
        "10um": (7, 12.5),
        "15um": (12.51, 17.5),
        "25um": (17.51, 35),
        "45um": (35.01, 55)
    }
```

Figure 63: Artificial sample Categorisation ranges

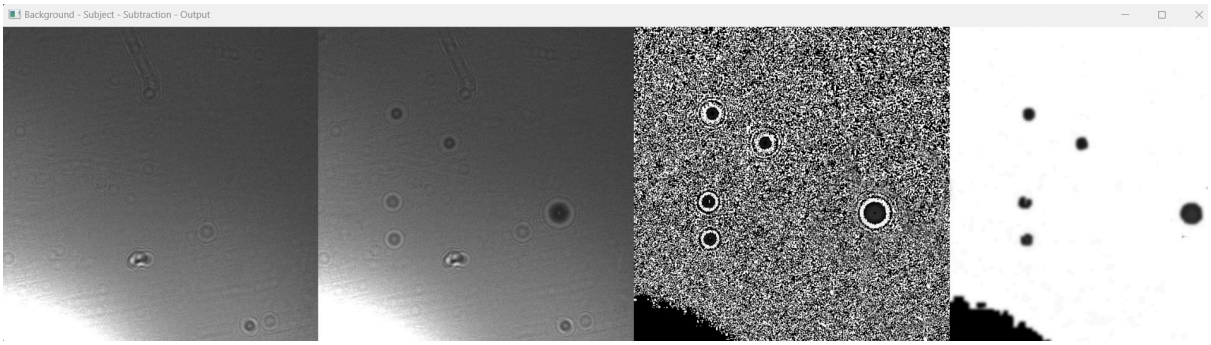

Figure 64: Stacked Images; Mixed Spheres

Figure 64 shows the “Background, subject, subtraction, output” compilation of a mixed sample experiment. In this example, there are multiple instances of contamination, as well as a relatively large “dead zone” caused by the LED. In the subject image, the two particles in the top left are 15µm, the two particles in the mid to bottom left are 10µm and the particle approximately mid right is 45µm.

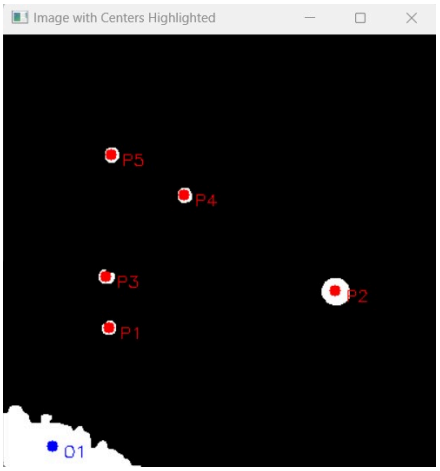


```
Number of Fragments: 0
Number of Particles: 5
Number of Obstructions: 1
```

Figure 65: Particle Detection; mixed spheres & initial readout

Figure 65 shows the tagging of the extracting particles, as well as the "dead zone" being correctly tagged as an "Obstruction". Similar to fragments, Obstructions (e.g. 'O1') are not processed.

Figure 66: Particle Sizings; line profiles for 10µm,15µm, 45µm particles respectively

Figure 66, shows the line profiles for a 10µm, 15µm and 45µm respectively, as seen the line profile broadens as the size of the particle increases, as expected. As shown, with the threshold being adaptive, the thresholds for all particles are all different, however defined by the same function, selecting the midpoint of the intensity range (midpoint between the minimum and maximum of the profile); ensuring what is taken into account is sufficiently contrasted to the background.

```
Particle Tag: P1
Particle Size Category: 10um
Particle Tag: P2
Particle Size Category: 45um
Particle Tag: P3
Particle Size Category: 10um
Particle Tag: P4
Particle Size Category: 15um
Particle Tag: P5
Particle Size Category: 15um
```

```
Total Number Of Particles: 5
Number of 10um Particles: 2
Number of 15um Particles: 2
Number of 25um Particles: 0
Number of 45um Particles: 1
Number of Unknown Particles: 0
```

Figure 67: Particle Sizings; Mixed particle final readout

As shown in Figure 67, the 5 particles are categorised, correctly identifying P1 & P3 as 10µm, P2 as 45µm and P4 & P5 as 15µm; this is summarised in the final readout.

6.3 Clinical Sample

Using sphere-based samples displayed LDHMs potential for particle sizing and differentiation when coupled with computer-vision. While this is a good indication of its effectiveness and potential for translation for biological samples, i.e. blood samples, further testing using clinical samples is required to confirm this.

6.3.1: Traditional Microscopy Of Blood Samples

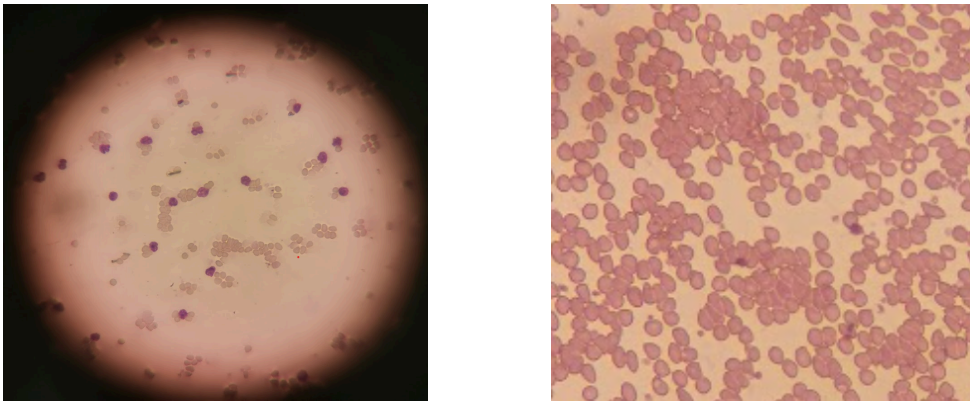

Figure 68: Blood Sample under traditional Microscope (Whole & RBC Aggregate)

Using a traditional microscope; a dilute & undilute whole blood sample was imaged, shown by Figure 68. Viewing the sample under a microscope allows for potential issues with the translation from spheres to cells to be assessed, as well as indicating if the settings used for spheres (e.g. grouping ranges) would have to be altered.

A potential issue with blood cells is aggregation, as shown in Figure 68 (right) which highlights how an undiluted blood sample is too cell dense for the method of computer vision used. However, Figure 68 (left), which is far more dilute, also shows the cells naturally tend to aggregate. This aggregation may make it difficult to either distinguish cells from each other or cause errors in sizing.Another issue with cells is the variation within the same cell groups in regard to shape; the microbeads used in the artificial samples were uniform spheres, where cell appearance is not only naturally varied, but also dependent on orientation of non-spherical cells, i.e RBCs.

6.3.1: LDHM Of Blood Samples

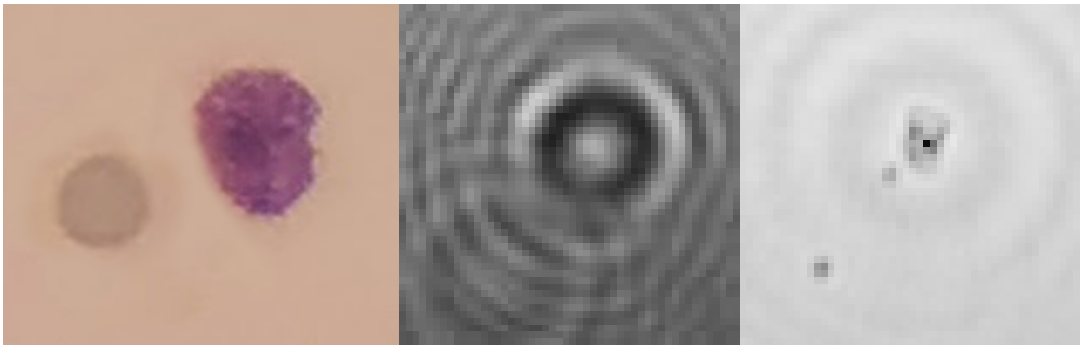

Figure 69: RBC & WBC under Microscope vs LDHM (Hologram,Reconstruction)

Figure 69 shows a stained blood sample with a RBC (left) and a WBC (right) as viewed under a traditional microscope as well as a comparable hologram image taken of an unstained rat blood sample, captured using LDHM device, using the reconstruction portion of the software showing a WBC and two RBCs (propagation variable 'z', set for WBC focus).

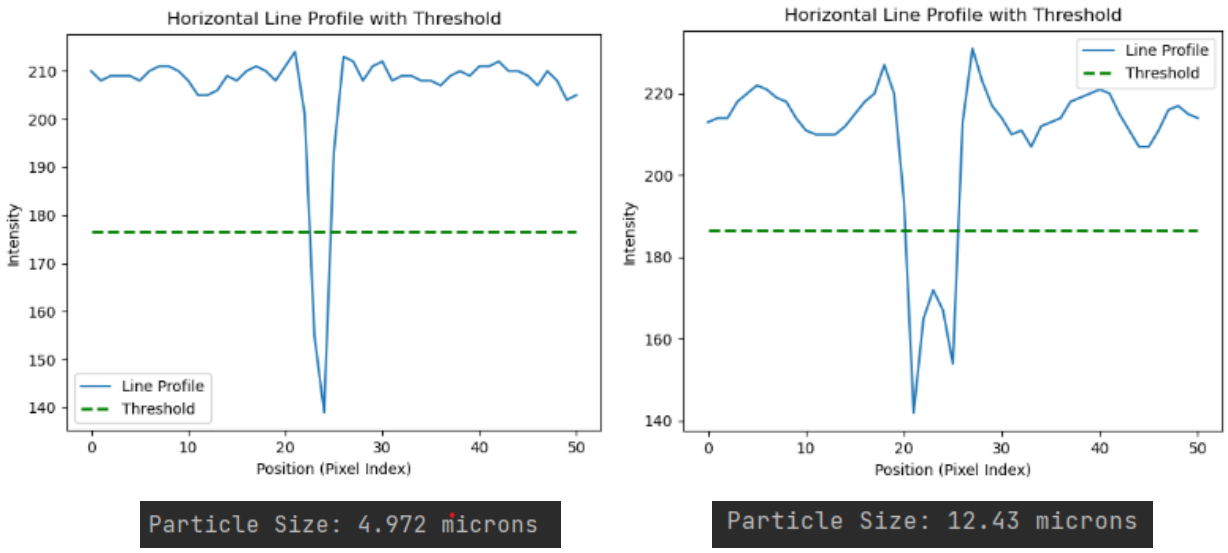

Figure 70: RBC & WBC Reconstruction Sizing Line Profile

Using a manual version of line profile code, the RBC and WBC were selected to determine particle size, in order to aid in the category sizes for the clinical sample version of the code. The sizes, based on the software, were approximately 5µm, and 12.4µm respectively, (Figure 70). Given these sizes were smaller than expected, with human RBCs and WBCs being approximately 8µm [60] & 15 µm [61] respectively, it was decided to assume this was a middle value, and size the categories to be ± the difference between this measurement and literature, resulting in the sizing groups of RBC = 5µm ± 3µm, WBC = 12µm ± 3µm.

Red Blood Cells:

Given their relative concentrations within blood, RBCs were the most common cell in the samples used, making capturing experimental images of these cells relatively easy.

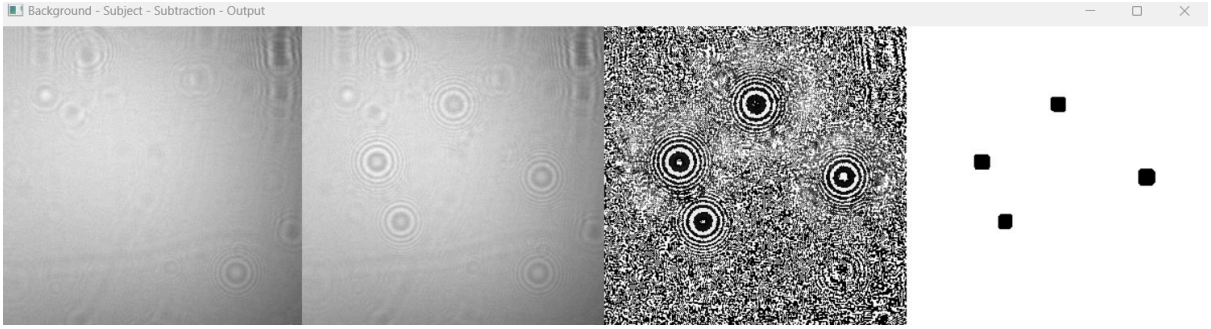

Figure 71: Stacked Images; RBC

Figure 71 (above) shows the stacked image output generated by the code, showing the background,subject (experimental), subtraction and final detection image. This displays the code's ability to detect the RBC holograms as well as remove static FOD / particles that are common in both images.

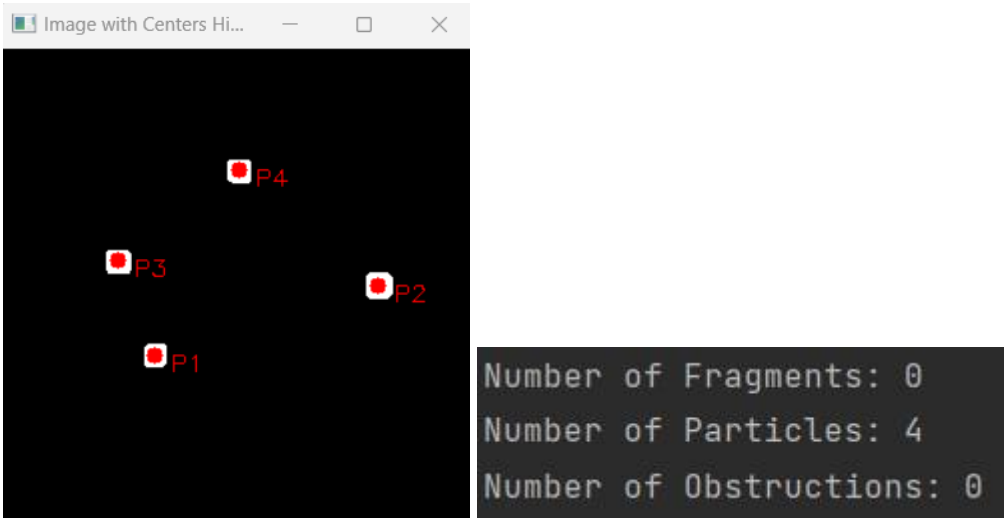

Figure 72: Particle Detection; RBC & Initial Readout

Figure 72 shows the P-tagged image and the relative console output, showing 4 correctly identified particles.

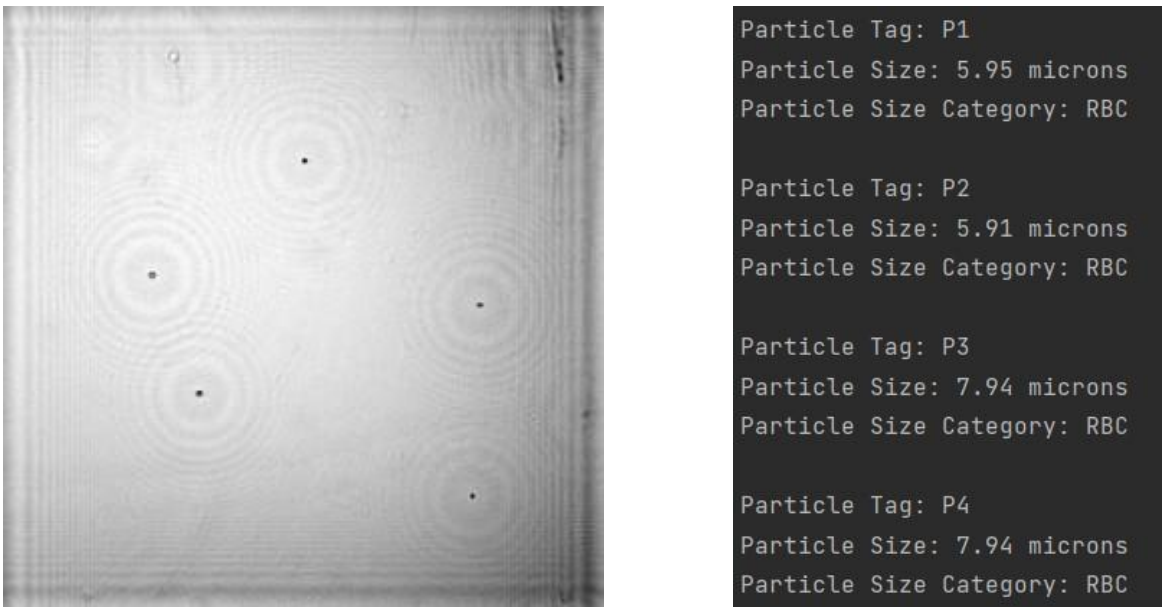

Figure 73: Particle Reconstruction, Sizing & Categorisation

Figure 73 hows the reconstruction of the subject image and the relative console readout. Shown are five reconstructed particles, four of which are counted while the fifth is disregarded as contamination (due to being in a static position in both images). The console readout shows the tagged particle, the calculated size and the category for each, correctly categorising the particles as RBCs for the calculated size.

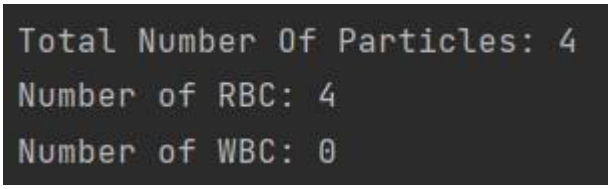

Figure 74: RBC Final Readout

Figure 74 shows the final readout, summating the total number of particles detected, as well as the the number of particles in each category.

Overall, for this size particle, the software displayed good accuracy, with minor errors relating to particles being too close to each other in the horizontal plane, being at the edges of the image, or the reconstruction of the particle being affected by the reconstruction of another close particle.

White Blood Cells:

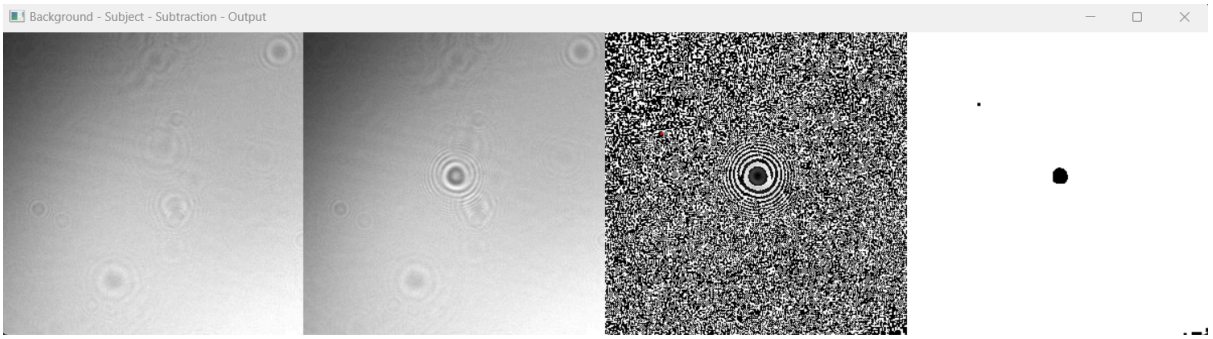

Figure 75: Stacked Images; WBC

Figure 75, above, shows the image stack output of the background, subject, subtraction and final output for a WBC sample, where a single WBC was isolated, imaged and sized.

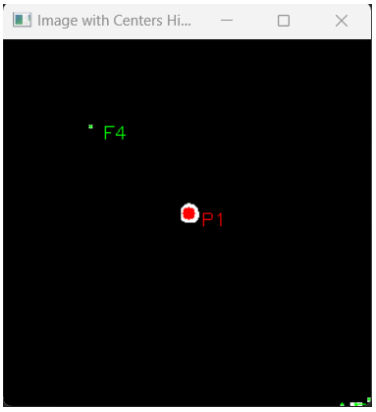

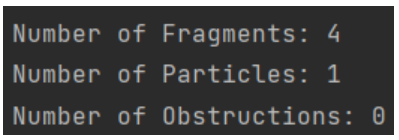

Figure 76: Particle Detection; WBC & Initial Readout

Figure 76 shows the tagged final output, with the readout displaying the number of detected particles, fragments and obstructions. Within this tagged image are four listed ‘fragments’ - in this instance they are artefacts generated by noise.

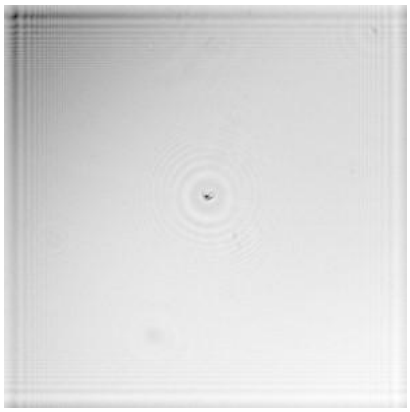

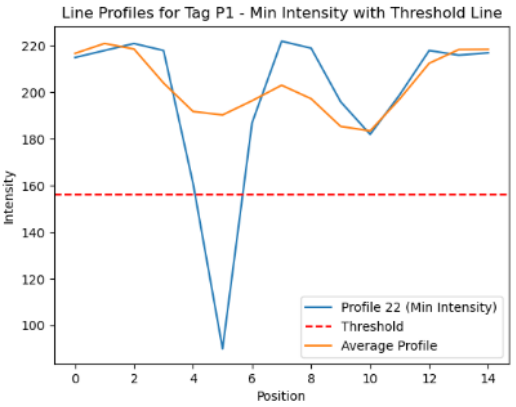


```
Particle Tag: P1
Particle Size: 0.00 microns
Particle Size Category: UnderBounds

Total Number Of Particles: 0
Number of RBC: 0
Number of WBC: 0
```

Figure 77: Reconstruction & Incorrect Line profile and Incorrect Sizing

However, despite the successful detection and reconstruction, the sizing of the parting is incorrect. There are two issues that contribute to this incorrect sizing. Firstly, looking towards the line profile graph generated, shown by Figure 77 , it can be noticed that the positioning of the 'peak' associated with detecting a particle, is in this case not centre. This screwed peak causes an error in versions of the code that utilise the first threshold crossing to the left and right of the centre to generate a pixel length of the particle as there are two left crossings and no right crossings. This results in the incorrect sizing of 0 microns, putting its category as "UnderBounds" and not including it as a RBC or WBC.

```
Particle Tag: P1
Particle Size: 4.40 microns
```

Figure 78: Alternative Sizing Method for WBC; incorrect

Adapting the threshold crossing method to be the first and last threshold crossing (a method that potentially suffers from errors caused by spikes in the background) then the pixel length is correctly interpreted. However, as shown by Figure 78, this calculation, while true to the graph, is incorrect for the expected particle. This displays the second issue - the non uniform shape and structure of cells. The line profile is based on the estimated particle centre generated by the centre of the holograms after image processing. This, within a degree of tolerance, works well for uniform particles, such as those used in the artificial samples. However, the complex shape and structure of WBCs in particular lead to the line profile centre being placed in sub-optimally or in positions where internal structures generate sharp intensity drops that can be triggered as crossings in itself, rather than the cell walls.

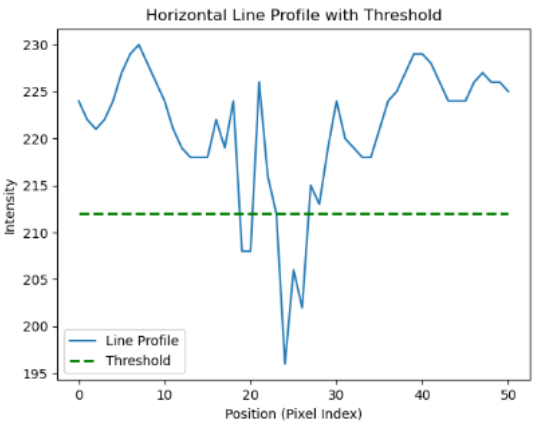

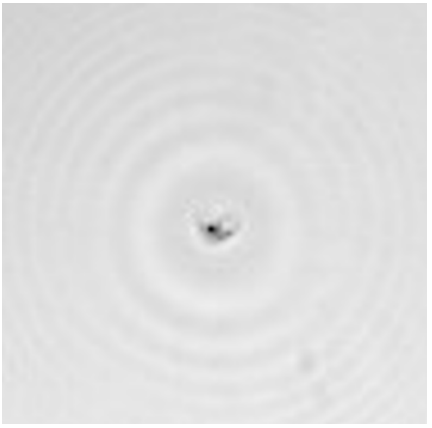

Particle Size: 19.469 microns

Figure 79: Manual sizing with Line Profile - High

Placing the line profile manually, using middle threshold crossing, however leads to a more appropriate reading. Generating a line profile, Figure 79 , in the centre of the particle, above the internal structure with a line profile width of 50 pixels, estimates the particle size to be 19.469 micrometres. The sizing, while quite over the range intended for WBCs. Though generating a line profile just under the internal structure provides a particle size of 11.681 micrometres, shown by Figure 80, which already falls within the WBC categorisation.

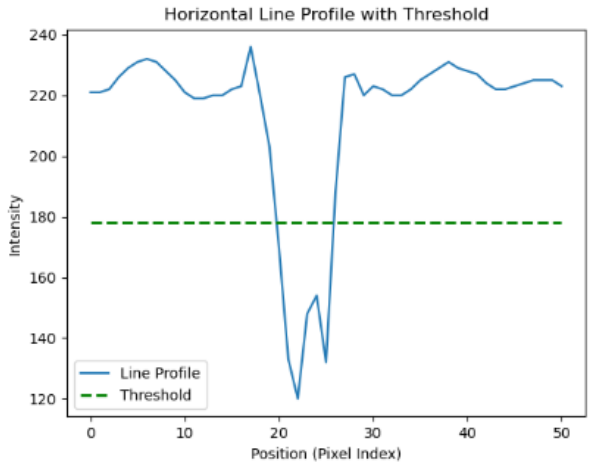

Particle Size: 11.681 microns

Figure 80: Manual sizing with Line Profile - Low

The two issues listed above were a constant for all WBC examples tested. With the automated method of sizing being unreliable, being able to differentiate between RBCs and WBCs by specifically categorising each is not possible, however sizing RBCs appears promising at this stage, though further development will be required for RBC/WBC differentiation and categorization. Overall, the identification, categorization and sizing of WBCs will require further development to become functional.

7: Discussion

7.1: Overview

The device utilised a shorter wavelength (420 nm, 15nm Bandwidth) LED, this design decision was influenced by the theory in section 2.4.1 as well as the preliminary experiments that investigated blue vs red LEDs (section 3.6.2) in terms of reconstruction contrast.
A small pinhole, 15µm, was also used due to the findings of the preliminary experiments. Though one of the benefits of LDHM is the ability to utilise smaller pinholes to avoid FOD blocking the pinhole/aperture, it was decided that within a sealed device, the quality benefits outweighed the potential for blocking the pinhole.
The 'Z1' parameter of the device accounts for the majority of the device length, being 6cm in length. While continuous improvement was displayed with an increasing Z1 parameter, larger lengths pushed the design into a direction that was less compact and top heavy, reducing the overall stability of the device. The length chosen was therefore a compromise between quality factors and usability factors.
Conversely, the 'Z2' parameter is negligible when compared to the total length of the device, being only 130um - 260um (+1mm with camera guard). This distance, as shown by theory and preliminary experiments, was desired to be small in order to bring the object plane as close to the sensor plane as possible, to maintain image quality and ensure a unit magnification. As the sample is both a liquid and would be a biohazard, there has to be some barrier between the sample and the sensor. This limits the 'Z2' barrier to thin transparent materials, which made traditional microscopy coverslips ideal. This material was thin, transparent and could be positioned flatly on top of the camera without damaging or contaminating the sensor.

The design posed a few technical challenges, such as section connectivity, electronic integration, ambient light shielding and section sizing. Each component (e.g. LED, Pinhole, camera) required a 3D printed holder, these holders had to be 3D printed separately, as smaller prints produced better quality. Through iterative design, the 3D printed sections were slimmed down to reduce the size of the device, with the aim of balancing the desired criteria of compactness with the preliminary experiments showing increasing quality with a larger Z1 parameter.

With the preliminary testing using open-air device style, it was noted during this experimental period that the captured image was sensitive to fluctuations in ambient light, which had further impacts on the computer-vision software. These sections , casing and holders, had to be designed to be easily connectable and to ensure alignment of the components, as well as compatibility with the microfluidic device and a protective / ambient light shielding casing, which too had to be designed with connectivity in mind. The casing design had to accommodate the internal sections, as well as house the electronic components, with access ports for the microfluidic and connectable wires for the LED & camera. With the internals of the device being in sections, slight variations in build could affect alignment, for this reason a simple X,Y screw and spring aligner was designed to adjust the pinhole to enable more central illumination of the sensor should the alignment be skewed.

The final design in this project is designed in a way to allow for easy assembly, disassembly and changing of components; this gives the final design a less than polished appearance, which for use outside of R&D would need to be altered into a more fixed structure, including alignment features being fixed after construction and before use. However, the design meets the criteria of being compact, lightweight, low cost, and low complexity, indicating suitability for translation into point-of-care use.
While the physical design is quite effective in use, certain design elements can be investigated further to ensure optimisation, such as the use of narrowband & coherent lasers over LEDs and fibre optic integration for pinhole replacement and angled imaging.

This project included a bespoke microfluidic device for sample delivery to the sensor plane of the LDHM device. This device was created using a standard glass microscope slide as a base. This slide had inlet / outlet holes drilled into either side through the slide with 3D printed luer locks attached to the top. Attached to the bottom of the slide was a coverslip; held in place by microfluidic tape, with a channel connecting the two ports.

As mentioned above, the use of glass coverslips enabled the ‘Z2’ parameter to be 130-260μm at minimum, negligible to the overall device size, while providing a better quality image (in terms of contrast) as well as limiting the magnification to near-unit.

The biggest challenges in the design of the microfluidic device were transparency, leak-proofing & creating a thin Z2 parameter. Transparency was paramount to the success of visualisation through the microfluidic channel. The need for transparency limited the choice of applicable materials, with glass being chosen for its transparency, durability and availability. Leak-proofing the microfluidic channel(s) was important to avoid contamination from samples as well as damaging electronic components, i.e. the camera. The microfluidic tape was applied in a way which created thick walls horizontally, allowing for a higher pressure to be tolerated before bursting. Epoxy was also used at the 3D printed port and glass boundaries, providing a second layer of protection should the tape fail. A thin Z2 parameter was required to bring the sample as close to the sensor plane as possible in order to create a magnification that was unit. Due to this thickness constraint , all 3D printed ports would have to be accessed via the top of the microfluidic as well as thicker glass components, i.e. glass slides, being used as a rigid top layer, rather than at the bottom like in traditional optical microscopy.

In terms of function, the microfluidic devices functioned well, providing a good transparent flow channel while being durable and leakproof. The standard slide increased the durability of microfluidic devices, making them resistant to light mechanical pressure, though easily broken if dropped. However, this design would not be suitable for a point-of-care solution - mainly due to flow being regulated either by the user or a syringe driving device; for this to be more suitable, the design would need to be altered to have some form of capillary based loading and flow or utilise a sample pumping mechanism, such as a microcontroller paired with a sample pump, to allow for a regulated, constant flow.

The project makes use of computer vision as a form of image analysis. The code design allows for the user to capture and store experimental images of a microfluidic device (background and subject images). These images are then processed; using particle detection via image subtraction and denoising to extract the particles within the sample. The holographic image captured is then reconstructed using the angular spectrum method, in order to produce more comprehensible images. The particles are then sized using line profiles taken across each particle in the reconstructed image. This produces a final readout of the number of detected particles and the number in each category, as well as the line profiles and reconstructed images saved.

Utilising computer-vision came with technical issues of its own, mainly contamination handling, particle identification and sizing. With multiple glass surfaces between the lightsource and the camera, contaminants were common, even with vigorous cleaning. As mentioned, these contaminants produce unwanted effects such as particle blocking, false particles counting and false sizing. The solution utilised was quite simple, by converting a background and an experimental image into two 2D arrays and carrying out a bitwise subtraction, details shared by the two images (i.e static contaminants) can be removed while details only in the experimental image (i.e particles in flow) and be preserved.The solution used does well at combating the effects of blocking and false counting , however sizing issues remain present - due to the reconstruction using an experimental image including the contamination.
Particle detection was aided by the contamination handling; with just the differences between the background and experimental images resulting in an image showing particles and noise. However, this noise at times attributed to “false particles” where dense noise was detected as its own entity, while usually, when this false particle was reconstructed, it resulted in an error and was automatically disregarded, sometimes FOD, artefacts at image edges, or other particle reconstructions would be read by the line profile, attributing a size to the false particle and thus including the particle into the count. The noise captured appears to have increased since moving from a RED LED source to BLUE LED, with significant noise found in darker regions of the image. Sizing the particle was overall the most difficult technical challenge; as the particle could sit anywhere in the channel volume, it was important to scan through the reconstruction-image stack and find the point of reconstruction for each individual particle before sizing them. Given the near unit magnification, the image captured is equal in physical dimension to the resolution of the image, multiplied by the physical pixel size of

the sensor, which is 2.2µm per pixel. Using this information and the centre of the particle as found by particle detection, a line profile can be taken at each stage of the reconstruction of a particle. Line profile displaying the highest contrast is taken as the point of reconstruction,calculated as the peak below threshold value of the midpoint between the min/max of the intensity range, allowing the particle pixel length to be measured, and a 'real' diameter to be calculated. However, as mentioned previously, the reconstruction includes unremoved contamination / blocking particles, which can lead to incorrect sizing of particles.

Computer vision as an analytical tool allows for complex analysis without human intervention, making the method applicable for point-of-care diagnostics. However, the software would have to have default settings that are physical device & sample specific, meaning that given the physical device is only a prototype, the computer vision software would have to be further optimised for a more standard design version, as well as sizing categories designed around an expected sample type.

Overall, computer vision based analysis proved an effective tool when coupled with LDHM technology; the visual nature of the computer vision analysis complemented the image data collected using an LDHM device well. With the computer vision style used being quite conventional, the rigidness (reliant on hard-coded defaults and categories) of the software used in this project could be made more flexible with the integration of AI and machine learning techniques for particle identification, sizing and categorisation. There are several features that could be implemented such as a rotating line profile to allow for the most appropriate line profile to be used in order to combat particle blocking related sizing issues. User inspired features, such as a reference / sizing grid, may be useful for manual analysis, which may aid in use or device / software validation.

During the testing phase of this project, both artificial and biological samples were used. As mentioned, artificial samples were initially used to avoid the potentially hazardous contamination and ethical issues surrounding blood samples, however they were extremely useful for software experiments, such as sizing, due to their consistent size and uniform shape. Blood samples however were still required for testing, to showcase the functionality of the device when applied to a biological sample.

The testing of the designed LDHM device, coupled with computer-vision, using artificial samples shows good accuracy, correctly identifying multiple different size spheres, within a tolerance, and being able to accurately differentiate between the sized particles. It is however worth noting that spheres are a very ideal sample, in terms of size and shape uniformity; this low variation in both parameters allowed for more constant results. This may highlight the potential for the translation of LDHM to other areas, such as inspection of clinical / lab products, such as spheres or other manufactured particles, as part of quality assurance in manufacturing, where there is a standard shape / size that is expected from the sample.

The testing of the designed LDHM device, coupled with computer-vision, using biological samples shows that while the software can be used for particle detection with fair accuracy, whilst the sizing features included are not appropriate for WBCs due to their complex structure and shape. Sizing, particularly for WBCs, would need further investigation, with avenues for advancement in quality (e.g. via different reconstruction methods, parameter or hardware changes, etc), detection (e.g. machine learning / AI) or sizing method (line profile alterations). The issue lies in the automatic detection and sizing of WBCs, as it is possible to capture, reconstruct and manually size WBCs accurately, there is difficulty with automatically identifying the particles, as well as the sizing method handling the internal structures , as the nuclei causes a drop in intensity across the line profile, generating multiple crossings of the threshold. Depending of handling of these instances (versions of the code utilised the first two crossings left and right of the centre of the line profile, while others used the first and last crossing), either the internal structure would either be sized or a mix of the internal structure in addition to the left or right cell wall depending on proximity, or the whole cell being sized though if noise in the line profile was sizable compared to the particle contrast , which is often the case with the virtual holograms in the images with smaller (less intense / less contrasted) particles, then the noise would be taken into account, generating a massively oversized calculation in the particle.

Overall, this design is not fully suitable for point-of-care diagnostics, however the project does highlight the potential for LDHM technology to be translated to point of care diagnosis, especially when paired with a computer vision software for automated image analysis.

For this project to be further developed in terms of suitability for point-of-care diagnostics, there are a few design features that would have to be amended or redesigned. The largest change would be the method of sample delivery to the sensor plane; microfluidics have many benefits over smear samples, such as larger sample throughput and potential to count and average data of the flow, however, the manual method of pumping sample used in the project is not compatible with at home use. As mentioned, a method would need to be implemented that achieves a regulated flow rate independent of a user. Further investigation into capillary based microfluidics may offer a solution to this issue, though will not offer as regulated flow control or the throughput offered by a sample reservoir, waste tank and syringe pump solution, however, a self contained microfluidic cartridge would be most appropriate for point-of-care diagnostics. Other amendments would be a more polished device structure, opting for single rigid structure over rather than a modular design, with alignment methods, such as aligning screws either being unnecessary or locked during the construction stage.

This project highlights the potential for LDHM based particle detection and analysis, albeit needing further development for clinical samples / purposes, with further potential development in all sections of the project (hardware, software, microfluidics). Overall the system described in this project is compact, lightweight and low cost and achieves milestones such as sizing and categorising manufactured “ideal” particles within a tolerance range and sizing of RBCs, though unfortunately falls short for more complex particles such as WBCs.

In comparison to competing technologies, the LDHM prototype shows great potential. The larger / variable FOV in conjunction with the CV based analysis allows for LDHM to image and analyse a larger sample plane than a haemocytometer, as well as the automation process being faster and less labour intensive than manual counting. The maximum FOV for this LDHM prototype is 18.29mm^2, far larger than a Haemocyctometer. With the sample plane being larger, a larger volume of sample can be analysed at once, which allows for the count to be more representative of the whole blood sample, as well as the potential for better averaging. However, the LDHM prototype requires a more precise sample preparation , in terms of the operational procedure and use of bespoke microfluidics as a form of sample delivery. The LDHM prototype, while designed to be as low complexity as possible, is still more complex than the haemocytometer; however the haemocytometer still requires a microscope to visualise the sample, whereas the LDHM prototype can function using any PC or laptop capable of running the python code, which is not overly intensive. When compared to other automatic devices, such as the Coulter Counter, is where this prototype begins to struggle. In theory, the main advantage of LDHM over Coulter Counters is the visualisation based differentiation, which yields more information about the sample such as internal structures, morphology, 3D positioning of particles within the sample. However this prototype requires further development for the identification of complex cells, as the method for differentiation struggles sizing WBCs and further use such as morphological analysis and identification of internal structures is yet to be explored. The LDHM device however is much less expensive to develop than the commercially available Coulter counters, such as the “Multisizer 4e”, as well as being far more compact and portable in comparison.

7.2 Limitation

7.2.1: Artificial Blood VS Biological Samples

While the justification for using non-biological, artificial, samples has been highlighted; the choice is not without limitations. With the software being developed using artificial blood as the sample, the relevant detection variables (i.e thresholds, size ranges, etc) are tuned to that of the microbeads opposed to blood cells. This means, while every effort has been made to generate an appropriately matched artificial blood, there is no guarantee that the same settings will be appropriate for both artificial and real samples; this may lead to misinterpreted cells, inflated or decreased counting / calculated concentration and overall unsuitable results.

Microbeads are visually uniform; being practically perfect spheres in shape and having no internal structures. This is in contrast to a real sample, where cells are , even within the same group,are not identical; with their shapes being non consistent , with different identifying structures and internal substructures. Therefore, the set-up proposed in this paper, while seeing some biological sample testing, has not experienced extensive testing on identifying particles based on complex structures.

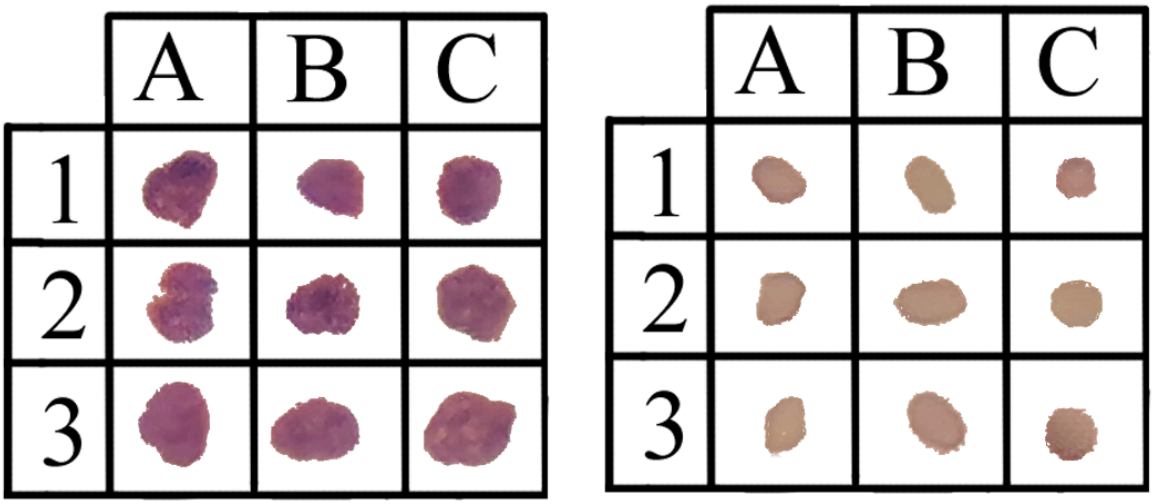

Figure 81: Compilation of WBC & RBC Shape

Figure 81, above, bove is a compilation of the various shapes of cells within the WBC and RBC groups digitally extracted from one sample imaged using traditional microscopy. Given cell shape is not perfect, variation in cell appearance is difficult to group, given a cell can vary in size, shape or both. Therefore the grids above approximately correspond so that rows 1-3 show increasing cell size, and groups A-C show “complex” shape, “flattened” shape, and “round” shape. This shape variation can cause sizing errors when utilising a horizontal-only line profile to determine size, as for a non-uniform cell, the size calculated is dependent on the orientation of the irregular cell.

As shown by reconstructions (Figure 69 & 79), internal structures (e.g. Cell Nuclei), can be observed using LDHM. In this image, the internal structure is shown as a dense, black particle within the cell. Given the software selects the line profile that has the point of lowest intensity (e.g. black) as the point that is most reconstructed, this may help identify WBCs internal structures; however, with cell shape being non-uniform, there is no guarantee that the internal structure will be intercepted by the line profile, meaning that the identification of WBCs is solely dependent on the sizing calculate rather than any internal morphological details.

To mediate this issue, further testing would need to be carried out, using clinical samples, to generate suitable settings, and perhaps alternative methods for identification. This may highlight design considerations that would need to change to become more suitable for clinical samples. These clinical samples would have to be varied to enable robust testing and validation, i.e varied concentrations of expected particulates and blood disorder related (particularly disorders that alter the regular shape of cells).

7.2.2: Computation intensity & information loss

Generating holographic interference patterns using a LDHM set-up is relatively simple to produce and can be displayed in real-time; generating comprehensible images is more complex. To reconstruct images from these holograms is computationally intensive, with the time taken to produce them being linked to the computing power of the device the set-up is linked to.

This potentially could make calculations by reconstruction an issue for a generic user with low grade / dated commercial technology; making investigation into non-reconstruction identification techniques useful. These methods, such as sizing, edge / contour identification, are less computationally complex to compute, making their functions more rapid, however, these result in information loss - as information such as substructures is unidentified / removed. This weakens the potential for complex blood analysis.

7.3 Future work

This project has potential to expand from this initial starting point, with many avenues for further research and development. With LDHM having many applications, the identified areas below will be project specific, surrounding the areas of testing, design and potential bloodwork applications.

7.3.1 Further Testing with Clinical Samples

Particle Concentrations & Haemoglobin Calculation:

Concentrations of cells within a sample would be useful information to extract; for blood analysis, a higher or lower concentration of RBCs or WBCs could be indicative of illness or disease. This would not be difficult to implement, provided the microfluidic channel is of a known volume , the sample is of a known dilution and the differentiation and count are accurate

Differentiation of leukocytes and analysis:

For further development of this project is required for identification, sizing and categorization of WBCs. With space to develop across all design features, there are multiple avenues that may lead to better quality images or software results. Being capable of a complete blood cell count would make this technology competitive with existing leading technologies, such as the Coulter Counter. The visualisation based analysis additionally gives potential for leukocytes differentiation to better map the cell populations within the sample.

Red Blood Cell Shape Analysis:

As shown by the clinical sample tests, the extractable morphological details the cells are limited with the current software. Indications of illnesses based on bloodwork is not limited to just the concentrations of red and white blood cells, but also cell shape; which is why increasing the quality of the reconstructed images, which is discussed further on, would make the function of the LDHM technology far more impactful. Poikilocytosis is the umbrella term for a large percentage of abnormal cell shape variations within a blood sample, indicating an underlying health issue - the most commonly known of these being sickle cell anaemia. Poikilocytosis is currently identified using blood smears, manually prepared and viewed by a medical professional using a traditional microscope . Further investigation into identifying and differentiating shaped cells using computer vision, may allow a simple set-up such as the one described in this dissertation, to automatically differentiate, count and classify anomalous cells in parallel to the standard counting and concentration calculations.

Name	Shape	Poikilocytosis Associated Conditions
Acanthocyte	Low density of thorn-like structures	Liver Dysfunction
Codocytes	“Target” like	Liver Disease, Iron deficiency
Echinocyte	High density of short spike-like structures	Uremia
Elliptocyte	Elliptical / Oval	Hereditary elliptocytosis

spherocytes	Spherical	Hemolytic anemias
Stomatocytes	Slit appearance	Hereditary / alcoholism
Drepanocytes	Sickle-like	Sickle Cell Anaemia
Dacrocye	Tear-drop appearance	bone marrow fibrosis

Table 3: Poikilocytosis information [62]

Table 3 ,above, is not an extensive list of all anomalous RBC variants, nor an exhaustive list of all associated conditions. However, this shows the value in analysing cell shape, as it can highlight a vast amount of potential health issues. [62]

7.3.2: Software Advancements

Reference Grid implementation:

Haemocytometer have an integrated reference grid, which is useful for referencing cell populations in certain regions of the image data as well as being an indicator for the cell size.

With the image captured having approximately unit magnification, assuming max resolution is utilised, the image captured will be the same size as the sensor, or the resolution multiplied by the physical pixel size, a virtual reference grid can be designed and applied.

Line profile rotation implementation:

With line profiles being drawn horizontally, there is a limitation in the accuracy of particle sizing when two particles are close to each other horizontally, where the line profile partially intersects the secondary particle.

Given the artificial sample using a large particle range 45µm-10µm, the line profile used had to be suitably larger than 45µm to capture the moment of reconstruction; potentially causing issues with smaller particles that are relatively close, this was resolved for clinical sample testing, utilising a smaller line profile length due to the focus on the WBC-RBC range, though there is still potential for this issue to arise.

The code below shows an example of identifying the line profile disturbance caused by a secondary particle.

From here, the line profile direction can be adjusted, in angular increments, for example defined here by 22.5 degree increments. These increments allow for 8 attempts at avoiding an adjoining particle. By decreasing the angle variable, more attempts can be made, however this increases the computational time of difficult particles, with extremely low angles potentially intersecting the sample secondary particle multiple times.

Machine Learning Based Computer Vision:

The software side of this project uses a standard approach to computer vision, which can be quite rigid in terms of predefined settings and sensitive to variations in contour size / shapes. A method that has been brought to attention has been the application of AI and Machine learning algorithms to help identify and differentiate particles, based on learning image sets. This could potentially aid in the identification of particles that have a complex 3D Shape or identifiable internal structures such as tilted red blood cells or WBC variants. This could potentially reduce the number of miscounted or misinterpreted particles.

Fresnel Reconstruction:

The Angular Spectrum Method used proved to be effective, however lacked morphological detail desired for full utilisation of the visual nature of LDHM technology for cell analysis. Angular Spectrum Method is not designed for near-field applications, which given the design parameters, the system design falls into this category. Rayleigh Method, as mentioned, is also not applicable, given the size of the scattering particles are not on the magnitude for rayleigh scattering to be the most appropriate model. Fresnel Reconstruction however is more applicable at near-field applications. [63]

Far-field distance, also called Fraunhofer distance, is defined by equation;

$Df = 2D^2 / \lambda$
Where;
D is aperture size
λ is wavelength

Inserting the system variables into this equation, 15μm aperture, 470 nm wavelength, a far-field distance can be calculated as 95.7cm - far higher than the propagation distance of Z2.

The Fresnel method models wavefronts as spherical and calculates diffraction patterns using this wave curvature. Though sounding complex, this process is less computationally intensive than the Angular Spectrum Method used.

With this in mind, the quality of the reconstruction may be improved by utilising a Fresnel based reconstruction method over Angular Spectrum method, which may further aid in improving the potential for Machine learning / Artificial intelligence based differentiation and/or morphological analysis.

Pixel Super Resolution Via Subject Shifting:

To further the potential for morphological analysis, a Pixel Super Resolution (PSR) method may have to be considered. PSR is achieved by numerous methods, such as light source shifting (where the light source is shifted, either using a source array or mechanically shifting source) or subject shifting (where the sample is shifted, either by microfluidic flow or mechanically shifted)[48]. In any method, the shifting component, by mechanical means or otherwise, produces unique interference patterns per shift step; these can be digitally combined to synthesise a higher resolution interference pattern, which in turn can be used to reconstruct a higher resolution image. This higher resolution image would be of increased quality, allowing for greater morphological analysis / particle differentiation using computer-vision, maintaining the non-invasive and label-free nature of LDHM while increasing the analysis capability.

With the design described within this project, there is the potential to implement PSR methods via sample shifting using the already existing microfluidic sample delivery. Utilising this method of PSR avoids redesign, which would be required to implement a light source array or mechanically shifting single light source, with the redesign focus being on the software element of the project there are no additional device hardware considerations or costs.

However, the microfluidic device flow would have to be better controlled, i.e. not user controlled, due to the subject-shift PSR method being sensitive to sample movement, as well as mechanical vibrations experienced by the device. An automated control method however may increase the overall cost and size of the device and when paired with additional vibration sensitivity may be unsuitable for at-home use.

7.3.3: Hardware Advancements

Laser & Driver:

One of the objectives for this project was to produce a low-cost yet effective system design, which influenced the decision to opt for LED over laser technology, due to the lower cost and lower power consumption, which in turn resulted in driving solutions that were also low complexity, low cost and low power consumption, making it suitable for being powered by a USB connection.

However, lasers do offer many advantages over LED technology in terms of coherence and spectral bandwidth. For example, the PLT3 450GB Laser Diode from ams OSRAM offers 450 nm Wavelength, with a 1 nm Spectral Bandwidth, though requires a typical forward voltage of 5.2 V and current of 87mA.

The driver method used in this project, while effective, would not be applicable for higher power devices such as lasers. The LM317 used results in a 2.6v to 3V drop - this accounts for the majority of the supply voltage from the 5V USB connection. However, if a boost converter is implemented prior to the driver stage, the voltage can be increased to accommodate both the higher voltage requirements of a laser, as well as the drop of the LM317.

Overall, the benefits in quality may be worth the additional cost and size; with the more complex circuitry, the optics would be more reliable as well as producing higher quality interference patterns.

Optical Fibre:

Optical fibre can be an advantageous design consideration for LDHM devices.

Fibre optics can be used to replace the pinhole component of the device; with the diameter of the optical fibre being comparable to a pinhole of equal diameter. This allows for smaller “pinholes” to be used while reducing the risk of blocking due to no physical opening. Theoretically, one of the benefits of the smaller diameter is the positive effects on image quality such as enhancing contrast, as supported by preliminary testing where the quality of the image increased with a smaller pinhole diameter.

High quality manufactured pinholes are expensive, in the context of the design in this project the pinhole accounted for approximately 39.4% of the device cost, costing £69.42 from the supplier “ThorLabs”. However, from the same supplier, single mode optical fibre, compatible with wavelengths 400-680nm, can be purchased for between £9.89 - £16.54 per metre (at time of writing). These fibres have a core of 3.0 μm and an approximate mode field diameter (light beam width propagating the fibre) of between 3.3 ± 0.5 μm at 405 nm and 4.6 ± 0.5 μm at 630 nm. Fibre specifications are product specific and may vary.

Using fibre optics, the sample could be illuminated at multiple small angles in a more compact system than possible with standard LEDs. A light source array would allow for the implementation of PSR reconstruction via light source shifting, which increases the quality of the image for greater resolution, detail extraction and potential for greater morphological analysis. Though, as mentioned, there are alternative PSR methods, which can utilise existing design features, such as microfluidic-based sample shifting.

Though it should be noted that implementation of fibre optics also has its challenges, such as design complexity. The increased number of design elements such as fibre coupled LEDs/Lasers may increase the physical size of the device, as well as increase the power consumption beyond USB power output capability for light source array designs. With increased size, components and energy usage comes increased overall cost, which may or may not outweigh the benefits, though going this route makes the resultant device less suitable for point-of-care diagnostics.

7.3.4: Microfluidic Advancements

Capillary Loaded Microfluidic Device:

As mentioned, user controlled microfluidic loading is unsuitable for point-of-care diagnostics, as the unregulated flow can cause various errors both of the data collected as well as increase the risk of bursting microfluidics due to incorrect pressure being applied.

Therefore a capillary based approach may be applicable. Capillary loading, while not keeping the pressure / flow constant, will reduce the risk of pressure-related microfluidic failure as well as generating a more constant flow between users than a syringe method, though ultimately is still an unregulated flow option. Depending on the imaging style desired, flow may not be required as opposed to just populating the sample plane over the sensor. This style of loading is more appropriate for at-home users, with most users becoming accustomed to at-home microfluidic testing kits over the course of the COVID-19 pandemic, where this sample handling method by untrained individuals was relatively effective. A fully enclosed cartridge, without an external waste tank as used in this project, allows for easy disposal of contaminated microfluidic devices, reducing risk of contaminating other surfaces or the device itself.

However, as mentioned the limited control of flow also limits the sensing style of the device, focusing on just the population over the sensor rather than averaging count over flow, which may decrease accuracy. There is also the potential due for anomalous data, such as those caused by cell aggregation, to have a greater effect, especially as uniform sample spread is hard to achieve in wide channelled (to cover entire sensor FOV) microfluidic devices.

Pump loaded Microfluidic Device:

While less appropriate for at-home use, a pump loaded system would offer far superior flow regulation, allowing for a higher throughput device while maintaining a consistent sample difference (via flow progression) for averaging.
Pumping mechanisms however, would be complex to integrate into the device (to avoid reliance on separate equipment), which would increase device size and cost. This style of sample loading would be most applicable to professional settings, with potential to be used in local, smaller clinics opposed to a larger organisation such as a hospital. The level of throughput would likely be unnecessary in a home setting, and when combined with the complexity and added cost for a consumer, would also likely be economically unviable.

8: Conclusions

Reflecting on the project goals stated at the beginning of thesis;

Within “Design Experiments and Considerations” (Section 3), the parameters of an LDHM set-up were thoroughly investigated, with the chosen metric for quality being contrast for ease of contour / edge detection in computer vision applications. Using the data from these preliminary experiments, a final prototype was designed to generate high quality, digital holographic images, with consideration to factors such as cost, size, simplicity and weight. This design was overall effective at producing holographic images, of artificial and biological samples, allowing for a large potential FOV (if maximum sensor height is used, then the FOV is approximately equal to 4.277mm squared) being able to image particles as small as 5μm (as calculated for RBC), as well as internal structures of WBCs to be observable albeit not well resolved.

A supporting software, with the purpose of holographic image collection, reconstruction, particle identification, particle sizing and contamination handling was designed. This software utilised OpenCV based image processing, coupled with a reconstruction method based on the PyLDHM library, background-subject subtraction with denoising methods, contour detection / fill / find centre methods, and line profile based particle sizing. The software developed was crucial to the later testing stages of the device and experiments with artificial and biological samples. The software designed functioned appropriately for ideal particles, such as the manufactured sphericals used in the artificial sample, however had mixed success with biological samples, with RBCs being sized and categorised appropriately, while attempts at sizing and categorising WBCs automatically were unsuccessful despite the reconstruction of both cells being a success..

The sample delivery system took the form of a bespoke, glass microfluidic device. This microfluidic device was compatible with the LDHM device, with a slot in the device casing / sample chamber that allowed the microfluidic to be inserted while allowing the I/O syringe ports to be accessed while shielding the sample chamber from ambient light.
The material cost of this device was low, being based on readily available materials such as microscope slides and coverslips, as well as 3D-printed I/O ports. This allowed for a design that was transparent (compatible with in-line holographic / traditional microscopy), lightweight and portable.
While the device is low complexity - i.e a simple channel - the method of loading makes this system inappropriate for at-home use; due to the method of loading being unregulated, and the potential hazards associated with waste collection.

The software was used in multiple experiments that used artificial and biological samples, with mixed success across all software features.
For both artificial and biological samples, the software handled the detection of particles well, provided certain conditions were met, such as a relatively uniform background, low particle aggregation, and unshifted perspective between the background and subject images.
Differentiation, based on sizing, was a mixed success. Using the more uniform artificial sample, the sizing was ,within a degree of tolerance, quite accurate, and based on this sizing, the software successfully categorised particles correctly for their calculated size. However, with the biological sample, the automated differentiation method was mostly unsuccessful, while RBCs were mostly correctly sized and categorised, WBCs rarely calculated as the correct size, with most sizing errors calculating WBCs as RBCs. Consequently, the count for the artificial sample was accurately calculated, while the biological count was approximately equal to the total cell count.
Overall , the accuracy for the artificial samples was far superior to that of the biological samples, this reduced accuracy is attributed to the more complex shape and structure of biological cells compared to manufactured

particles . The device and software in this project requires further development to be translated into a clinically functional device, however, the technology shows promise, with multiple milestones being achieved while remaining low-cost, compact and lightweight.

9: References

[1] A. A. Fryer and W. S. Smellie, “Managing demand for laboratory tests: A laboratory toolkit,” *Journal of Clinical Pathology*, vol. 66, no. 1, pp. 62–72, 2012. doi:10.1136/jclinpath-2011-200524

[2] NHS England, “Digital First: Clinical Transformation through Pathology Innovation.” May. 11, 2017 (src: https://www.england.nhs.uk/wp-content/uploads/2014/02/pathol-dig-first.pdf)

[3] “What is pathology?,” The Royal College of Pathologists, https://www.rcpath.org/discover-pathology/what-is-pathology.html#:~:text=Pathology%20is%20the%20study%20of,experts%20in%20illness%20and%20disease. (accessed Dec. 20, 2023).

[4] NHS England, “Service improvement in blood sciences.” Jan. 2013 (Src: https://www.slideshare.net/NHSImprovement/service-improvement-in-blood-sciences)

[5] M. L. Verso, “THE EVOLUTION OF BLOOD-COUNTING TECHNIQUES,” *Medical History*, vol. 8, no. 2, pp. 149–158, Aug. 2012. doi:https://doi.org/10.1017/S0025727300029392

[6] B. J. Bain, *Blood Cells: A Practical Guide*, 5th Edition. Gower Medical Publishings, 2015.

[7] J. Nunez *et al.*, “Low Lymphocyte Count and Cardiovascular Diseases ,” *Current Medicinal Chemistry*, vol. 18, no. 21, May 2011. doi:10.2174/092986711796391633

[8] P. P. Chmielewski and B. Strzelec, “Elevated leukocyte count as a harbinger of systemic inflammation, disease progression, and poor prognosis: a review,” *Folia Morphologica*, vol. 77, no. 2, Oct. 2017. doi:10.5603/FM.a2017.0101

[9] J. L. Kujovich, “Evaluation of Anemia,” *Obstetrics and Gynecology Clinics of North America*, vol. 43, no. 2, pp. 247–264, Mar. 2016. doi:10.1016/j.ogc.2016.01.009

[10] U. P. Moravapalle, A. Deshpande, A. Kapoor, R. Ramjee, and P. Ravi, “Blood Count on a Smartphone Microscope: Challenges,” *HotMobile ’17: Proceedings of the 18th International Workshop on Mobile Computing Systems and Applications*, pp. 37–42, Feb. 2017. doi:10.1145/3032970.3032986

[11]N. J. Brendish et al., “Clinical impact of molecular point-of-care testing for suspected COVID-19 in hospital (COV-19POC): a prospective, interventional, non-randomised, controlled study,” The Lancet Respiratory Medicine, vol. 8, issue 12, Oct. 2020, doi: https://doi.org/10.1016/S2213-2600(20)30454-9.

[12] R. Paschotta (2008). optical intensity. *RP Photonics Encyclopedia*. doi:https://doi.org/10.61835/tro.

[13] R. Paschotta (2008). optical intensity. *RP Photonics Encyclopedia*. doi:https://doi.org/10.61835/wdl.

[14] R. Paschotta (2008). optical intensity. *RP Photonics Encyclopedia*. doi:https://doi.org/10.61835/vke.

[15]Lahiri M, Wolf E. Change in spatial coherence of light on refraction and on reflection. J Opt Soc Am A Opt Image Sci Vis. 2013 Jun 1;30(6):1107-12. doi: 10.1364/JOSAA.30.001107. PMID: 24323097

[16] Nikolic, D. and Nesic, L. (2011). Verification of the uncertainty principle by using diffraction of light waves. European Journal of Physics, 32(2), pp.467–477. doi:https://doi.org/10.1088/0143-0807/32/2/018.

[17] Young, T. (1804). I. The Bakerian Lecture. Experiments and calculations relative to physical optics. *Philosophical Transactions of the Royal Society of London*, 94, pp.1–16. doi:https://doi.org/10.1098/rstl.1804.0001.

[18] Barnhart, S. and Gunasekaran, S. (2020). Design and Development of a Coherent Detection Rayleigh Doppler Lidar System for Use as an Alternative Velocimetry Technique in Wind Tunnels. [online] Available at: https://www.researchgate.net/publication/343770420_Design_and_Development_of_a_Coherent_Detection_Rayleigh_Doppler_Lidar_System_for_Use_as_an_Alternative_Velocimetry_Technique_in_Wind_Tunnels [Accessed 26 Dec. 2023].

[19] R. Paschotta (2008). optical intensity. *RP Photonics Encyclopedia*. doi:https://doi.org/10.61835/p2i

[20] Acharya, R. (2017). Mie Scattering Theory - an overview . [online] www.sciencedirect.com. Available at: https://www.sciencedirect.com/topics/engineering/mie-scattering-theory.

[21] GABOR, D. (1948). A New Microscopic Principle. Nature, 161(4098), pp.777–778. doi:https://doi.org/10.1038/161777a0.

[22] Oe, K. and Nomura, T. (2018). Twin-image reduction method using a diffuser for phase imaging in-line digital holography. Applied Optics, 57(20), p.5652. doi:https://doi.org/10.1364/ao.57.005652.

[23] Leith, E.N. and Upatnieks, J. (1962). Reconstructed Wavefronts and Communication Theory*. Journal of the Optical Society of America, 52(10), p.1123. doi:https://doi.org/10.1364/josa.52.001123.

[24] Matišák, J., Rábek, M. and Žáková, K. (2019). Use of Holographic Technology in Online Experimentation. Proceedings of the 2019 Federated Conference on Computer Science and Information Systems. doi:https://doi.org/10.15439/2019f179.

[25] Huang, S.-Y., Arvind Mukundan, Tsao, Y.-M., Kim, Y., Lin, F.-C. and Wang, H.-C. (2022). Recent Advances in Counterfeit Art, Document, Photo, Hologram, and Currency Detection Using Hyperspectral Imaging. 22(19), pp.7308–7308. doi:https://doi.org/10.3390/s22197308.

[26] Ostrovsky, Y.I., M.M. Butusov and Ostrovskaya, G.V. (2013). Interferometry by Holography. Springer.

[27] H. John Caulfield (2003). Holography and optical computing: the ongoing entanglement. Proceedings of SPIE. doi:https://doi.org/10.1117/12.478428.

[28] Ozcan, A. and McLeod, E. (2016). Lensless Imaging and Sensing. Annual Review of Biomedical Engineering, 18(1), pp.77–102. doi:https://doi.org/10.1146/annurev-bioeng-092515-010849.

[30] Moschandreou, T.E. (2012b). Blood Cell - An Overview of Studies in Hematology. InTech eBooks. InTech. doi:https://doi.org/10.5772/2979.

[31] Puddu, P.E., Lanti, M., Menotti, A., Mancini, M., Zanchetti, A., Cirillo, M., Angeletti, M. and Gubbio Study Research Group (2002). Red blood cell count in short-term prediction of cardiovascular disease incidence in the Gubbio population study. Acta Cardiologica, [online] 57(3), pp.177–185. doi:https://doi.org/10.2143/AC.57.3.2005387.

[32] Nersesjan, V., Zervides, K.A., Sørensen, A.L., Kjaer, L., Skov, V. and Hasselbalch, H.C. (2020). The red blood cell count and the erythrocyte sedimentation rate in the diagnosis of polycythaemia vera. European Journal of Haematology, [online] 104(1), pp.46–54. doi:https://doi.org/10.1111/ejh.13334.

[33] van Es, N., Sturk, A., Middeldorp, S. and Nieuwland, R. (2014). Effects of cancer on platelets. Seminars in Oncology, [online] 41(3), pp.311–318. doi:https://doi.org/10.1053/j.seminoncol.2014.04.015.

[34]Boilard, E., Blanco, P. and Nigrovic, P.A. (2012). Platelets: active players in the pathogenesis of arthritis and SLE. Nature Reviews Rheumatology, 8(9), pp.534–542. doi:https://doi.org/10.1038/nrrheum.2012.118.

[35] Krishnegowda, M. and Rajashekaraiah, V. (2015). Platelet disorders. Blood Coagulation & Fibrinolysis, 26(5), pp.479–491. doi:https://doi.org/10.1097/01.mbc.0000469521.23628.2d.

[36] Clarke, W.L., Cox, D., Gonder-Frederick, L.A., Carter, W. and Pohl, S.L. (1987). Evaluating Clinical Accuracy of Systems for Self-Monitoring of Blood Glucose. Diabetes Care, 10(5), pp.622–628. doi:https://doi.org/10.2337/diacare.10.5.622.

[37] Han, Y., Yu, Z., Wen, S., Zhang, B., Cao, X. and Wang, X. (2011). Prognostic value of chemotherapy-induced neutropenia in early-stage breast cancer. Breast Cancer Research and Treatment, 131(2), pp.483–490. doi:https://doi.org/10.1007/s10549-011-1799-1.

[38] Federici, M., Hribal, M., Perego, L., Ranalli, M., Caradonna, Z., Perego, C., Usellini, L., Nano, R., Bonini, P., Bertuzzi, F., Marlier, L.N., Davalli, A.M., Carandente, O., Pontiroli, A.E., Melino, G., Marchetti, P., Lauro, R., Sesti, G. and Folli, F. (2001). High glucose causes apoptosis in cultured human pancreatic islets of Langerhans: a potential role for regulation of specific Bcl family genes toward an apoptotic cell death program. Diabetes, [online] 50(6), pp.1290–1301. doi:https://doi.org/10.2337/diabetes.50.6.1290.

[39] Daniels, G. (2021). An overview of blood group genotyping. Annals of Blood, 0. doi:https://doi.org/10.21037/aob-21-37.

[40]Jambroes, M., Nederland, T., Kaljouw, M., van Vliet, K., Essink-Bot, M.-L. and Ruwaard, D. (2015). Implications of health as ‘the ability to adapt and self-manage’ for public health policy: a qualitative study. The European Journal of Public Health, [online] 26(3), pp.412–416. doi:https://doi.org/10.1093/eurpub/ckv206.

[41] www.freestyle.abbott. (n.d.). Freestyle Libre 2 - FreeStyle Libre | Abbott. [online] Available at: https://www.freestyle.abbott/uk-en/products/freestyle-libre-2.html [Accessed 27 Dec. 2023].

[42] Abcam (2019). Counting cells using a hemocytometer | Abcam. [online] Abcam.com. Available at: https://www.abcam.com/protocols/counting-cells-using-a-haemocytometer.

[43] AKKOYUN, F. and ÖZÇELİK, A. (2021). Rapid Characterization of Cell and Bacteria Counts using Computer Vision. Türk Doğa ve Fen Dergisi. doi:https://doi.org/10.46810/tdfd.902441.

[44] Graham, M.Don. (2021). The Coulter Principle: A history. Cytometry Part A, 101(1), pp.8–11. doi:https://doi.org/10.1002/cyto.a.24505.

[45] Nguyen, J., Wei, Y., Zheng, Y., Wang, C. and Sun, Y. (2015). On-chip sample preparation for complete blood count from raw blood. Lab on a Chip, 15(6), pp.1533–1544. doi:https://doi.org/10.1039/c4lc01251h.

[46] EDMUNDSON, I.C. (1966). Coincidence Error in Coulter Counter Particle Size Analysis. Nature, 212(5069), pp.1450–1452. doi:https://doi.org/10.1038/2121450b0.

[47] www.beckman.com. (n.d.). Cellular Analysis using the Coulter Principle: Measurement with Great Accuracy and Speed - Beckman Coulter. [online] Available at: https://www.beckman.com/resources/reading-material/application-notes/cellular-analysis-using-the-coulter-principle.

[48] Wu, Y. and Ozcan, A. (2018). Lensless digital holographic microscopy and its applications in biomedicine and environmental monitoring. Methods, 136, pp.4–16. doi:https://doi.org/10.1016/j.ymeth.2017.08.013.

[50] Zhang, J., Sun, J., Chen, Q. and Zuo, C. (2020). Resolution Analysis in a Lens-Free On-Chip Digital Holographic Microscope. IEEE transactions on computational imaging, 6, pp.697–710. doi:https://doi.org/10.1109/tci.2020.2964247.

[51] Littwiller, D. (2001). CCD vs. CMOS: PHOTONICS SPECTRA.

[52] Linear Systems, Fourier Transforms, and Optics (Wiley Series in Pure and Applied Optics) Jack D. Gaskill

[53]Seo, S., Su, T.-W., Tseng, D.K., Erlinger, A. and Ozcan, A. (2009). Lensfree holographic imaging for on-chip cytometry and diagnostics. Lab Chip, 9(6), pp.777–787. doi:https://doi.org/10.1039/b813943a.

[54] Ozcan, A., Isikman, S.O., Ikbal Sencan, Onur Mudanyali, Su, T.-W., Bishara, W. and Erlinger, A. (2010). High-Throughput Lens-Free Blood Analysis on a Chip. Analytical Chemistry, [online] 82(11), pp.4621–4627. doi:https://doi.org/10.1021/ac1007915.

[55]Bryan, A.K., Engler, A., Gulati, A. and Manalis, S.R. (2012). Continuous and Long-Term Volume Measurements with a Commercial Coulter Counter. PLoS ONE, 7(1), p.e29866. doi:https://doi.org/10.1371/journal.pone.0029866.

[56] Moon, S., Keles, H.O., Ozcan, A., Khademhosseini, A., Haeggstrom, E., Kuritzkes, D. and Demirci, U. (2009). Integrating microfluidics and lensless imaging for point-of-care testing. Biosensors & Bioelectronics, [online] 24(11), pp.3208–3214. doi:https://doi.org/10.1016/j.bios.2009.03.037.

[57] www.beckman.com. (n.d.). Multisizer 4e Coulter Counter. [online] Available at: https://www.beckman.com/cell-counters-and-analyzers/multisizer-4e [Accessed 27 Dec. 2023].

[58] Raúl Fernando Guerrero-Castañeda, Trujillo, C. and Doblas, A. (2022). pyDHM: A Python library for applications in digital holographic microscopy. PLOS ONE, 17(10), pp.e0275818–e0275818. doi:https://doi.org/10.1371/journal.pone.0275818.

[59] Diez-Silva, M., Dao, M., Han, J., Lim, C.-T. and Suresh, S. (2010). Shape and Biomechanical Characteristics of Human Red Blood Cells in Health and Disease. MRS bulletin, [online] 35(5), pp.382–388. doi:https://doi.org/10.1557/mrs2010.571.

[60] M, U. (n.d.). Red blood cell diameter - Rat Rattus norvegicus - BNID 102928. [online] bionumbers.hms.harvard.edu. Available at: https://bionumbers.hms.harvard.edu/bionumber.aspx?s=n&v=1&id=102928.

[61] Tigner, A., Ibrahim, S.A. and Murray, I. (2022). Histology, White Blood Cell. [online] PubMed. Available at: https://www.ncbi.nlm.nih.gov/books/NBK563148/.

[62] Bandaru, S.S. and Gupta, V. (2020). Poikilocytosis. [online] PubMed. Available at: https://www.ncbi.nlm.nih.gov/books/NBK562141/.

[63] Goodman, J.W. (1968). Introduction to Fourier optics. New York: Mcgraw-Hill.

10: Appendix

10.1: LDHM Computer Vision Software

```python
import cv2
import numpy as np
import math
import os
import matplotlib.pyplot as plt
from PIL import Image
from scipy.interpolate import interp1d

def projectBanner(integer):
    print("")
    if integer == 0:
        print(
            "╔==========================|OWEN KNIGHTLEY"
            " LONG|==============================╗")
        print(
            "‖ Computer Vision For Lensless Digital Holographic Microscopy Particle Counting ‖")
        print(
            "╚======================================="
            "=======================================╝")
        print(" ")
    else:
        return None
```

```python

def titleBanner(string, boolean):
    message = string
    size = len(string)
    i = 0
    bannerTop = ""
    bannerBottom = ""
    while i < size:
        if i == 0:
            bannerTop = bannerTop + "╔="
            bannerBottom = bannerBottom + "╚="
        elif i == size - 1:
            bannerTop = bannerTop + "=╗"
            bannerBottom = bannerBottom + "=╝"
```

```python
        else:
            bannerTop = bannerTop + "="
            bannerBottom = bannerBottom + "="
        i = i + 1
    #print("")
    if boolean:
        print("")
        print(bannerTop)
        print('‖' + message + '‖')
        print(bannerBottom)
    else:
        print(message)
```

```
def instructionSet(integer):
    if integer == 0:
        print("A User-specific file path is required for image data storage")
        print("...Please Create a folder and insert its path here....")
    elif integer == 1:
        print(" ")
        print("*It is recommended that the folder chosen as filepath is open and visible")
        print("*Click on the Live video window that has opened; this has been resized to fit on the screen")
        print("*Insert the microfluidic device into the LDHM device slot and ensure than it remains still")
        print("*Insert buffer fluid into the microfluidic channel until the channel is filled")
        print(
            "*Press the 'b' key when you are ready to take"
            " a background image; this should appear in your folder")

    elif integer == 2:
        print(" ")
        print("*After the background has been captured; introduce the sample to the microfluidic channel")
        print("*It is important to start subject capture "
              "only after the sample front has flowed to the end of the microfluidic")
        print("*Press and hold the 's' key when you are "
              "ready to take a subject image; this should appear in your folder")
    elif integer == 3:
        print(" ")
        print("...Please view your captured images...")
    else:
        return None
```

```
def find_threshold_crossings(profile, threshold):
    crossings = []
    profile = profile.astype(np.int32)  # Convert to int32 data type
    center_index = len(profile) // 2  # Find the center index of the profile

    # Initialize variables to store the crossings on either side of the center
    left_crossing = None
    right_crossing = None

    for i in range(center_index - 1, 0, -1):
        if (profile[i] < threshold and profile[i + 1] >= threshold) \
                or (profile[i] >= threshold and profile[i + 1] < threshold):
            # Linear interpolation to find the exact position of the crossing
            slope = (profile[i + 1] - profile[i])
            if slope != 0:
                x = i + (threshold - profile[i]) / slope
                left_crossing = x
            break  # Break when the first left crossing is found
```

```

    for i in range(center_index, len(profile) - 1):
        if (profile[i] < threshold and profile[i + 1] >= threshold) \
                or (profile[i] >= threshold and profile[i + 1] < threshold):
            # Linear interpolation to find the exact position of the crossing
            slope = (profile[i + 1] - profile[i])
            if slope != 0:
                x = i + (threshold - profile[i]) / slope
                right_crossing = x
            break  # Break when the first right crossing is found

    # Append the left and right crossings to the list
    if left_crossing is not None:
        crossings.append(left_crossing)
    if right_crossing is not None:
        crossings.append(right_crossing)

    return crossings

```

```python
def subtractionDespeckle(background_path, subject_path):
    # Read the background and subject images
    background = cv2.imread(background_path, cv2.IMREAD_GRAYSCALE)
    subject = cv2.imread(subject_path, cv2.IMREAD_GRAYSCALE)

    if background is None:
        print(f"Error: Could not read the background image at '{background_path}'")
        return

    if subject is None:
        print(f"Error: Could not read the subject image at '{subject_path}'")
        return

    # Convert the images to NumPy arrays
    background_array = np.array(background)
    subject_array = np.array(subject)

    # Subtract the subject image from the background to get the original image
    original_image = background_array - subject_array

    # Invert the image for erosion and dilation
    inverted_image = cv2.bitwise_not(original_image)
```

```python

    # Perform erosion and dilation to remove small speckles
    #kernel1_1 = np.ones((1, 1), np.uint8)
    kernel3_3 = np.ones((3, 3), np.uint8)
    inverted_eroded = cv2.erode(inverted_image, kernel3_3, iterations=2)
    inverted_dilated = cv2.dilate(inverted_eroded, kernel3_3, iterations=2)

    # Apply Gaussian blur to the inverted dilated image
    blurred_image = cv2.GaussianBlur(inverted_dilated, (9, 9), 0)

    # Invert back the blurred image
    dilated = cv2.bitwise_not(blurred_image)

    # Contour Fill
    lower = 0
    upper = 100
    thresh = cv2.inRange(dilated, lower, upper)
    threshinvert = 255 - thresh

    des = cv2.bitwise_not(threshinvert)  # threshinvert
    contour, hier = cv2.findContours(des, cv2.RETR_CCOMP, cv2.CHAIN_APPROX_SIMPLE)

    for cnt in contour:
        cv2.drawContours(des, [cnt], 0, 255, -1)
```

```python

    invertedfill = cv2.bitwise_not(des)
    #cv2.imshow("Contour Fill", invertedfill)
    # Save the image subtraction as "temp_subtraction.tiff"
    # cv2.imwrite("temp_subtraction.tiff", original_image)
    Reinvertedfill = 255 - invertedfill
    Output_eroded = cv2.erode(Reinvertedfill, kernel3_3, iterations=1)
    inverted_dilated = cv2.dilate(Output_eroded, kernel3_3, iterations=1)
    #cv2.imshow("Contour Fill_ Eroded/Dilated", inverted_dilated)
    FinalOutput = 255 - inverted_dilated
    #cv2.imshow("Background", background)
    #cv2.imshow("Subject", subject)
    #cv2.imshow("Particle Detection", FinalOutput)
    #cv2.waitKey(0)
    # Display the images side by side
    stacked_images = np.hstack((background, subject, original_image, FinalOutput))
    #cv2.imshow("Background - Subject - Subtraction - Output", stacked_images)
    #cv2.waitKey(0)
    cv2.destroyAllWindows()
```

```
    # Save the FinalOutput from the Despeckle function
    #final_output_filename = os.path.join(file_path, 'LDHM_ParticleDetection.tiff')
    #cv2.imwrite(final_output_filename, FinalOutput)
    #print(f"Final Output saved as {final_output_filename}")

    # Return the particle detection image
    return FinalOutput
```

```
def imageRead(namefile):
    # Function to load image using PIL
    loadImage = Image.open(namefile).convert('L')
    return loadImage
```

```
def angularSpectrum(field, z, wavelength, dx, dy):
    '''
    Function to diffract a complex field using the angular spectrum approximation
    Inputs:
    field - complex field
    z - propagation distance
    wavelength - wavelength
    dx,dy - sampling pitches
    '''

    field = np.array(field)
    M, N = field.shape
    x = np.arange(0, N, 1)
    y = np.arange(0, M, 1)
    X, Y = np.meshgrid(x - (N / 2), y - (M / 2), indexing='xy')

    dfx = 1 / (dx * M)
    dfy = 1 / (dy * N)

    field_spec = np.fft.fftshift(np.fft.fft2(np.fft.fftshift(field)))
    phase = np.exp(
        1j * z * 2 * math.pi * np.sqrt(np.power(1 / wavelength, 2) - (np.power(X * dfx, 2) + np.power(Y * dfy, 2))))

    tmp = field_spec * phase

    out = np.fft.ifftshift(np.fft.ifft2(np.fft.ifftshift(tmp)))

    return out
```

```
def intensity(inp, log=False):
    out = np.abs(inp)
    if log:
        out = 20 * np.log(out)
        out[out == np.inf] = 0
        out[out == -np.inf] = 0

    return out
```

```
def extract_horizontal_line_profile(image, center_x, center_y, line_length):
    h, w = image.shape[:2]
    if center_y >= h or center_x >= w:
        return None
    start_x = max(center_x - line_length // 2, 0)
    end_x = min(center_x + line_length // 2, w - 1)

    # Change the line length here to take profiles 2 pixels higher
    line_profile = image[center_y - 2, start_x:end_x + 1]

    return line_profile
```

```python
def find_centers(image, min_contour_area=150, max_contour_area=500):
    # Find contours in the binary image
    contours, _ = cv2.findContours(image, cv2.RETR_EXTERNAL, cv2.CHAIN_APPROX_SIMPLE)

    BGRimage = cv2.cvtColor(image, cv2.COLOR_GRAY2BGR)
    particles_centers = []  # List to store particle centers
    particles_tags = []  # List to store particle tags
    fragments = 0
    particles = 0
    obstructions = 0

    for idx, contour in enumerate(contours):
        # Calculate the center of each contour if the contour area is greater than zero
        M = cv2.moments(contour)
        if M["m00"] > 0:
            center_x = int(M["m10"] / M["m00"])
            center_y = int(M["m01"] / M["m00"])
        else:
            center_x, center_y = 0, 0

        contour_area = cv2.contourArea(contour)
```

```python

        # Draw a small circle at the center of the contour and add a tag
        tag = ""
        color = None
        if contour_area >= min_contour_area and contour_area < max_contour_area:
            color = (0, 0, 255)  # Red color for particles
            cv2.circle(BGRimage, (center_x, center_y), 5, color, -1)
            particles += 1
            tag = f'P{particles}'
        elif contour_area >= max_contour_area:
            color = (255, 0, 0)  # Blue color for obstructions
            cv2.circle(BGRimage, (center_x, center_y), 5, color, -1)
            obstructions += 1
            tag = f'O{obstructions}'
        else:
            color = (0, 255, 0)  # Green color for fragments
            cv2.circle(BGRimage, (center_x, center_y), 1, color, -1)
            fragments += 1
            tag = f'F{fragments}'

        # Get the dot color and use it for the tag text
        dot_color = tuple(color)
        cv2.putText(BGRimage, tag, (center_x + 10, center_y + 10), cv2.FONT_HERSHEY_SIMPLEX, 0.5, dot_color, 1)
```

```
        # Store particle centers and tags separately in their respective lists
        if contour_area >= min_contour_area and contour_area < max_contour_area:
            particles_centers.append((center_x, center_y))
            particles_tags.append(tag)
    return particles_centers, particles_tags, BGRimage, fragments, particles, obstructions

# Function to add center highlight to the image
def add_center_highlight(image, center_x, center_y, radius=1, color=(0, 0, 255), thickness=1):
    cv2.circle(image, (center_x, center_y), radius, color, thickness)

def find_particle_category(particle_size):
    # Define the size ranges for each category
    size_categories = {
        "UnderBounds": (0, 0),
        "RBC": (2, 8.9999),
        "WBC": (9, 15),
        "OverBounds": (15.0000001, 10000000)
    }

    # Check the size of the particle and categorize it into the appropriate category
    for category, size_range in size_categories.items():
        if size_range[0] <= particle_size <= size_range[1]:
            return category

    # If the particle size doesn't match any category, return None
    return None
```

```

def calculate_particle_size(threshold_crossings, sensor_pixel_um):
    if len(threshold_crossings) >= 2:
        total_length_below_threshold = threshold_crossings[-1] - threshold_crossings[0]
    else:
        total_length_below_threshold = 0

    particle_size = total_length_below_threshold * sensor_pixel_um
    return particle_size
```

```

# Project Banner
projectBanner(0)

pathPass = 0
while pathPass == 0:
    instructionSet(0)
    file_path = input("Enter the file path of your folder: ")  # input path
    titleBanner("File path is reachable", True)
    if os.path.exists(file_path):  # Test if path is real
        pathPass = 1
    else:
        titleBanner("ERROR: File path is unreachable", True)
```

```

# Video Capture Code
deviceCamera = cv2.VideoCapture(0, cv2.CAP_DSHOW)  # '0' indicates default camera, '1' secondary (LDHM Device)
deviceCamera.set(cv2.CAP_PROP_FRAME_WIDTH, 2592)  # Resolution X
deviceCamera.set(cv2.CAP_PROP_FRAME_HEIGHT, 1944)  # Resolution Y

# Get the camera's native resolution
width = int(deviceCamera.get(cv2.CAP_PROP_FRAME_WIDTH))
height = int(deviceCamera.get(cv2.CAP_PROP_FRAME_HEIGHT))
imageXY = 640  # Change this to your desired size

# Calculate the crop coordinates to get a 640x640 square in the center
crop_x = (width - imageXY) // 2
crop_y = (height - imageXY) // 2
```

```
350
351 backgroundTaken = 0
352 subjectTaken = 0
353 confirmation = 0
354 imageConfirmation = ""
355
356 instructionSet(1)
357 while backgroundTaken & subjectTaken != 1:
358     success, frame = deviceCamera.read()
359
360     # Crop the frame to 640x640 centered
361     cropped_frame = frame[crop_y:crop_y + imageXY, crop_x:crop_x + imageXY]
362
363     # Resize the cropped frame to imageXY before saving
364     cropped_frame = cv2.resize(cropped_frame, (imageXY, imageXY))
365
366     cv2.imshow("Live LDHM Video", cropped_frame)
367
368     if cv2.waitKey(1) & 0xFF == ord('b'):  # button press for background image capture
369         if backgroundTaken == 0:
370             cv2.imwrite(os.path.join(file_path, 'LDHM_Raw' + "_Background" + '.tiff'), cropped_frame)
371             background_image_path = os.path.join(file_path, 'LDHM_Raw' + "_Background" + '.tiff')
372             backgroundTaken = 1
373             titleBanner("Background Image Taken", True)
374             instructionSet(2)
375
```

```
376     if cv2.waitKey(1) & 0xFF == ord('s'):  # button press for subject image capture
377         if subjectTaken == 0:
378             cv2.imwrite(os.path.join(file_path, 'LDHM_Raw' + "_Subject" + '.tiff'), cropped_frame)
379             subject_image_path = os.path.join(file_path, 'LDHM_Raw' + "_Subject" + '.tiff')
380             subjectTaken = 1
381             titleBanner("Subject Image Taken", True)
382
383     if backgroundTaken == 1 & subjectTaken == 1:
384         instructionSet(3)
385         while confirmation != 1:
386             print(" ")
387             imageConfirmation = input("Do you want to use the images captured? (yes/no): ")
388             if imageConfirmation == "yes":
389                 confirmation = 1
390             elif imageConfirmation == "no":
391                 confirmation = 0
392                 backgroundTaken = 0
393                 subjectTaken = 0
394                 titleBanner("Please Retake Images", True)
395             else:
396                 titleBanner("ERROR: type yes or no", True)
397                 confirmation = 0
398                 # Handle the case where the user entered "no" or anything other than "yes"
399
```

```
if backgroundTaken == 1 & subjectTaken == 1:

    # Image subtraction
    background_image_path = os.path.join(file_path, 'LDHM_Raw' + "_Background" + '.tiff')
    subject_image_path = os.path.join(file_path, 'LDHM_Raw' + "_Subject" + '.tiff')
    subtraction_Image = subtractionDespeckle(background_image_path, subject_image_path)
    flipSubtraction = 255 - subtraction_Image

    particles_centers, particles_tags, highlighted_image,\
    fragments, particles, obstructions = find_centers(flipSubtraction)

    # Display the image with centers highlighted
    cv2.imshow('Image with Centers Highlighted', highlighted_image)

    # Save the image with centers highlighted
    output_path = os.path.join(file_path, 'LDHM_ParticleDetectionTagged.tiff')
    cv2.imwrite(output_path, highlighted_image)
    #print(f"Image with Centers Highlighted saved as {output_path}")

    titleBanner("Initial Readout", True)
    print("Number of Fragments:", fragments)
    print("Number of Particles:", particles)
    print("Number of Obstructions:", obstructions)

```

```
    hologram = imageRead(subject_image_path)
    hologram_array = np.array(hologram)

    # Image dimensions
    width_pixels,height_pixels = imageXY

    # Sensor size and pixel pitch in mm
    sensor_width_mm = width * 0.0022
    sensor_height_mm = height_pixels * 0.0022
    pixel_pitch_mm = sensor_width_mm / width_pixels

    # Wavelength in mm
    wavelength_mm = 640 / 1e6  # Convert nm to mm

    # Reconstruct the hologram for distances from 0 to 5mm in steps of 0.01mm
    minDist = 1.1
    maxDist = 1.5
    mmStep = 0.01
    distances_mm = np.arange(minDist, maxDist, mmStep)
    image_array = []
    for z in distances_mm:
        reconstructed = angularSpectrum(hologram_array, z, wavelength_mm, pixel_pitch_mm, pixel_pitch_mm)
        intensity_image = intensity(reconstructed, True)

```

```
        # Scale the intensity image to 8-bit for OpenCV display
        scaled_intensity = cv2.normalize(intensity_image, None, 0, 255, cv2.NORM_MINMAX, cv2.CV_8U)
        filename = 'Reconstruction_' + str(round(z, 2)) + '.tiff'
        cv2.imwrite(filename, scaled_intensity)
        #cv2.imshow("Intensity Reconstruction", scaled_intensity)
        image_array.append(scaled_intensity)
        cv2.waitKey(1)  # Adjust the delay in milliseconds for animation speed
        if cv2.waitKey(1) & 0xFF == 27:  # Press 'Esc' to exit the animation
            break

    # Loop through the centers and add center highlights to each image
    # Initialize dictionaries to store line profiles for each tag
    imageEdit = []
    line_length = 15  # Length of the horizontal line profile
    line_profiles_by_tag = {tag: [] for tag in particles_tags}
    #catCount10 = 0
    #catCount15 = 0
    #catCount25 = 0
    #catCount45 = 0
    catCountX = 0
    catCountWBC = 0
    catCountRBC = 0
```

```
    Z1 = 10
    Z2 = minDist
    magFact = (Z1 + Z2) / Z1
    titleBanner("Particle Sizing & Categorisation", True)
    for idx, image in enumerate(image_array):
        image_rgb = cv2.cvtColor(image, cv2.COLOR_GRAY2RGB)  # Convert image to RGB
        for center, tag in zip(particles_centers, particles_tags):
            center_x, center_y = center
            color = (0, 0, 255)  # Red color for particles
            add_center_highlight(image_rgb, center_x, center_y)
            cv2.putText(image_rgb, tag, (center_x - 10, center_y + 20), cv2.FONT_HERSHEY_SIMPLEX, 0.5, color, 1)

            # Extract horizontal line profile
            line_profile = extract_horizontal_line_profile(image, center_x, center_y, line_length)

            # Store line profiles in the corresponding dictionary based on their tags
            if line_profile is not None:
                line_profiles_by_tag[tag].append(line_profile)

            # Draw the line profile on the image
            if line_profile is not None:
                line_y = center_y
                line_x1 = center_x - line_length // 2
                line_x2 = center_x + line_length // 2
                cv2.line(image_rgb, (line_x1, line_y), (line_x2, line_y), (255, 255, 255), 1)
        cv2.imwrite(f"Edited_Image_{idx}.png", image_rgb)
        imageEdit.append(image_rgb)
```

```
498
499     # Display each edited image for 1 second (adjust the delay as needed)
500     for image in imageEdit:
501         cv2.imshow('Image', image)
502         cv2.waitKey(10)
503
504     # Save line profiles for each tag
505     for tag, line_profiles in line_profiles_by_tag.items():
506         tag_folder = f"Line_Profiles_{tag}/"
507         os.makedirs(tag_folder, exist_ok=True)
508         for idx, line_profile in enumerate(line_profiles):
509             profile_filename = os.path.join(tag_folder, f"{tag}_profile_{idx}.txt")
510             np.savetxt(profile_filename, line_profile)
511
512         # Loop through the particle tags and analyze them
513     for tag in particles_tags:
514         if tag.startswith("P"):
515             line_profiles_to_plot = line_profiles_by_tag[tag]
516
517             # Find the profile with the minimum intensity
518             min_intensity_profile_idx = np.argmin([np.min(profile) for profile in line_profiles_to_plot])
519             min_intensity_profile = line_profiles_to_plot[min_intensity_profile_idx]
520
521             # Calculate the threshold as intensity of the minimum point plus half of the range
522             threshold = np.min(min_intensity_profile) + (
523                         np.max(min_intensity_profile) - np.min(min_intensity_profile)) / 2
```

```
524
525             # Round the threshold crossings to the nearest integer
526             threshold_crossings = find_threshold_crossings(min_intensity_profile, threshold)
527             threshold_crossings = np.round(threshold_crossings).astype(int)
528
529             # Calculate the particle size
530             sensor_pixel_um = 2.2
531             particle_size = calculate_particle_size(threshold_crossings, sensor_pixel_um)
532             Z3 = Z2 + (mmStep * min_intensity_profile_idx)
533             magFact = Z1 / (Z1 + Z3)
534             sensor_pixel_um = 2.2
535             if len(threshold_crossings) >= 2:
536                 total_length_below_threshold = threshold_crossings[-1] - threshold_crossings[0]
537             else:
538                 total_length_below_threshold = 0
539
540             particle_size = (total_length_below_threshold * sensor_pixel_um) * magFact
541
542             # Categorize the particle based on its size
543             category = find_particle_category(particle_size)
544
```

```
            # Print the particle tag and size category
            print(f" ")
            print(f"Particle Tag: {tag}")
            print(f"Particle Size: {particle_size:.2f} microns")
            print(f"Particle Size Category: {category}")

            # Save the reconstruction image for this particle
            if category != "UnderBounds":
                reconstruction_image = image_array[min_intensity_profile_idx]
                reconstruction_filename = os.path.join(file_path, f'{tag}_Reconstruction.tiff')
                cv2.imwrite(reconstruction_filename, reconstruction_image)

                #print(f"Reconstruction image for {tag} saved as {reconstruction_filename}")

                # Save the line profile graph as P[number]_Profile in an appropriate image format
                profile_plot_filename = os.path.join(file_path, f'{tag}_Profile.png')
                plt.figure()
                plt.plot(min_intensity_profile, label=f"Profile {min_intensity_profile_idx} (Min Intensity)")
                plt.axhline(y=threshold, color='r', linestyle='--', label='Threshold')
                avg_profile = np.mean(np.array(line_profiles_to_plot), axis=0)
                plt.plot(avg_profile, label=f"Average Profile")
                plt.xlabel("Position")
                plt.ylabel("Intensity")
                plt.title(f"Line Profiles for Tag {tag} - Min Intensity with Threshold Line")
                plt.legend()
                plt.savefig(profile_plot_filename)
                plt.close()

```

```
    titleBanner("Final Readout", True)
    print("Total Number Of Particles:", particles)
    print("Number of RBC:", catCountRBC)
    print("Number of WBC:", catCountWBC)
    print(" ")
    cv2.waitKey(0)
    cv2.destroyAllWindows()
```

Figure 82: Appendix; Complete Computer Vision Software

10.2: Technical Drawing LDHM Device

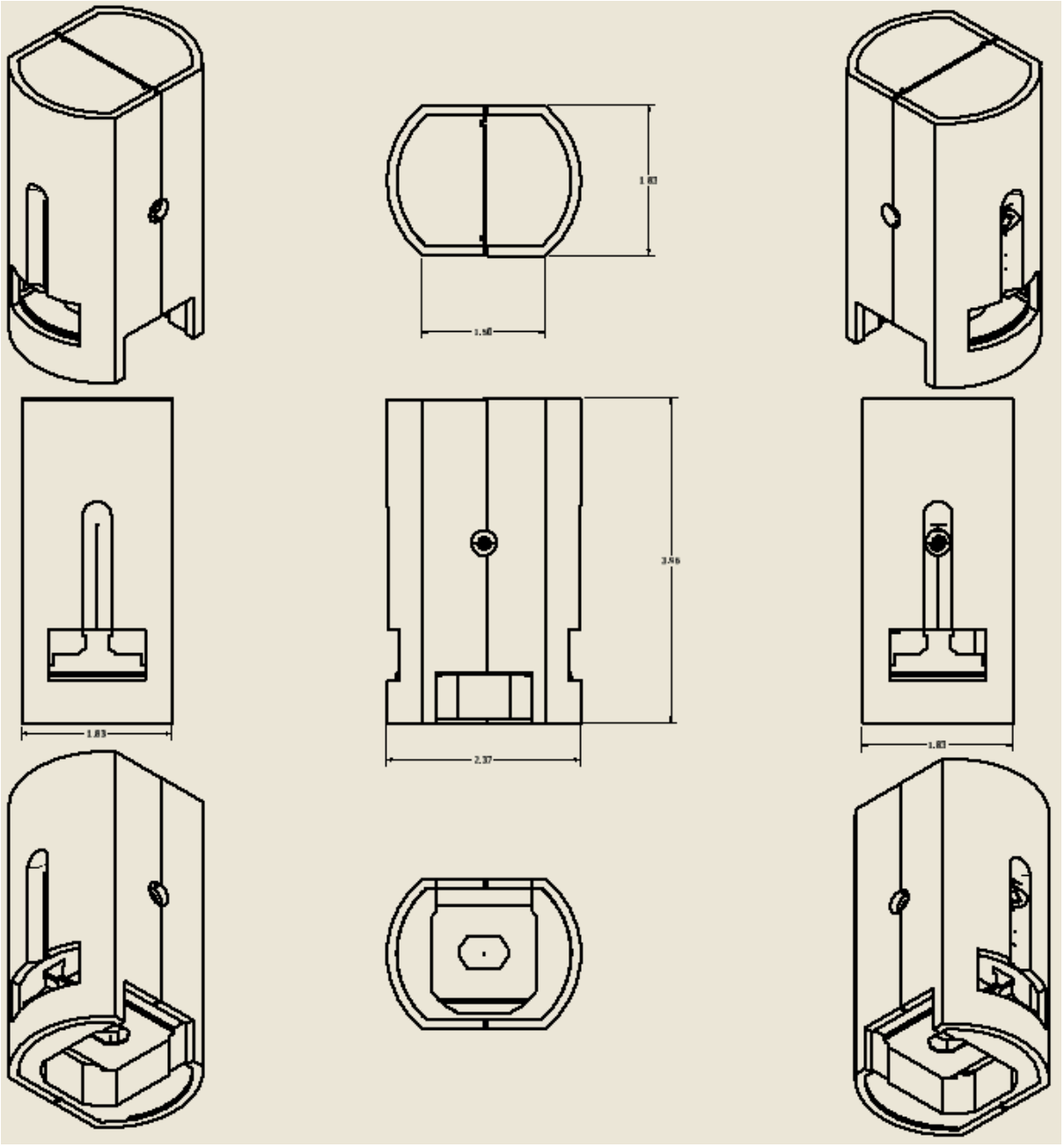

Figure 83: Appendix; Technical Drawing (Prototype LDHM device)